DISSERTATION

A THEORETICAL AND NUMERICAL INVESTIGATION OF WARM-PHASE MICROPHYSICAL PROCESSES

Submitted by

Adele Igel

Department of Atmospheric Science

In partial fulfillment of the requirements

For the Degree of Doctor of Philosophy

Colorado State University

Fort Collins, Colorado

Fall 2015

Doctoral Committee:

Advisor: Susan van den Heever

Sonia Kreidenweis
Steven Rutledge
Iuliana Oprea

ABSTRACT

A THEORETICAL AND NUMERICAL INVESTIGATION OF WARM-PHASE MICROPHYSICAL PROCESSES

Several studies examining microphysical processes are conducted with an emphasis on further understanding warm-phase processes, particularly condensation. In general, these studies progress from simple to complex representations of microphysical processes in models. In the first study, a theoretical, analytical expression for the condensational invigoration, that is the invigoration in the warm-phase of a cloud due to changes in the condensation rate, of a polluted, cloudy parcel of air relative to a clean, cloudy parcel of air is developed. The expression is shown to perform well compared to parcel model simulations, and to accurately predict the invigoration to within 30% or less. The expression is then used to explore the sensitivity of invigoration to a range of initial conditions. It is found that the invigoration, in terms of added kinetic energy, is more sensitive to the cloud base temperature than to the initial buoyancy of the parcels. Changes in vertical velocity between clean and polluted parcels of up to 4.5 m s^{-1} at 1 km above cloud base are theoretically possible, and the difference in vertical velocity decreases when the initial vertical velocity of either parcel is large. These theoretical predictions are expected to represent an upper limit to the magnitude of condensational invigoration and should be applicable to both shallow cumulus clouds as well as the warm phase of deep convection.

In the second study, the focus shifts to the comparison of the representation of microphysical processes in single- and double-moment microphysics schemes. Single-moment microphysics schemes have long enjoyed popularity for their simplicity and efficiency.

However, it is argued that the assumptions inherent in these parameterizations can induce large errors in the proper representation of clouds and their feedbacks to the atmosphere. For example, precipitation is shown to increase by 200% through changes to fixed parameters in a single-moment scheme and low cloud fraction in the RCE simulations drops from ~15% in double-moment simulations to ~2% in single-moment simulations. This study adds to the large body of work that has shown that double-moment schemes generally outperform single-moment schemes. It is recommended that future studies, especially those employing cloud-resolving models, strongly consider moving to the exclusive use of multi-moment microphysics schemes.

An alternative to multi-moment schemes is a bin scheme. In the third study, the condensation rates predicted by bin and bulk microphysics schemes in the same model framework are compared in a novel way using simulations of non-precipitating shallow cumulus clouds. The bulk scheme generally predicts lower condensation rates than does the bin scheme when the saturation ratio and the integrated diameter of the droplet distribution are identical. Despite other fundamental disparities between the bin and bulk condensation parameterizations, the differences in condensation rates are predominantly explained by accounting for the width of the cloud droplet size distributions simulated by the bin scheme which can alter the rates by 50% or more in some cases.

The simulations are used again in the fourth study in order to further investigate the dependency of condensation and evaporation rates to the shape parameter and how this dependency impacts the microphysical and optical properties of clouds. The double-moment bulk microphysics simulations reveal that the shape parameter can lead to large changes in the average condensation rates, particularly in evaporating regions of the cloud where feedbacks between evaporation and the depletion of individual droplets magnify the dependency of the

evaporation rate on the shape parameter. As a result the average droplet number concentration increases as the shape parameter increases, but changes to the cloud water content are small. Taken together, these impacts lead to a decrease in the average cloud albedo. Finally, the simulations indicate that the value of the shape parameter in subsaturated cloudy air is more important than the value in supersaturated cloudy air, and that a constant shape parameter may not be a poor assumption for simulations of non-precipitating shallow cumulus clouds.

ACKNOWLEDGEMENTS

First and foremost I would like to acknowledge by advisor, Susan van den Heever, for her guidance, insightful discussions, and willingness to send me to conferences during my time as a PhD candidate. I would also like to thank my committee members for taking the time to serve and meet with me several times over the course of the last three years. In Chapter 2, Leah Grant is responsible for introducing the prediction of vertical velocity in the parcel model and I have had many useful conversations with Daniel Rosenfeld about condensational invigoration. In Chapter 3, Emily Parker assisted in analyzing the simple thunderstorm simulations, and Matthew Igel provided the radiative-convective equilibrium simulations. Chapters 4 and 5 would not have been possible without the bin microphysics code that was provided by Alexander Khain. I would like to thank all of the past and current members of the van den Heever Cloud Processes Group for their helpful comments and discussions. I am especially grateful to Stephen Saleeby and Stephen Herbener for their continued work to improve RAMS and to Leah Grant for letting me continually interrupt her work in order to talk about mine. Finally, Matthew Igel was both a group member and is still my husband and has discussed my work, offered advice, and supported me more than anyone else. This material is based upon work supported by the National Science Foundation Graduate Research Fellowship Program under Grant DGE-1321845 as well as National Aeronautics and Space Administration Grants NNX 13AN66H and NNX 13AQ33G.

TABLE OF CONTENTS

1. INTRODUCTION

Cloud microphysics is a key component of the atmospheric system and it impacts our weather and climate in a number of significant ways. Most obviously, it is critical for determining how much precipitation reaches the Earth's surface. Precipitation includes everything from weak drizzle to blizzards and damaging hail, all of which have large impacts on society. But, as important as precipitation is, it is not the only reason to care about cloud microphysics. It plays an important role in determining the magnitude and location of latent heating in clouds, which in turn is an important process that contributes to the buoyancy and dynamics of clouds and the generation of gravity waves. Thus, cloud microphysics is also critical for understanding storm dynamics. The microphysical structure of clouds is also important for evaluating how sunlight and other radiation are scattered, reflected, and absorbed and how this radiation warms and cools the atmosphere. Through its role in determining both latent and radiative heating and cooling, cloud microphysics speaks directly to Earth's energy balance. Finally, a knowledge of cloud microphysics is necessary to understand how increasing pollution will impact clouds by altering all of these processes that are impacted by cloud microphysics. However, in spite of the many components of the atmospheric system that cloud microphysics influences, the study of cloud microphysics for its own sake is of scientific interest, and is an area that needs to be well understood before it can be accurately used in the study of other atmospheric phenomena, such as those discussed above.

For liquid water hydrometeors, the basic microphysical processes are nucleation (the formation of new droplets), condensation and evaporation (the growth and decay of droplets), collision-coalescence (the behavior of droplets during collisions), break-up (the behavior of

droplets when they become large), and sedimentation (the physics governing how droplets fall). These processes are all reasonably well understood individually when considering just one or two droplets at a time with perhaps sedimentation being best understood and break-up being least well understood. The main difficulty in the study of cloud microphysics is in describing how these processes all interact and proceed simultaneously, and in doing so on spatial scales that are much larger than the hydrometeors themselves. For example, a small radar sampling volume or a small atmospheric model grid box might be on the order of 10^6 m^3 or 0.001 km^3 in size. A small cloud droplet may have a diameter of 10 μm, and a large raindrop may have a diameter of 1 mm. Assuming both have mass concentrations of 1 gram per cubic meter of air, then there are 2 quadrillion cloud droplets or 2 billion rain drops in the radar sampling volume or model grid box. So, while theoretical work and laboratory experiments have been largely successful in developing mathematical equations to describe processes such as condensation and collision-coalescence for individual drops (Pruppacher and Klett 2010), using these equations to explain the behavior of the immense number of hydrometeors in real clouds is challenging.

For condensation, the simplest way to avoid worrying about individual droplets in a model is to assume that the atmosphere is never supersaturated, and that those thermodynamic conditions that give rise to supersaturation immediately result in the condensation of water until saturation is achieved. This process is called saturation adjustment (MacDonald 1963) and has been used in numerous microphysics schemes (e.g. Soong and Ogura 1973; Rutledge and Hobbs 1983; Bryan and Fritsch 2002; Morrison et al. 2009). In using this saturation adjustment approach, nothing needs to be known about the characteristics of the cloud droplets or rain drops since the amount of water condensed is entirely controlled by the atmospheric conditions. However, observations of clouds and aerosol spectra suggest that the atmosphere is able to

achieve supersaturated conditions (e.g. Twomey 1959; Hudson 1980; Hoppel 1996). Most estimates of supersaturation have been made for stratus clouds and fog; estimating the supersaturation in convective updrafts is more difficult, but theoretical estimates suggest it could be 10% or higher (Fukuta 1993). Modeling studies indicate that magnitude of the supersaturation is a competition between the rate of generation due to adiabatic cooling and the rate of condensation which depends on the number and size of the cloud droplets, and it in turn impacts the updraft strength of the cloud (Kogan and Martin 1994; Khain et al. 2004, 2005, 2008; Lee et al. 2008; Storer and van den Heever 2013; Seiki and Nakajima 2014; Koren et al. 2014). While numerous studies have shown that these relationships exist, a simple theoretical framework does not exist with which to understand how the magnitude of the supersaturation and the updraft strength are related. This problem will be addressed in Chapter 2 where it is hypothesized that a simple description of condensation can be used to derive reasonable upper estimates of the change in kinetic energy and updraft velocity between clouds with different maximum supersaturation values.

For all other microphysical processes, and for non-saturation adjustment condensation schemes, some properties about the hydrometeors must be known in order to predict the rates of these processes. For many applications, a first step is to assume that statistical probability distribution functions (PDFs) can be used to characterize the distribution of individual hydrometeor sizes or masses in order to describe the large quantities of hydrometeors in the atmosphere. In both observational analysis and modeling, a gamma (Γ) PDF or an exponential PDF (a special case of the gamma PDF) is typically assumed since this function has been found to fit well to many observed distributions of hydrometeors (e.g. Marshall and Palmer 1948; Gunn

and Marshall 1958; Ulbrich 1983; Liu et al. 1995; Haddad et al. 1996). There are many ways to express the gamma PDF; in this dissertation, the size distribution ($n(D)$) will be expressed as

$$n(D) = \frac{N}{D_n \Gamma(\nu)} \left(\frac{D}{D_n}\right)^{\nu-1} e^{-D/D_n}$$

following Walko et al. (1995). In this equation, D is the hydrometeor diameter, N is the total number concentration, ν is referred to as the shape parameter, and D_n is referred to as the characteristic diameter. In the radar community, it is more common to see the gamma PDF written as

$$n(D) = N_0 D^{\mu} e^{-\Lambda D} \qquad \text{or} \qquad n(D) = N \frac{(3.67+\mu)^{\mu+1}}{D_0 \Gamma(\mu+1)} \left(\frac{D}{D_0}\right)^{\mu} e^{-(3.67+\mu)D/D_0}$$

as in Gorgucci et al. (2002) where $\mu=\nu-1$ is also called a shape parameter, $\Lambda=D_n^{-1}$ is called the slope parameter, $N_0=ND_n^{-1}\Gamma(\nu)$ is the intercept parameter, and D_0 is the median diameter. An exponential PDF is obtained in all formulations when $\nu=1$ or $\mu=0$. Regardless of the formulation, there are three independent parameters in the distribution; in the first formulation, these parameters are N, ν and D_n. There is a strong interest in determining the appropriate values of these parameters for various hydrometeor types for a number of reasons. For example, knowing the values of these parameters can help to constrain relationships between radar reflectivity and rain rate or snowfall rate (e.g. Ulbrich and Atlas 1998; Liao et al. 2014; Thompson et al. 2015). For satellite retrievals, these values are needed in order to retrieve measurements of the effective radius and optical depth (Platnick and Valero 1995; Painemal and Zuidema 2011; King et al. 2013). In cloud microphysical model parameterizations, assuming a PDF to describe the hydrometeor size distribution will reduce the number of variables that need to be predicted (e.g. Khain et al. 2015). Such parameterizations are referred to as "bulk" microphysics parameterizations or schemes. In most bulk microphysics parameterizations, at least one of these parameters, if not two, must be held fixed or otherwise diagnosed (often somewhat arbitrarily),

but the values that are chosen may strongly influence the simulations (Ferrier et al. 1995; Morrison and Grabowski 1998; Gilmore et al. 2004; van den Heever and Cotton 2004; Yussouf and Stensrud 2012; Adams-Selin et al. 2013).

The first of the three independent parameters, N, is the total number concentration, and is the value that is obtained when the PDF is integrated over all sizes. In some bulk microphysics schemes, N, or more often the closely related quantity the mass mixing ratio, r, is the only quantity predicted for each of the hydrometeor categories (e.g. Lin et al. 1983; Walko et al. 1995; Straka and Mansell 2005; Hong and Lim 2006). These are known as single-moment bulk microphysics schemes because only one moment of the distribution is predicted. In these schemes, usually the shape parameter and intercept parameter are held fixed, and the characteristic diameter is diagnosed. Though these schemes tend to be simple, increasingly they are being replaced by double-moment bulk microphysics schemes in which two moments of the distribution, typically the number concentration and mass mixing ratio, are predicted (e.g. Ferrier 1994; Meyers et al. 1997; Milbrandt and Yau 2005a; Morrison et al. 2005; Seifert and Beheng 2006; Mansell et al. 2010). A more in-depth discussion of single- and double-moment schemes is presented in Chapter 3 where it is argued that there are compelling reasons to favor double-moment schemes for most atmospheric modeling applications based on past literature results, simple theoretical arguments, single-moment scheme sensitivity tests, and multi-cloud simulations.

Even in double-moment schemes, the shape parameter must be held fixed or diagnosed based on other cloud properties. It is a poorly constrained parameter based on observations (Miles et al. 2000; Bringi and Chandrasekar 2001; McFarquhar et al. 2014). Specification of this parameter in models can be circumvented by moving to triple-moment schemes or to bin

microphysics schemes in which PDFs are not assumed but, instead, the diameter range over which the hydrometeor species exists is broken into bins, and the number concentration (or mass mixing ratio) of each bin is explicitly predicted (e.g. Khain et al. 2015). In this way the size distribution shape can evolve freely and there is no need to specify distribution parameters as was necessary in the single- and double-moment bulk microphysics schemes. However, whereas in bulk schemes there are at most three quantities predicted for each hydrometeor type, in spectral bin schemes thirty or more bins may be used to represent each species and hence thirty or more quantities need to be predicted. Thus, while spectral bin schemes are typically thought to more accurately describe microphysical processes (e.g. Beheng 1994; Seifert and Beheng 2001; Morrison and Grabowski 2007; Milbrandt and Yau 2005; Milbrandt and McTaggart-Cowan 2010; Kumjian et al. 2012), they are much more computationally expensive to run. Partly for this reason bulk schemes are used currently in all operational weather and climate forecast models. In fact, bin schemes have only recently been used in 3D, rather than 2D, simulations of the atmosphere for research purposes (e.g. Ovthchinnikov and Kogan 2000). So, while bin schemes are becoming more popular for basic research applications (a situation that is enhanced by increasing computational resources), there is still a need to develop and improve bulk microphysics parameterizations.

To that end, condensation and evaporation rates in simulations using bin and bulk microphysics schemes are compared in Chapter 4 in order to identify ways in which the condensation rates in bulk microphysics schemes might be improved. It is found that the fixed shape parameter in bulk microphysics schemes is the primary reason why condensation and evaporation rates do not agree with those in bin schemes. Motivated by this finding, additional simulations are run using a double-moment bulk scheme to determine how the shape parameter

can impact the microphysical and optical properties of clouds. These results are discussed in Chapter 5. In this chapter, it is hypothesized that in the absence of drizzle formation the shape parameter influences properties of clouds primarily through changes to the evaporation process, and that representing the spatial variability of the shape parameter may not have a large impact on these cloud properties.

In summary, the dissertation is organized such that the degree of microphysical complexity being discussed increases with each chapter. First, in Chapter 2, there is a primarily theoretical discussion of condensation and how it relates to convective invigoration in warm clouds. In Chapter 3, I investigate the sensitivity of a single-moment scheme to the choice and value of fixed parameters and compare its performance to a double-moment scheme. The focus shifts to a comparison of double-moment bulk and spectral bin microphysics schemes in Chapter 4. Lastly, in Chapter 5, the sensitivity of the double-moment bulk scheme to a fixed shape parameter is tested with guidance from observations and the bin microphysics scheme. Final conclusions are presented in Chapter 6.

2. A THEORETICAL FRAMEWORK FOR PREDICTING THE MAGNITUDE OF CONDENSATIONAL INVIGORATION

2.1 Introduction

The interaction of aerosols and clouds is of interest because of changes in the cloud radiative properties and precipitation production that aerosols can cause. Changes to the cloud microphysical properties due to increases in aerosol concentration lead to increases in the cloud albedo, as first proposed by Twomey (1974, 1977), and to decreases in precipitation from shallow warm clouds, as first suggested by Squires (1958). In addition, aerosols can alter the cloud dynamics, which can lead to further changes to the radiative properties of clouds and their precipitation production. The impacts on radiative properties and precipitation production caused by aerosol-induced changes in dynamics can often be larger than the impacts caused by the direct changes to the cloud microphysics alone (Tao et al. 2012). The question of how aerosols impact the dynamics of both shallow and deep convective clouds is one that has received much attention in the literature.

Most commonly, aerosol-cloud dynamical feedbacks are discussed in terms of invigoration. "Invigoration" is typically defined as an increase in the cloud vertical velocity (e.g. Andreae et al. 2004; Rosenfeld et al. 2008; Li et al. 2011; Fan et al. 2013; Storer and van den Heever 2013). In convective clouds, invigoration is thought to occur in two stages: one stage in the warm phase of the cloud, and a second when ice is formed. Invigoration in the ice phase, though the most commonly mentioned method of invigoration in the literature, will not be discussed here. Andreae et al. (2004), Khain et al. (2005), van den Heever et al. (2006),

Rosenfeld et al. (2008), Fan et al. (2013), Storer and van den Heever (2013), and Altaratz et al. (2014), among others, discuss this process in detail.

In the warm phase, increased condensational growth of cloud droplets occurs under more polluted conditions. This idea was demonstrated by Kogan and Martin (1994) using simulations and was shown analytically to be true by Pinsky et al. (2013). With more condensational growth of cloud droplets, more latent heat is released, buoyancy increases, and the cloud becomes invigorated. A number of studies have shown directly that the changes in condensational growth due to a larger number of droplets leads to increases in vertical velocity in warm shallow clouds, and that this effect saturates at a few hundred CCN cm^{-3} (Kogan and Martin 1994; Seiki and Nakajima 2014; Koren et al. 2014; Saleeby et al., 2015; Sheffield and van den Heever 2015). This process has been termed "condensational invigoration" (Seiki and Nakajima 2014). Condensational invigoration is also addressed by others who, through simulations of deep convective clouds, show that condensation in the warm phase and updraft strength both increase in more polluted clouds (Khain et al. 2004, 2005, 2008; Lee et al. 2008; Lebo and Seinfeld 2011; Storer and van den Heever 2013). However, two outstanding questions remain. First, what should the magnitude of condensational invigoration be from a theoretical standpoint? And second, how does this magnitude vary for a wide range of initial conditions?

In section 2.2, we introduce a theoretical framework with which to understand the maximum possible condensational invigoration. Rather than using vertical velocity to quantify condensational invigoration, we will use kinetic energy, which, as will be seen below, is more convenient for quantifying condensational invigoration in this theoretical framework. We describe parcel model experiments in section 2.3, and analyze these experiments in order to assess the validity of the theoretical expression in section 2.4. Finally, we use the derived

theoretical expression to explore the magnitude of condensational invigoration for various initial conditions in section 2.5. The results are summarized in section 2.6.

2.2 Theoretical Framework

The objective of this study is to develop an expression for the upper limit of the difference in kinetic energy of two parcels, one clean and one polluted, as a function of height when all else is equal. The kinetic energy of a parcel, which is a quantity closely related to the convective available potential energy (CAPE), is equivalent to the path integral of the buoyancy of a parcel. Therefore, we begin by writing an expression for the Reynolds-averaged buoyancy (B) of a parcel of air with temperature (T), water vapor mixing ratio (r_v), and liquid water mixing ratio (r_l), at a height (z) above cloud base as:

$$B(z) = g\left(\frac{T_v(z)-\overline{T_v}(z)}{\overline{T_v}(z)} - r_l(z)\right) \tag{2.1}$$

$$\text{where} \quad T_v = T\left(1 + \frac{1-\varepsilon}{\varepsilon} r_v\right) \tag{2.2}$$

is a commonly-used approximation to the virtual temperature, the overbar indicates the environmental value, and ε is the ratio of the molecular weights of water to dry air (0.622). Pressure gradient forces and entrainment are neglected. Note that these factors would generally reduce the net acceleration of the parcels and hence they do not hinder us from analytically expressing an upper limit of invigoration. For now, we assume that $\overline{T_v}$ is independent of height. We will show later that this assumption does not strongly impact the results.

The virtual temperature of the parcel changes as the height above cloud base increases due to adiabatic cooling, latent heating, and vapor depletion. This is expressed as:

$$T_v(z) = \left(T_0 - \Gamma_d z + \frac{L}{c_p} r_l(z)\right)\left[1 + \frac{1-\varepsilon}{\varepsilon}\left(r_{v_0} - r_l(z)\right)\right] \tag{2.3}$$

where the subscript *0* indicates the value at cloud base, Γ_d is the dry adiabatic lapse rate, L is the latent heat of vaporization and c_p is the specific heat capacity of air at constant pressure.

After substituting Eq. 2.3 into Eq. 2.1, the difference in buoyancy between a clean (c) and polluted (p) parcel that are otherwise identical can be expressed as:

$$B_p(z) - B_c(z) =$$

$$g\left(\frac{L}{c_p\overline{T_v}}\left(1+\frac{1-\varepsilon}{\varepsilon}r_{v_0}\right)+\frac{1-\varepsilon}{\varepsilon\overline{T_v}}(\Gamma_d z - T_0) - 1\right)\left(r_{lp}(z) - r_{lc}(z)\right) - \frac{gL(1-\varepsilon)}{\varepsilon c_p\overline{T}_v}\left(r_{lp}(z)^2 - r_{lc}(z)^2\right) \tag{2.4}$$

Magnitudinal estimates of each term indicate that the terms with r_{v0}, Γ_d, or r_l^2 are at least two orders of magnitude lower than the highest order term and can be neglected when $\overline{T_v}$ and T_0 are estimated to be 300K, r_{v_0} to be 15 g kg^{-1}, and z to be less than 5 km. Thus Eq. 2.4 reduces to:

$$B_p(z) - B_c(z) = a\left(r_{lp}(z) - r_{lc}(z)\right) \tag{2.5}$$

$$\text{where} \quad a = g\left(\frac{L}{c_p\overline{T_v}} - \frac{1-\varepsilon}{\varepsilon}\frac{T_0}{\overline{T_v}} - 1\right) \tag{2.6}$$

At this point progress cannot be made unless the dependence of the liquid water mixing ratio (r_l) on the height above cloud base (z) is known. For this we turn to the work of Pinsky et al. (2013), hereafter referred to as P13. P13 developed an approximate, universal, analytical equation for the derivative of liquid water with respect to height (their Eq. 39):

$$\frac{dQ^*}{dh^*} = (h^* - Q^*)Q^{*1/3} \tag{2.7}$$

where Q^* and h^* are the universal cloud water mixing ratio and height, respectively. The universal solution can be transformed into actual solutions through the use of scaling factors that are described in P13. P13 assume that the variables A1 and A2 (see Eq. 2.9 below) and the vertical velocity of the parcel are constant with height and that the liquid water content at cloud base is zero in order to arrive at Eq. 2.7. This latter assumption was relaxed in Pinsky et al.

(2014), but was not found to strongly impact our results. The assumption of constant vertical velocity results in the underestimation of the maximum supersaturation and overestimation of condensed liquid water, particularly at levels below the level of maximum supersaturation (not shown). Though unavoidable here, this assumption will not be made elsewhere in this theoretical framework.

The numerical solution to Eq. 2.7 is shown in Figure 2.1. Unfortunately, a simple analytic expression for this solution does not exist. However, we can approximate the solution in Figure 2.1 with a piece-wise function. We fit the lower portion of the solution with a polynomial, and the upper portion of the solution with a line; these best-fit curves are also shown in Figure 2.1, and are seen to approximate the numerical solution very well. We transition the fit from the polynomial to the line at the level of maximum supersaturation, which is uniquely defined in the universal framework developed by P13. In other words, there exists a unique relationship between the maximum supersaturation ($S_{\max}$), the height of the maximum supersaturation ($z_{\max}$), and the cloud water mixing ratio at this height ($r_{l\max}$; see Eq. 35 in P13). The best-fit piecewise function shown in Figure 2.1 is expressed as:

$$Q^*(h^*) = \begin{cases} C_3(h^*/C_2)^{B_1} & , h^* < C_2 \\ B_2(h^* - C_2) + C_3, & h^* \geq C_2 \end{cases} \tag{2.8}$$

where C_2=1.904, C_3=0.846, B_1=2.4, and B_2=1.09. C_1 (not used here) and C_2 are constants determined by P13, and C_3=C_2–C_1. Physically, C_2 is the universal height of maximum supersaturation, and C_3 is the universal cloud water content at C_2. B_1 and B_2 are the best-fit parameters we found in Figure 2.1.

The universal quantities are transformed back to physical quantities using the relationships in P13 (their Eq. 37) such that we now have:

$$r_l(z) = \begin{cases} r_{l\max}(z/z_{\max})^{B_1} & , z < z_{\max} \\ B_2 A_1 A_2^{-1}(z - z_{\max}) + r_{l\max} & , z \geq z_{\max} \end{cases} \quad (2.9)$$

where A_1 and A_2 are defined by P13 as $A_1 = \frac{g}{R_a T}\left(\frac{LR_a}{c_p R_v T} - 1\right)$ and $A_2 = r_{v_0}^{-1} + \frac{L^2}{c_p R_v T^2}$, R_a and R_v are the dry air and water vapor gas constants, respectively, and $r_{l\max}$ and $z_{\max}$ (and also $S_{\max}$) are functions only of the cloud base vertical velocity and cloud droplet number concentration for a given initial cloud base temperature and pressure (Figs. 2.2 and 2.3; see also P13 Eqs. 32-34[1] which are reproduced here in section 2.7). It is seen that $z_{\max}$, $S_{\max}$, and $r_{l\max}$ increase rapidly as the cloud base vertical velocity increases, and that these quantities decrease as the cloud droplet concentration increases (Fig. 2.2). Additionally, $S_{\max}$ is least sensitive to the cloud base temperature, whereas $r_{l\max}$ is most sensitive (Fig. 2.3). $z_{\max}$, $S_{\max}$, and $r_{l\max}$ are all more sensitive to the droplet concentration than to the cloud base temperature, particularly at low droplet concentrations (Fig. 2.3). Because the equations developed by P13 do not account for buoyancy and feedbacks to vertical velocity as the parcel rises, the values of $z_{\max}$, $S_{\max}$, and $r_{l\max}$ are all underestimates of their true values for the case where vertical velocity increases above cloud base.

Substituting Eq. 2.9 into Eq. 2.5 yields a simple, piece-wise equation for the difference in buoyancy between a clean and polluted parcel:

$$B_p(z) - B_c(z) = \begin{cases} a\left(r_{lp\max}\left(z/z_{p\max}\right)^{B_1} - r_{lc\max}(z/z_{c\max})^{B_1}\right), z < z_{p\max} \\ a\left(B_3\left(z - z_{p\max}\right) + r_{lp\max} - r_{lc\max}(z/z_{c\max})^{B_1}\right), z_{c\max} > z \geq z_{p\max} \\ a\left(B_3\left(z_{c\max} - z_{p\max}\right) + r_{lp\max} - r_{lc\max}\right), z \geq z_{c\max} \end{cases} \quad (2.10)$$

[1] Note that the coefficient in P13 Eq. 34 should be $C_2 - C_1$, not $C_2/C_1 - 1$.

where $B_3 = B_2 A_1 A_2{}^{-1}$. Note that $S_{\max}$ for a polluted parcel will be less than that of a clean parcel (P13), and thus $z_{p\max} < z_{c\max}$ and $r_{lp\max} < r_{lc\max}$ since $S_{\max}$, $z_{\max}$, and $r_{l\max}$ are all linearly related.

Finally, we integrate both sides of Eq. 2.10 with respect to z. Such integration of each buoyancy term on the left-hand side yields kinetic energy (K). The kinetic energy in this case is the same as CAPE, but we refer to it as kinetic energy in order reinforce the fact that this quantity is directly related to vertical velocity, and that *the difference in kinetic energy or vertical velocity is a measure of invigoration*. The integrated form of Eq. 2.10 is:

$$K_p(z) - K_c(z) = \Delta K(z) =$$

$$\begin{cases} \frac{a}{B_1+1}\left(r_{lp\max}\frac{z^{B_1+1}}{z_{p\max}{}^{B_1}} - r_{lc\max}\frac{z^{B_1+1}}{z_{c\max}{}^{B_1}}\right) & , z < z_{p\max} \\ a\left(\frac{B_3}{2}\left(z - z_{p\max}\right)^2 + r_{lp\max}\left(z - z_{p\max}\right) - \frac{r_{lc\max}}{B_1+1}\frac{z^{B_1+1} - z_{p\max}{}^{B_1+1}}{z_{c\max}{}^{B_1}}\right) + \Delta K\left(z_{p\max}\right) & , z_{c\max} > z \geq z_{p\max} \\ a\left(B_3\left(z_{c\max} - z_{p\max}\right) + r_{lp\max} - r_{lc\max}\right)(z - z_{c\max}) + \Delta K(z_{c\max}) & , z \geq z_{c\max} \end{cases}$$

(2.11)

Note that had we developed an equation for the vertical velocity difference, the full expression for buoyancy would need to be integrated for the clean and polluted parcels separately (Eq. 2.1 with Eq. 2.3) so that the square root of each could be taken, and there would be no cancellation of terms as we have done in developing the kinetic energy difference expression (Eq. 2.11). This is the primary reason why the kinetic energy difference expression is simpler than the equivalent expression for the vertical velocity difference.

All three parts of this piece-wise equation show that the change in kinetic energy between a polluted parcel and a clean parcel is proportional to the height of maximum supersaturation and to the cloud water mixing ratio at that height of both the clean and polluted parcels. However, since $S_{\max}$, $r_{l\max}$, and $z_{\max}$ are all linearly proportional to one another, these equations could be rewritten in terms of any one of these quantities.

These equations can be simplified if we consider the case of a polluted parcel with an infinite aerosol concentration. In this case, the condensation rate becomes infinitely fast (since condensation rate is directly proportional to the droplet concentration which is infinite) and therefore the polluted parcel will condense any supersaturation immediately. $S_{p\max}$, $r_{lp\max}$, and $z_{p\max}$ are thus all equal to zero. This case is equivalent to saturation adjustment, and can be considered infinitely polluted. In such a case, the first part of the piece-wise equation (Eq. 2.11) vanishes, and the second two parts reduce to:

$$\Delta K(z) = \begin{cases} a\left(\frac{B_3 z^2}{2} - \frac{r_{lc\max}}{B_1+1}\frac{z^{B_1+1}}{{z_{c\max}}^{B_1}}\right) & , z < z_{c\max} \\ a(B_3 z_{c\max} - r_{lc\max})(z - z_{c\max}) + \Delta K(z_{c\max}) & , z \geq z_{c\max} \end{cases} \quad (2.12)$$

Thus far we have assumed that the environmental virtual temperature profile is isothermal. We now assess the magnitude of the error associated with this assumption. Since the third line of Eq. 2.10 contributes most to the total invigoration, especially when $z_{c\max}$ is small, we will reintegrate that equation, but now we assume that $\overline{T_v} = \overline{T_{v0}} - \Gamma_e z$ in coefficient a such that now the environmental virtual temperature is a linear function of height. Note that all other terms in line 3 of Eq. 2.10 are independent of z. Reintegration of this equation from $z_{c\max}$ to some arbitrary height z above cloud base yields:

$$\Delta K(z) = a'^{\left(B_3(z_{c\max} - z_{p\max}) + r_{lp\max} - r_{lc\max}\right)}(z - z_{c\max}) + \Delta K(z_{c\max}) \quad (2.13)$$

$$a' = g\left(\frac{\left(\frac{L}{c_p} - \frac{1-\varepsilon}{\varepsilon}T_0\right)\ln\left(\frac{\overline{T_{v0}} + \Gamma_e z}{\overline{T_{v0}} + \Gamma_e z_{c\max}}\right)}{\Gamma_e(z - \square_{c\max})} - 1\right) \quad (2.14)$$

The result is the same as in line 3 of Eq. 2.11, but the coefficient a in Eq. 2.11 has been redefined to be *a'* in Eq. 2.13. Using these two coefficients, the error imposed by assuming an isothermal atmosphere in Eq. 2.11 can be calculated for different values of Γ_e. This error is shown in Figure 2.4 as a function of height above cloud base and for two values of $z_{c\max}$, 10m and 100m. At 1 km

above cloud base, the error is about 2% for an environmental lapse rate of 10 K km^{-1} and about 4% for the extreme lapse rate of 20 K km^{-1}. This is a small error, even in the extreme case, and hence it is justifiable to neglect the environmental profile of virtual temperature. It should be emphasized again that the invigoration is expressed as the *difference* in kinetic energy between a clean and polluted parcel; although $K(z)$ for each parcel individually would be expected to be highly sensitive to Γ_e, $\Delta K(z)$ is not.

2.3 Parcel Model Experiments

A Lagrangian parcel model (Heymsfield and Sabin 1989; Feingold and Heymsfield 1992; Saleeby and Cotton 2004) was used in order to assess the validity of our theoretical expression for the change in kinetic energy between a clean and polluted parcel. The parcel model predicts the evolution of a lognormally distributed population of dry aerosol particles as they grow by condensation to cloud droplet sizes, as well as the vertical velocity of the parcel. Further details about the parcel model can be found in section 2.8.

Simulations were run with the parcel model using two different environmental conditions. Since the theoretical expression assumed an isothermal atmosphere, the parcel model environmental conditions used a temperature of 288K or 298K that was constant with height and a constant water vapor mixing ratio such that the relative humidity at 500m was 70%. The parcel was initialized at 500m with a temperature perturbation of 0.5K, a relative humidity of 99%, and a vertical velocity of 0.5 m s^{-1}. These initial conditions were chosen so most parcels grow to at least 1km above cloud base. A time step of 0.1 s is used. Simulations were ended when the parcel stopped rising. Although the use of an isothermal atmosphere is unrealistic, both Figure 2.4 and additional parcel model simulations (not shown) indicate that the invigoration is

minimally sensitive to the environmental conditions. Thus, despite the use of an isothermal atmosphere, these tests can be representative of either shallow convection or the warm-phase of deep convection.

Eight simulations were run with the parcel model using each of the two environmental conditions. The aerosol concentration was doubled with each test, starting at 25 cm^{-3} and ending at 1600 cm^{-3}. A lognormal distribution for the aerosol particles with a median radius of 40 nm and a geometric standard deviation of 1.8 was assumed for all simulations. The eighth simulation was run using saturation adjustment instead of explicit condensation for each environmental condition, and these simulations will subsequently be referred to as the "infinitely polluted" simulations since the condensation rate becomes infinitely fast in this situation, as explained in section 2.2.

2.4 Comparison to the Parcel Model

We will focus our analysis of Eq. 2.11 on the situation in which the polluted parcel is an infinitely polluted parcel (Eq. 2.12). In this situation, only the clean parcel properties, $r_{lc\max}$ and $z_{c\max}$, impact the invigoration since the polluted parcel properties, $r_{lc\max}$ and $z_{c\max}$, are zero. Also, recall that the initial temperature, water vapor mixing ratio, and vertical velocity of the two parcels are assumed to be identical, and that the parcels are both rising in the same environment. First, according to Eq. 2.12, the invigoration of the infinitely polluted parcel relative to the clean parcel increases as $z_{c\max}$ increases at levels below $z_{c\max}$. This is the expected behavior since as $z_{c\max}$ increases, $S_{c\max}$ also increases, more water is retained as vapor and less latent heat is released in the clean parcel. However, since the maximum supersaturation often occurs within a few tens of meters above cloud base, the invigoration that occurs below $z_{c\max}$ will be small

compared to the invigoration achieved at higher heights. Above $z_{c\max}$, the invigoration in terms of kinetic energy (Eq. 2.12) is composed of two terms, one proportional to $-z_{c\max}^2$, and one proportional to $z \cdot z_{c\max}$ (recall that $r_{lc\max}$ is linearly proportional to $z_{c\max}$). This latter term will always be the larger one in absolute magnitude (since by construction $z > z_{c\max}$ in this regime) and will become increasingly dominant with height above cloud base. Therefore, at heights just above $z_{c\max}$, the dependency of ΔK on $z_{c\max}$ will appear quadratic, and as z increases further, the dependency will become more linear. These two terms also show that the invigoration in terms of kinetic energy increases linearly with height above $z_{c\max}$. Lastly, Eqs. 2.11 and 2.12 both indicate that the invigoration will be only weakly dependent on the initial buoyancy of the parcels through coefficient a (assuming that the initial vertical velocity is the same for both parcels).

A comparison of the change in kinetic energy, or the invigoration of an infinitely polluted parcel relative to a clean parcel, between the theoretical predictions and the parcel model simulations described in section 2.3 is shown in Figure 2.5 as a function of $z_{c\max}$, $S_{c\max}$, and $r_{lc\max}$ for four different levels above cloud base. To calculate the theoretical prediction in each of the subplots a-c in Figure 2.5, we rewrote Eq. 2.12 so that it was only a function of z and the $c$max variable of interest. For example, in Figure 2.5a, $r_{lc\max}$ in Eq. 2.12 is replaced with $r_{lc\max} = A_1 A_2^{-1} C_3 C_2^{-1} z_{c\max}$ (P13) so that only $z_{c\max}$ appears in the equation. The values of the $c$max variables are taken from the parcel model simulations rather than calculating them from the parcel initial conditions using Eqs. 32-34 in P13 (section 2.7). While the latter method is possible, we wish to assess the error associated with the theoretical prediction developed here, and not the error associated with calculating the $c$max variables from initial conditions that was developed by P13.

The magnitude of the invigoration simulated by the parcel model behaves in much the way as predicted by the theoretical model described above. Both the parcel model and the theoretical prediction show decreasing sensitivity of the invigoration to $z_{c\max}$, $S_{c\max}$, and $r_{lc\max}$ as these quantities increase (i.e. as the clean parcel becomes cleaner), and that the sensitivity to these quantities becomes more linear as the height above cloud base increases.

The error made by the theoretical prediction using $z_{c\max}$ and $S_{c\max}$ (Fig. 2.5d-e) is largest for high aerosol concentration in the clean parcel (low $z_{c\max}$ and low $S_{c\max}$). At these aerosol concentrations, using $r_{lc\max}$ as the prediction variable results in the lowest errors, which are 25% or less (Fig. 2.5f) in nearly all cases. For low aerosol concentrations in the clean parcel, $z_{c\max}$ and $S_{c\max}$ perform better than $r_{lc\max}$. The error is about 40% or less when using $z_{c\max}$ as a predictor, and $S_{c\max}$ performs best at the lowest aerosol concentration tested where the error is about 30% or less. For all predictors, the errors are lower when the environmental temperature is warmer. Overall, Figure 2.5 indicates that the theoretical prediction works well for at least one of the prediction variables over a range of aerosol concentrations and environmental conditions. Furthermore, except at 250m above cloud base or less, the errors are positive, indicating that the theoretical prediction gives an upper limit to the magnitude of the invigoration. The theoretical prediction can also be expected to give an upper limit since processes that have been neglected here, including entrainment and the vertical pressure gradient force, are expected to further decrease the magnitude of invigoration.

2.5 Exploration of the parameter space

Since the theoretical prediction has been shown to perform well in comparison with the parcel model, we can use the simplified theoretical prediction (Eq. 2.12) to easily explore the

sensitivity of condensational invigoration to the initial cloud base condition T_0 and the environmental condition $\overline{T}_v$. Figure 2.6 shows the change in kinetic energy at 1km above cloud base between a clean parcel and an infinitely polluted parcel as a function of the cloud base temperature (T_0) and the initial virtual temperature perturbation ($T_{v0} - \overline{T_{v0}}$) for low (Fig. 2.6a-c) and high (Fig. 2.6d-f) values of $z_{c\max}$, $S_{c\max}$, and $r_{lc\max}$, where low and high values of these parameters are based on Figure 2.5. Low values of $z_{c\max}$, $S_{c\max}$, and $r_{lc\max}$ correspond to high values of cloud droplet concentration and low values of cloud base vertical velocity in the clean parcel whereas high values of $z_{c\max}$, $S_{c\max}$, and $r_{lc\max}$ correspond to low values of cloud droplet concentration and high values of cloud base vertical velocity (Fig. 2.2). Recall also that although the theoretical prediction assumes an isothermal atmosphere, the results discussed here are applicable to the warm phase of all convective clouds within the first kilometer above cloud base since the sensitivity of the prediction to the environmental profile of temperature is minimal (Fig. 2.4)

The initial virtual temperature perturbation is proportional to the parcel's initial buoyancy (Eq. 2.1). Figure 2.6 uses Eq. 2.12 to show that the change in kinetic energy only weakly increases as the initial buoyancy increases (by at most by 2% for a perturbation of 5K) for all cloud base temperatures and for both low and high values of $z_{c\max}$, $S_{c\max}$, and $r_{lc\max}$. To explain the lack of sensitivity to buoyancy, we will consider just the case of constant $r_{lc\max}$. The amount of latent heat released, which drives the magnitude of invigoration, is directly proportional to the amount of liquid that has condensed. For a constant $r_{lc\max}$, the total amount of latent heat released by the time $z_{c\max}$ is reached is also constant for a given cloud base temperature, and thus the magnitude of invigoration at $z_{c\max}$ is not be expected to depend strongly on the buoyancy. However, note that in order to maintain a constant $r_{lc\max}$ when buoyancy is increased, the number

of cloud droplets must be increased or the cloud base velocity must be decreased, or a combination of the two. This is because when buoyancy is increased, the vertical velocity will increase more quickly and there will be less time for condensation. Increasing the droplet concentration will speed the condensation rate. Decreasing the cloud base vertical velocity will increase the available time for condensation – both options have the effect of compensating for the decreased available time for condensation that is induced by higher buoyancy such that $r_{lc\max}$ can remain constant. The invigoration, in terms of added kinetic energy, increases with buoyancy because, above $z_{c\max}$, higher vertical velocity induced by the higher buoyancy will reduce the time available for condensation and the resultant latent heat release in the clean parcel (in the infinitely polluted parcel, condensation is instantaneous so the amount of condensation is unchanged). Thus the difference in kinetic energy between the infinitely polluted parcel and the clean parcel will be increased. A similar line of reasoning applies for the case of a constant $z_{c\max}$ or $S_{c\max}$.

On the other hand, the invigoration in terms of kinetic energy changes more substantially as the cloud base temperature increases. For constant values of $z_{c\max}$ or $S_{c\max}$ (Fig. 2.6a-b, d-e), the invigoration increases as the cloud base temperature increases, by up to 50% for $z_{c\max}$ and by up to 80% for $S_{c\max}$. These increases occur primarily because at warmer temperatures, the saturation water vapor mixing ratio is higher, and thus greater differences in condensed water between clean and polluted parcels occur for the same supersaturation. The opposite trend is seen when $r_{lc\max}$ is held constant (Fig. 2.6c, f). In this case the invigoration magnitude decreases as the cloud base temperature increases, but only by 7% or less. By holding $r_{lc\max}$ constant, the difference in condensed water, which is the main driver behind the invigoration magnitude, is highly constrained. Furthermore, in order to maintain a constant $r_{lc\max}$ as the cloud base

temperature is increased, the maximum supersaturation ($S_{c\max}$) must be reduced and occur at a lower height ($z_{c\max}$). These qualitative relationships can be inferred from Figure 2.3. In other words, at higher temperatures, water is condensed more quickly and as a result, the height of maximum supersaturation decreases. It is this reduction in $S_{c\max}$ and $z_{c\max}$ that leads to a small decrease in the invigoration as the cloud base temperature increases in Fig. 2.6c and 2.6f.

While the focus here has been on invigoration in terms of kinetic energy, invigoration is more traditionally described in terms of vertical velocity. There is no way to simply convert the change in kinetic energy derived above to a change in vertical velocity. One of the vertical velocity values must already be known in order to obtain the vertical velocity difference from the expression for the kinetic energy difference (Eq. 2.11 or 2.12). In field measurements or in a numerical model, this is not an issue, since vertical velocity and not kinetic energy is typically the quantity that is measured or predicted. Rather than derive a new expression for the change in vertical velocity, which would not be as simple as it has been for kinetic energy (see the discussion in section 2.2), we specify a value of the vertical velocity for the clean parcel at the height above cloud base of interest, and calculate the change in vertical velocity between that clean parcel and an infinitely polluted parcel from the kinetic energy difference.

Figure 2.7 shows these vertical velocity differences as a function of cloud base temperature and the clean parcel vertical velocity at 1km above cloud base for the same low and high values of $z_{c\max}$, $S_{c\max}$, and $r_{lc\max}$ as in Figure 2.6. As the cloud base temperature increases, the change in vertical velocity increases for constant $z_{c\max}$ or $S_{c\max}$ (Fig. 2.7a-b, d-e) and decreases for constant $r_{lc\max}$ (Fig. 2.7c, f) as we would expect based on the kinetic energy results (Fig. 2.6). However, the change in vertical velocity is more strongly dependent on the vertical velocity of the clean parcel at 1km than on the cloud base temperature. As the clean parcel

velocity increases, the invigoration in terms of vertical velocity rapidly decreases. Thus, clean clouds that are already vigorous are less sensitive to changes in $z_{c\max}$, $S_{c\max}$, and $r_{lc\max}$ in terms of vertical velocity than clouds that have small updraft speeds. This result supports conclusions of previous studies that have examined the sensitivity of aerosol-induced invigoration to different environmental stability conditions (Storer et al. 2014; Stolz et al. 2015)

Figures 2.6 and 2.7 are also useful for investigating the upper limit of invigoration. Recall from Figure 2.5 that $S_{c\max}$ gives the lowest errors for high values of $z_{c\max}$, $S_{c\max}$, and $r_{lc\max}$ (low values of aerosol concentration in the clean parcel). Figures 2.6e and 2.7e indicate that the maximum change in kinetic energy between a clean and infinitely polluted parcel for the conditions considered here is about 12 $m^2 s^{-2}$ and that the maximum change in vertical velocity is about 4.5 m s^{-1}, respectively. For more typical values of aerosol concentration, the invigoration in terms of vertical velocity is usually less than 2 m s^{-1} (Fig. 2.7a-c). However, our analysis does not account for processes such as entrainment and mixing which will likely reduce the magnitude of invigoration, particularly in shallow clouds, which tend to be more dilute than deep convective cores since shallow clouds are narrower (e.g. Simpson et al. 1965). Therefore, the analysis should not be interpreted as the expected magnitude of invigoration in real clouds, but rather as an upper estimate of this magnitude.

2.6 Conclusions

Condensational invigoration is a phenomenon that has been discussed previously by the community, particularly in the context of aerosol-cloud interactions (Kogan and Martin 1994; Khain et al. 2004, 2005, 2008; Lebo and Seinfeld 2011; Storer and van den Heever 2013; Koren et al. 2014; Seiki and Nakajima et al. 2014). However, the magnitude of condensational

invigoration is not well known and is typically only discussed in specific cases or idealized studies. In this study, we developed an analytical expression to describe the change in kinetic energy between a clean and polluted parcel in order to explore the magnitude of condensational invigoration which is applicable to any warm phase convection, whether it be shallow convection or deep convection that goes on to have an ice phase. The expression relied on the work of Pinsky et al. (2013) in order to describe the evolution of liquid water with height.

The new analytical expression revealed that the change in kinetic energy, which is a quantity that can be used to quantify the magnitude of condensational invigoration, between an infinitely polluted parcel and a clean parcel at a given height above cloud base can be expressed as a function of the maximum supersaturation for the clean parcel ($S_{c\max}$), the height at which that maximum supersaturation occurs ($z_{c\max}$), or the liquid water mixing ratio at that height ($r_{lc\max}$). When written this way, the analytical expression was not explicitly dependent on the initial aerosol concentration and the cloud base vertical velocity of the clean parcel. Furthermore, it was shown that the change in kinetic energy is minimally sensitive to the environmental profile of temperature, and thus the analytical expression can be applied to both shallow clouds and the warm phase of deep convective clouds. Predictions made by our analytical expression for the change in kinetic energy were compared to results from parcel model simulations. It was seen that the errors made by the analytical expression at heights of up to 1 km above cloud base were 25% or less for at least one of the three possible prediction variables, for nearly all of the parcel model tests.

We used the new analytical expression to explore the sensitivity of condensational invigoration to the cloud base temperature and the initial buoyancy of the cloud. The invigoration, measured in terms of kinetic energy or vertical velocity and expressed as a function

of $z_{c\max}$, $S_{c\max}$, and $r_{lc\max}$, was nearly insensitive to the initial buoyancy of the cloud parcel, and was more strongly dependent on the cloud base temperature. Analysis at 1km above cloud base showed that the change in kinetic energy varied by up to 80% for typical values of cloud base temperature. This added kinetic energy increases linearly with height above the height of maximum supersaturation. The analytical expression was then used to also determine the magnitude of invigoration in terms of vertical velocity. In order to do so, the velocity of the clean parcel was specified and as a result, a range of values was possible for the change in vertical velocity given a particular change in the kinetic energy. Our analysis indicated that the change in vertical velocity decreased as the vertical velocity itself increased, but can be as much as about 4.5 m s^{-1} at 1km above cloud base for an ultra-clean cloud. More typical values of invigoration are less than 2 m s^{-1}. As a consequence, condensational invigoration is likely to be a minor effect in most situations. The estimates of invigoration developed here are expected to be an upper limit on the change in velocity realized in real clouds, since we expect that entrainment and the vertical pressure gradient force would decrease the magnitude of condensational invigoration. Future work should address how mixing and other processes, such as rain formation and condensate unloading, further alter the invigoration magnitude.

2.7 Appendix A

The dependencies of $z_{\max}$, $S_{\max}$, and $r_{l\max}$ on droplet concentration (N), cloud base vertical velocity (w), cloud base temperature (T), and cloud base pressure (p) were developed by P13. Their equations (32-34) are reproduced here for reference.

$$S_{\max} = C_1 \left(\frac{FA_1}{3}\right)^{\frac{3}{4}} \left(\frac{3\rho_a}{4\pi\rho_w A_2}\right)^{\frac{1}{2}} w^{\frac{3}{4}} N^{-\frac{1}{2}}$$

$$z_{\max} = C_2 {A_1}^{-1/4} \left(\frac{F}{3}\right)^{3/4} \left(\frac{3\rho_a}{4\pi\rho_w A_2}\right)^{1/2} w^{3/4} N^{-1/2}$$

$$q_{\max} = C_3 \left(\frac{FA_1}{3}\right)^{3/4} \left(\frac{3\rho_a}{4\pi\rho_w {A_2}^3}\right)^{1/2} w^{3/4} N^{-1/2}$$

where $F = \frac{\rho_w L^2}{k_a R_v T^2} + \frac{\rho_w R_v T}{e_w(T) D}$

and ρ_a is air density, ρ_w is water density, k_a is the coefficient of air heat conductivity, e_w is the saturation vapor pressure over a flat surface of water, and D is the coefficient of water vapor diffusion. Other symbols are defined in the main text.

2.8 Appendix B

The parcel model has been slightly modified for the current study. As before modification, the model prognoses the height, pressure, temperature, and droplet diameter of the initially deliquesced aerosol particle distribution using the variable coordinate ordinary differential equation solver (VODES; Brown et al. 1989), which is an iterative method for solving the equations. The only microphysical process that is represented in the parcel model is condensation. Collision-coalescence, ice phase processes, precipitation fallout, and the effects of entrainment are not included. A prognostic equation for vertical velocity has been added in order to allow for latent heating and buoyancy feedbacks to the parcel vertical velocity. The vertical velocity (w) is predicted using the Reynolds-averaged buoyancy term as follows:

$$\frac{\partial w}{\partial t} = g\left(\frac{T_v - \overline{T_v}}{\overline{T_v}} - r_l\right)$$

where $T_v = T\dfrac{1 + r_v/\varepsilon}{1 + r_v}$

and where t is time, and all other symbols have the same definition as in the main body of the text.

Finally, the saturation ratio is diagnosed rather than predicted. Since the mixing ratio of the total water (vapor plus liquid) is known and must remain constant in the absence of entrainment, the vapor mixing ratio can be diagnosed from the predicted liquid water mixing ratio. The latter is determined from the size and number distributions of the droplets. The saturation vapor mixing ratio is determined from the prognosed parcel temperature. The actual vapor mixing ratio and the saturated vapor mixing ratio are then used to calculate the saturation ratio, and hence the supersaturation.

A saturation adjustment option was added to the parcel model in order to conduct the experiments of interest. When this option is used, the model behaves as described above while the saturation ratio is less than 1. When the saturation ratio is greater than 1, the height, pressure, and temperature is first updated assuming dry adiabatic processes. Then an iterative method is used to calculate the amount of condensed water and latent heating. The equations for the moist physics are iterated until the saturation ratio is 1 with an absolute tolerance of 10^{-8}.

2.9 Figures

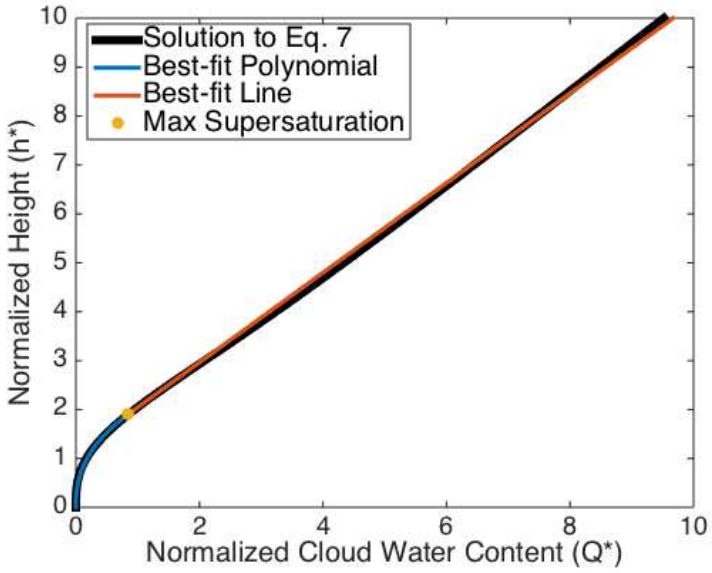

Figure 2.1. The thick black line shows the solution to Eq. 2.7. The blue and red lines show the best-fit piece-wise function (Eq. 2.8) to Eq. 2.7, and the yellow filled-circle indicates the point of maximum supersaturation that separates the two portions of the piece-wise function.

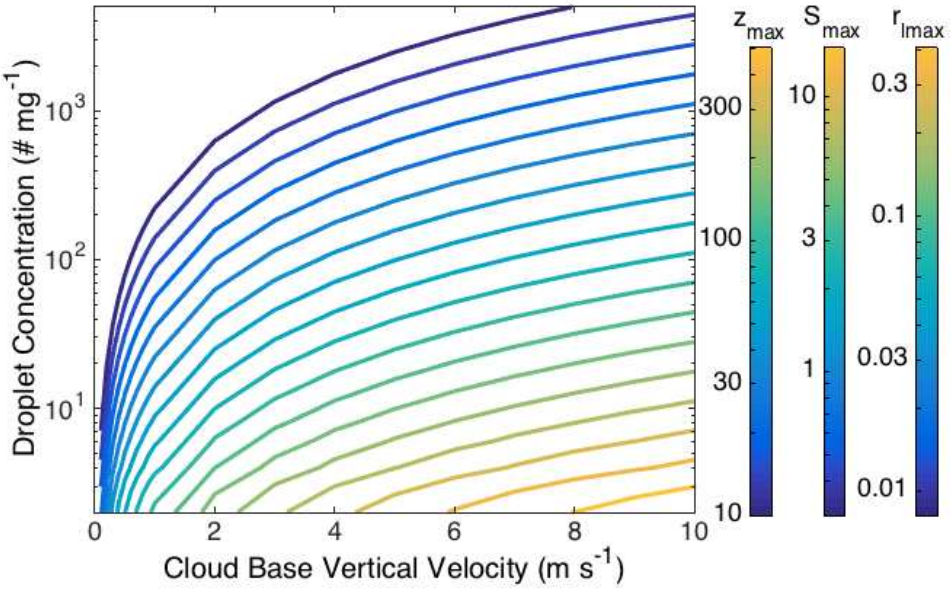

Figure 2.2. z_{max} (m), S_{max} (%), and r_{lmax} (g kg^{-1}) as a function of cloud droplet concentration and cloud base vertical velocity for a cloud base temperature of 10°C and cloud base pressure of 950mb.

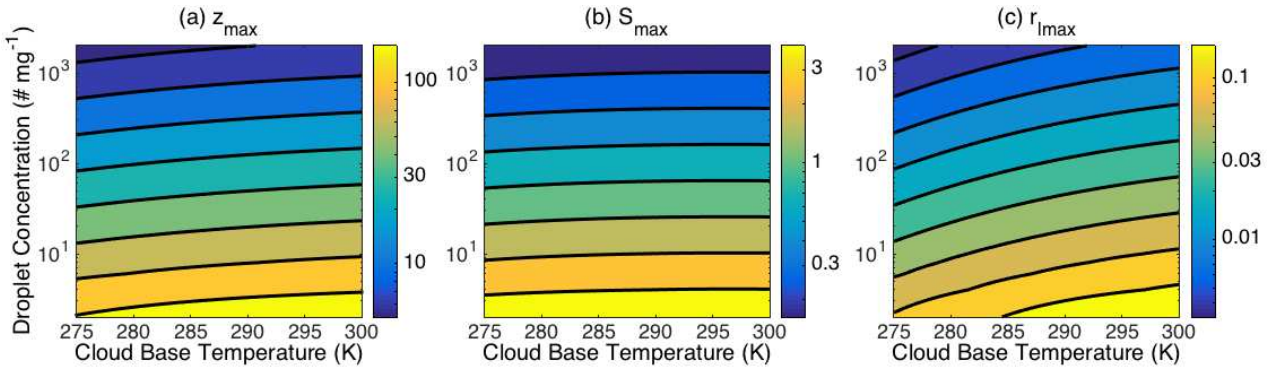

Figure 2.3. (a) z_{max} (m), (b) S_{max} (%), and (c) r_{lmax} (g kg^{-1}) as a function of droplet concentration and cloud base temperature for a cloud base vertical velocity of 2 m s^{-1} and a cloud base pressure of 950mb.

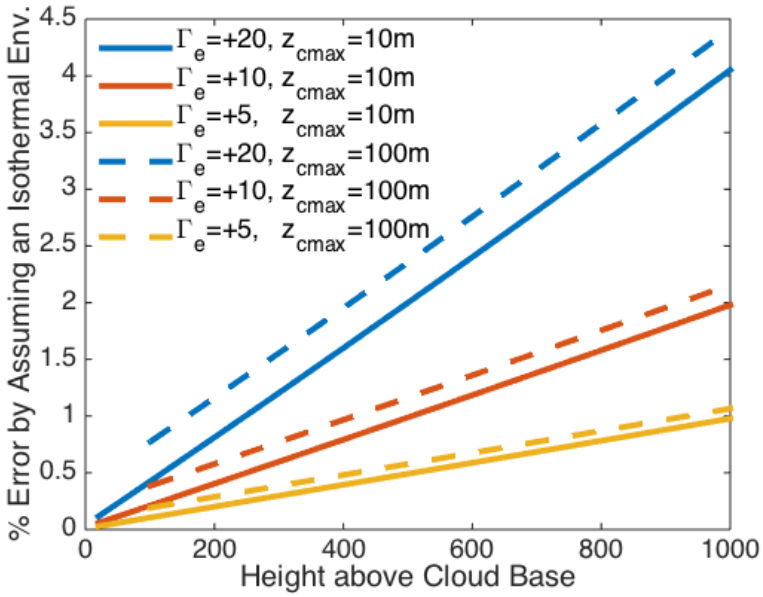

Figure 2.4. Percent error in Eq. 2.11 due to assuming an isothermal environmental lapse rate for a range of non-isothermal environmental lapse rates (K km^{-1}). Solid lines show the error for z_{cmax} =10m, and dashed lines show the error for z_{cmax} =100m.

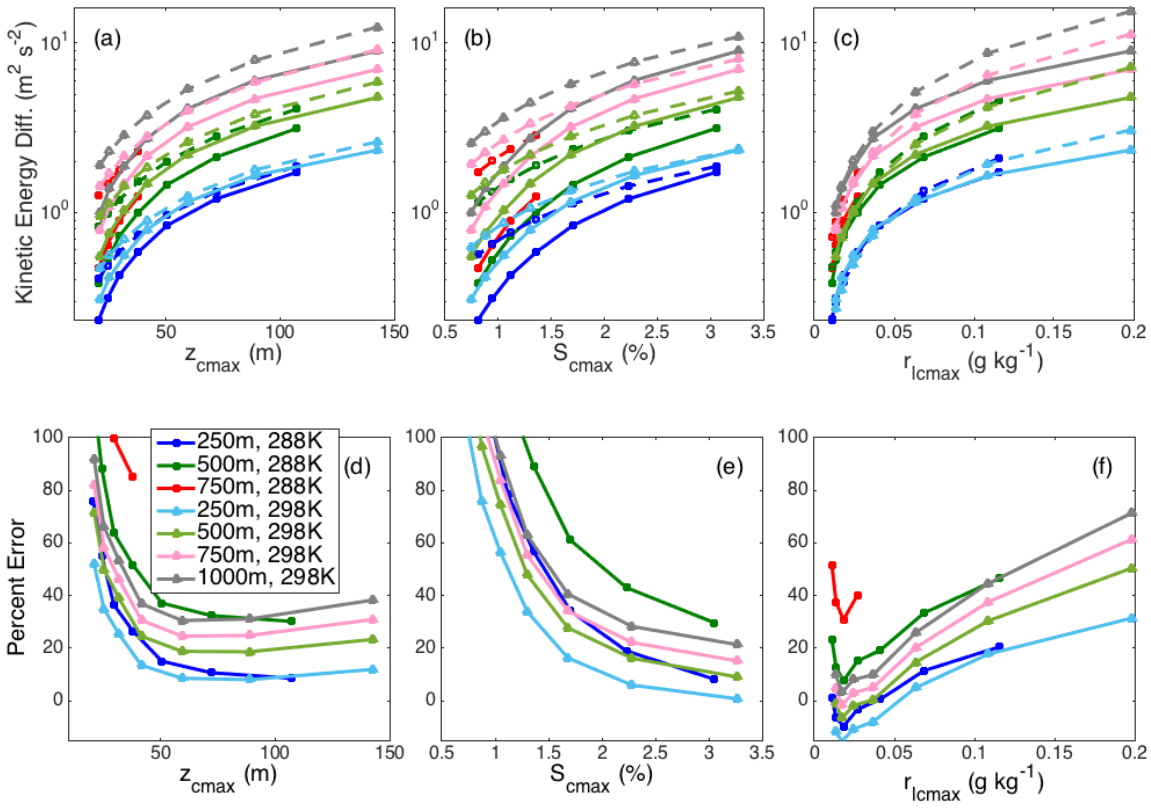

Figure 2.5. (a-c) Kinetic energy difference between an infinitely polluted parcel and clean parcels as a function of (a) z_{cmax}, (b) S_{cmax}, and (c) r_{lcmax}. Solid lines show results from the parcel model and dashed lines show results from the theoretical prediction (Eq. 2.12) for four different levels above cloud base (colors). Dark colors (blue, green, red) show results where the environmental temperature is 288K, and light colors (light blue, light green, pink, gray) show results where the environmental temperature is 298K. (d-f) As in (a-c) except showing the percent error of the theoretical prediction. The dots indicate the values for the seven different aerosol concentrations used in the parcel model simulations described in section 2.3. Note that larger values of z_{cmax}, S_{cmax}, and r_{lcmax} correspond to lower aerosol concentrations.

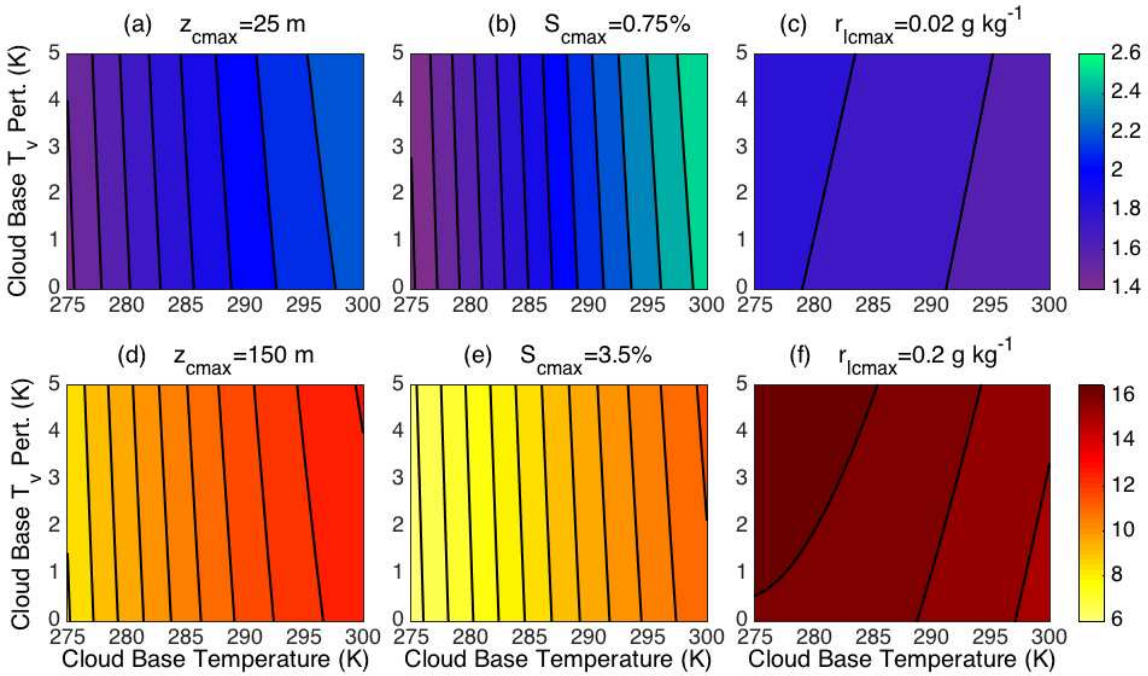

Figure 2.6. Change in kinetic energy (m^2s^{-2}) between an infinitely polluted parcel and a clean parcel at 1km above cloud base as a function of cloud base temperature and the cloud base virtual temperature perturbation where (a, d) z_{cmax} is held constant, (b, e) S_{cmax} is held constant, and (c, f) r_{lcmax} is held constant. In (a-c) the contour interval is 0.1 m^2s^{-2} and in (d-f) it is 0.5 $m^2 s^{-2}$.

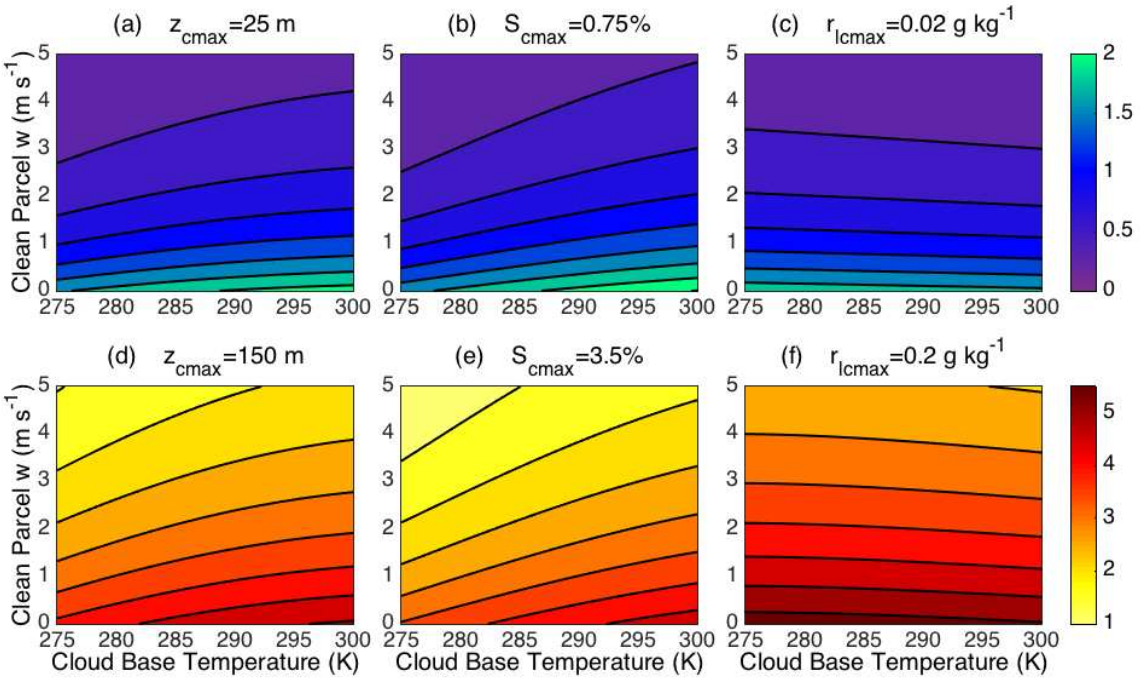

Figure 2.7. Change in vertical velocity between a clean parcel and an infinitely polluted parcel at 1km above cloud base as a function of cloud base temperature and the vertical velocity of the clean parcel at 1 km where (a, d) z_{cmax} is held constant, (b, e) S_{cmax} is held constant, and (c, f) r_{lcmax} is held constant. The contour interval is 0.25 m s^{-1} in (a-c) and is 0.5 m s^{-1} in (d-f).

3. MAKE IT A DOUBLE? SOBERING RESULTS FROM SINGLE- AND DOUBLE-MOMENT MICROPHYSICS SIMULATIONS[2]

3.1 Introduction

The parameterization of cloud microphysics has long been one of the greatest challenges for atmospheric models with grid spacings of a few kilometers or less. Due to the small length scale at which microphysical processes occur (microns-millimeters) and the sheer number of cloud droplets, ice crystals, and rain drops (up to ~10000 cm^{-3}), it is not feasible to simulate microphysical processes explicitly in domains with volumes of even a few cubic kilometers given current computational resources. Many microphysical parameterization frameworks, wherein microphysical processes are not explicitly simulated, have therefore been designed to circumvent this problem, the two most frequently used today being single-moment and double-moment bulk schemes.

The goal of this paper is to motivate the use of double-moment schemes over single-moment schemes. This will be done in several ways. First, here in the introduction, an overview of microphysics schemes is given, and the past work comparing single- and double-moment schemes is presented. In section 3.2, the sensitivity of different microphysical processes to fixed parameters that are necessary in single-moment schemes will be investigated from a simple theoretical perspective. In section 3.3, idealized simulations of convection using a single-moment scheme are presented to show the range of results that can be achieved by simply changing the fixed parameters. Though the differences obtained in simulations using single- and

[2] This chapter is previously published in the peer-reviewed literature. Igel, A. L., M. R. Igel, and S. C. van den Heever, 2015: Make it a double? Sobering results from single- and double-moment microphysics simulations. *J. Atmos. Sci.* 72, 910-925. doi: http://dx.doi.org/10.1175/JAS-D-14-0107.1.

double-moment schemes have been described in the past, less attention has been given to the range of results that can achieved by varying the fixed parameters within the same single-moment scheme such as has been done by Ferrier et al. (1995), Gilmore et al. (2004), van den Heever and Cotton (2004) Yussouf and Stensrud (2012), and Adams-Selin et al. (2013). The range of results will be demonstrated for a simple simulation in this study to advocate further for the phasing out of single-moment schemes, particularly when conducting research simulations. Lastly, comparisons between simulations run with both single- and double-moment schemes for a system in radiative-convective equilibrium (RCE) are presented in section 2.4. Basic comparisons are made between observations and the RCE simulations that suggest that the double-moment simulations capture the tropical cloud and precipitation characteristics more realistically than single-moment schemes.

Single-moment schemes require minimal memory and computational burden compared to more complex schemes. Many single-moment schemes predict the mixing ratio of each hydrometeor species and keep either the mean diameter or number concentration fixed, such that the other can be diagnosed (Lin et al. 1983; Walko et al. 1995; Straka and Mansell 2005; Hong and Lim 2006). Depending on the complexity of the scheme, the size distribution of each species can be monodisperse, or a distribution shape may be assumed. In the case of an assumed exponential distribution, the intercept parameter is commonly held constant rather than the number concentration or the mean diameter. Irrespectively, there is a fixed relationship between number concentration, diameter, and other specified parameters of the assumed distribution. Though not common, some schemes diagnose the intercept parameter based on environmental conditions so that it can vary in space and time (Hong et al. 2004; Thompson et al. 2004). Nonetheless, the inability of single-moment schemes to allow the number concentration and

mean diameter of hydrometeors to vary independently severely limits their ability to simulate clouds with characteristics consistent with observations across a wide range of atmospheric conditions.

Double-moment schemes, as their name implies, predict two moments of the distribution, usually the mixing ratio and number concentration of each hydrometeor species (Ferrier 1994; Meyers et al. 1997; Milbrandt and Yau 2005a; Morrison et al. 2005; Seifert and Beheng 2006; Mansell et al. 2010). Some schemes are mixed-moment with one moment of some hydrometeor species being predicted, such as cloud water and ice crystals, and two moments of other species being predicted (Thompson et al. 2008; Hong et al. 2010). Double-moment schemes allow for a more realistic representation of clouds, since both number concentration and diameter are allowed to vary independently in space; however, the shape of the distributions usually remains fixed. A fixed distribution shape is not always the case; Milbrandt and Yau (2005), for example, developed diagnostic equations for the shape parameter of the precipitating hydrometeors.

When both the mixing ratio and number concentration of a hydrometeor species are predicted, the representation of many microphysical processes can be improved. Two such processes, condensation and collision-coalescence are discussed below in section 3.2. Another process that is improved is sedimentation, or the falling of hydrometeors (Wacker and Seifert 2001; Milbrandt and Yau 2005a; Milbrandt and McTaggart-Cowan 2010). In the real atmosphere, large, more massive drops fall faster than small drops which leads to an effect known as size sorting. Size sorting cannot be predicted in a single-moment scheme unless one of the fixed parameters is allowed to vary with height (Milbrandt and McTaggart-Cowan 2010) but can be predicted in any multi-moment scheme by using different fall velocities for the different predicted moments of the hydrometeor size distribution. Though generally sedimentation is

improved in double-moment schemes over single-moment schemes, double-moment schemes tend to be overly aggressive in their sorting, and methods have been suggested to ameliorate this problem (Milbrandt and Yau 2005a; Wacker and Lüpkes 2009; Mansell 2010; Milbrandt and McTaggart-Cowan 2010).

While the representation of microphysical processes can be improved since more variables exist in double-moment schemes than single-moment schemes to describe the cloud properties, new assumptions must also be made. For example, since the predicted mean diameter of rain can reach large values, the raindrop break-up process must be parameterized. However this is a poorly understood process, and simulations can be sensitive to how it is implemented (Morrison and Milbrandt 2011; Morrison et al. 2012; Van Weverberg et al. 2014). Also, the number and size of raindrops to create during processes such as hail shedding and ice melting need to be parameterized, but is not constrained well by observations (see e.g. Meyers et al. 1997). Uncertainties exist regarding how many cloud droplets and ice crystals to create upon nucleation. Such decisions usually require some assumptions about the aerosol particle distribution. The Hallett-Mossop ice multiplication process is another poorly understood ice nucleation mechanism that can have large impacts on cloud properties depending on how it is parameterized (Connolly et al. 2006). These are just some of the problems that must be addressed in double-moment schemes but not in single-moment schemes.

Despite these new assumptions, double-moment schemes have been shown to be generally more successful than single-moment schemes in reproducing observations of a number of different cloud systems including squall lines (Morrison et al. 2009; Van Weverberg et al. 2012; Baba and Takahashi 2013), supercells (Dawson et al. 2010; Jung et al. 2012), scattered and isolated convection (Swann 1998), mesoscale cloud systems (Lee and Donner 2011), tropical

cyclones (Jin et al. 2014), Arctic mixed-phase stratus clouds (Luo et al. 2008), orographic clouds (Milbrandt et al. 2010), Colorado winter storms (Reisner et al. 1998), and synoptic-scale snow events (though single-moment schemes with diagnosed intercept parameters did well) (Molthan and Colle 2012). These studies have shown improvements in the representation of a wide range of atmospheric variables including liquid and ice water contents, precipitation, radiative fluxes, cold pool properties, storm morphology, and dynamics with the use of double-moment schemes. Van Weverberg et al. (2014) found that the two kinds of schemes do equally well when simulating very intense precipitation due to the poor representation of rain break-up in double-moment schemes. Relatively few studies have shown no improvement with the use of double-moment schemes (Van Weverberg et al. 2013; Wu and Petty 2010).

The improvement that is usually found in simulations when using double-moment schemes rather than single-moment schemes does come with increased computation time and memory requirements. That being said, computational capabilities have been rapidly increasing and it is suggested here that simulations run for research purposes should no longer use single-moment schemes. *Regardless of whether the focus of a given study is on microphysical processes or not*, the choice of microphysics scheme will influence the simulated outcome through a multitude of dynamic, radiation, thermodynamic, and microphysical feedback processes. Therefore double-moment parameterizations should be chosen over single-moment parameterizations whenever possible in order to obtain better results as demonstrated by the studies cited above and as will be demonstrated below in the current study.

It should be noted that other kinds of microphysics parameterizations exist for cloud-resolving models, but are less common. Triple-moment schemes (Milbrandt and Yau 2005b) predict the shape parameter of the gamma probability distribution using prognostic equations for

the radar reflectivity, which is the sixth moment of the distribution. Spectral bin schemes (Reisin et al. 1996; Ovtchinnikov and Kogan 2000; Rasmussen et al. 2002; Khain et al. 2004; Lebo and Seinfeld 2011) avoid the need to assume a size distribution function by dividing the distribution of a species into discrete bins and prognosing the number and/or the mass mixing ratio of each bin separately. Uniquely, Onishi and Takahashi (2012) developed a scheme with a bin representation of the warm phase species, and a two-moment bulk representation of the ice phase species. Bin-emulating schemes (Feingold et al. 1998; Saleeby and Cotton 2004, 2008; Saleeby and van den Heever 2013) have been designed to take advantage of both bulk and bin schemes – they are double-moment schemes that use lookup tables for some microphysical process rates that have been generated from bin schemes. Finally, the superdroplet method of parameterizing microphysics (Shima et al. 2009) uses a novel approach in which the position and physical properties of a collection of droplets with identical attributes (or a superdroplet) are prognosed. To date, the parameterization has only been developed for the warm phase. These kinds of schemes can be good alternatives to single- and double-moment schemes depending on the application, although all of them are more computationally expensive.

3.2 Theoretical Considerations

In this section, the sensitivity of microphysical processes to fixed hydrometeor distribution parameters is explored. For simplicity, the focus of the discussion in this section is on the representation of warm phase microphysical processes in single-moment schemes, specifically condensation and autoconversion. However, similar reasoning could just as easily be applied to the ice phase for deposition, riming, and other collection processes. Note that the processes discussed have more complex representations in most microphysical schemes than are

described here. This section is only intended to provide a qualitative sense for the sensitivity of each process.

Condensation is the first process considered here. In some models, a saturation adjustment scheme is employed to calculate condensation. In such schemes, any supersaturation that develops is depleted immediately to form liquid water. When using saturation adjustment schemes, both single- and double-moment schemes will predict the same amount of condensation given the same supersaturation at any grid point. Lebo et al. (2012) have recently discussed saturation adjustment schemes in much more depth.

In other models, saturation adjustment is not implemented, in which case the condensation equation is represented explicitly in some form. This form will depend on the assumed size distribution of the hydrometeors. The gamma size distribution is commonly assumed such that the mixing ratio (r) can be expressed as:

$$r = \frac{N_T}{\rho_a}\frac{\pi}{6}\left(\frac{\overline{D}}{\nu}\right)^3 \frac{\Gamma(\nu+3)}{\Gamma(\nu)} \tag{3.1}$$

(e.g. Walko et al. 1995) where N_T is the total number concentration of droplets, $\overline{D}$ is the mean number diameter, ν is the distribution shape parameter, and ρ_a is air density. If ν=1, the distribution is equivalent to a Marshall-Palmer distribution. Following Walko et al. (1995) and neglecting the effects of ventilation, the equation for the rate of condensation (C; the time rate of change of the hydrometeor mass mixing ratio) can be expressed simply as

$$C = \frac{\partial r}{\partial t} = 2\pi(S-1)GN_T\overline{D} \tag{3.2}$$

where S is the saturation ratio and G is a function of temperature and pressure that represents the impacts of latent heat release and other nonlinearities, the specifics of which are not germane to the discussion.

These equations can be used to show how the properties of a distribution will impact condensation rates in a single-moment scheme. It can be seen from Eq. 3.1 that for a fixed mixing ratio and a fixed shape parameter $N_T \propto \overline{D}^{-3}$. By substituting this relationship into Eq. 3.2 it can be shown that $C \propto \overline{D}^{-2}$ for a fixed diameter or that $C \propto {N_T}^{2/3}$ for a fixed number concentration, all else being equal. The different powers on diameter and number concentration in these simple relationships indicate that the condensation rate will be comparatively more sensitive to the choice of fixed diameter. For example, for a doubling in the choice of fixed diameter, the condensation rate will be reduced by a factor of 4. On the other hand, a doubling of the fixed number concentration will increase condensation by only a factor of 1.6. Thus, changing either parameter will result in significant changes to the condensation rate, with the rate being more sensitive to changes in mean diameter. While such variability of the diameter and number concentration is common in real-world clouds, it *cannot* be represented by single-moment schemes. It should be noted though that when the supersaturation is low enough to be almost entirely consumed in one time step, saturation adjustment and supersaturation allowing condensation schemes will give very similar answers and the sensitivity to fixed parameters will be reduced.

The sensitivity of collision-coalescence to the choice of the fixed parameter in single-moment schemes is more difficult to determine because there are many different ways in which this process has been parameterized. Sophisticated Kessler-type parameterizations (e.g. Manton and Cotton 1977; Baker 1993; Boucher et al. 1995; Liu and Daum 2004) show the autoconversion rate to be proportional to ${N_T}^{-1/3}$ with no dependence on $\overline{D}$. Given that $N_T \propto \overline{D}^{-3}$, the autoconversion rate must be proportional to $\overline{D}$ if the diameter is fixed. Using the same example as before, doubling a fixed diameter will double the autoconversion rate, and

doubling a fixed number concentration will decrease the rate by a factor of 1.3, and by a factor of 2.2 for a tenfold increase. As with the condensation rate, we see that the autoconversion rate is more sensitive to a change in the mean diameter than to a change in the number concentration.

As shown above and summarized in Table 3.1, condensation and collision-coalescence have sensitivities to N_T and $\overline{D}$, although in the opposite sense. That is, growth of cloud water through condensation is increased and depletion through collision-coalescence is decreased for either a decrease in mean diameter or an increase in number concentration, assuming the same cloud water content. Therefore the two processes will feed back on one another to cause cloud water content to be even more disparate for a change in diameter or number concentration. For example, during a single model time step for a fixed cloud water content, a population of larger, less numerous cloud droplets ($\overline{D}\uparrow, N_T\downarrow$) will grow more slowly and have less additional mass at the end of the time step than a population of smaller, more numerous droplets ($\overline{D}\downarrow, N_T\uparrow$). During the same time step, this population of droplets ($\overline{D}\uparrow, N_T\downarrow$) will self-collect more quickly to create rain, further reducing the cloud water content relative to the scenario with smaller, more numerous droplets ($\overline{D}\downarrow, N_T\uparrow$). The processes act together to reduce the amount of cloud water present at the next model time step in ($\overline{D}\uparrow, N_T\downarrow$) relative to ($\overline{D}\downarrow, N_T\uparrow$). These processes and their subsequent feedbacks occur simply due to somewhat arbitrarily chosen microphysical parameters. Due to the nonlinear interaction of these processes as well as their different timescales, it is difficult to determine *a priori* how much quantities such as cloud water mixing ratio will vary due to changes in the fixed parameter values. The full implications of these changes in condensation and collision-coalescence rates and all other process rates, especially when multiple liquid and ice hydrometeors are being simulated, are best explored by running numerical simulations.

3.3 Simulations with Single-Moment Schemes

a. Simulation Design

To explore the range of results that can be obtained by simply changing the value of a fixed parameter, simulations of an idealized ordinary thunderstorm are run using the Regional Atmospheric Modeling System (RAMS) (Cotton et al. 2003). RAMS is used because its double-moment microphysics scheme (Meyers et al. 1997) can be run in a single-moment mode with either a fixed diameter or fixed number concentration. This capability allows for the exploration of the sensitivities of a simulation to either parameter. Many of the more recent advances to the RAMS double-moment scheme, such as its bin-emulating features and the second cloud mode (Saleeby and Cotton 2004, 2008; Saleeby and van den Heever 2013), were not used in order to keep the physics between the two schemes as similar as possible.

Four simulations of the idealized ordinary thunderstorm are performed: two with a fixed mean cloud droplet *diameter*, and two with a fixed cloud droplet *number concentration*. The other species (rain, snow, aggregates, graupel, and hail) each have a fixed mean diameter and thus are also run in single-moment mode. The settings for the fixed parameters in each simulation are summarized in Table 3.2. Pristine ice is run in double-moment mode in all simulations since the single-moment option has been deprecated in RAMS. All species have a fixed distribution shape parameter of 2. Though only the cloud droplet properties are being varied in these experiments, it is expected that there will be changes to both the warm and ice phases of the storm as a result since ice is often nucleated from and can grow through the collection of supercooled cloud droplets. Both phases will therefore be examined here.

The values chosen for the fixed cloud droplet parameters in these sensitivity tests are meant to be representative of lower and upper limits of values typically used in previous studies.

However, determining these limits is sometimes difficult as these values are frequently not reported in the literature. For the mean cloud droplet diameter, 5 and 25microns are chosen (referred to as D5 and D25, respectively), and for number concentration, 100 and 1000 mg^{-1} are selected (referred to as N100 and N1000, respectively). These values represent a reasonable range for the parameters based on observations (Pruppacher and Klett 2010).

In order to simulate an isolated, deep convective storm, the convective sounding of Weisman and Klemp (1982) is used to initialize the domain homogeneously horizontally. The horizontal wind is set to zero to simulate an ordinary thunderstorm rather than a supercell. The model domain is 200x200km in area with a 1 km horizontal grid spacing. Forty levels are used in the vertical dimension with a grid spacing of 100m at the surface being stretched to 1000m aloft with the model top at 23.3 km. The model time step was 5s. A 2K warm, square bubble, 20 x 20 km and 3 km deep, was used to initiate the convection.

b. Cloud Processes

Time series of cloud water growth (net condensation) and loss (autoconversion, accretion, riming) processes are shown in Fig. 3.1a along with the domain average cloud water path (Fig. 3.1b). From these figures, it is clear that changing the cloud droplet properties has an immediate impact on the condensation and collision-coalescence rates that lead to changes in the total cloud water content. As expected from the theory discussed above in section 3.2, a smaller cloud droplet diameter (D5) leads to initially higher condensation rates and lower collision-coalescence rates, resulting in a cloud water path that is ~6 times larger than that for D25. Also as expected, N1000 initially has a condensation rate ~3% higher than N100, though the absolute difference is small and cannot be seen in Fig. 3.1a (N100, N1000). The collision-coalescence

rate in N100 initially increases relative to N1000 as predicted by the theory presented in section 3.2. Overall, these changes in process rates result in the cloud water path being highest for D5 and lowest for D25, and cause the initial trends in precipitation (Fig. 3.1c) to follow those of collision-coalescence.

For the most part, the initial changes in process rates are half as large or less than were predicted by theory (see section 3.2), probably because the assumption of fixed cloud water content is no longer valid. For example, while for the same cloud water content fewer but larger cloud droplets will collect more quickly to form rain and lead to less cloud water at the next time step, having less cloud water at the next time step will slow the collision-coalescence process. Therefore, because the cloud water content is now different, the difference in rate between the two scenarios will be less at the next time step than it was at the first time step.

The trends in convective mass flux (Fig. 3.1d), defined as the mass flux at points with vertical velocity greater than 1 m s^{-1}, are in keeping with those for the condensation rate. Simulation D5 has a convective mass flux more similar to the constant number concentration cases, in part because so much of its cloud water is lofted above the freezing level where it causes increases in ice production and latent heating in the mixed-phase region (not shown). Simulation D25 has ~1/2 as much convective mass flux as the other three simulations during the first 40 minutes. The mass flux, and presumably the updraft speed, is reduced in D25 due to the relatively low condensational latent heating (Fig 3.1a) and therefore reduced buoyancy. These changes in convective mass flux alter the morphology of the cloud and have implications for the subsequent development of the simulated storm.

After the initial 30-40 minutes, the microphysical feedbacks to the dynamics begin to dominate the differences between the simulations. It is emphasized that the purpose of this study

is not to determine the pathways for these feedbacks, but rather only to demonstrate that they exist and that they lead to uncertainties in the simulation results. The D25 case, though it had the least convective mass flux initially, sustains the mass flux during the middle period of the simulation and ultimately produces the most mass flux at the end of the simulation when secondary convection begins to develop. This fundamental change in the evolution of convection is reflected in the precipitation, cloud mixing ratio, and cloud process fields (Fig. 3.1a-c). The other three simulations appear to plateau to some degree in these fields whereas D25 continues to increase steadily. Ultimately D25 produces greater than or in excess of 3 times more precipitation than its D5 counterpart. This is a significant increase considering that the only difference in the setup of the two simulations is the mean size of the cloud droplets.

The sensitivity of these simulations to rain drop size is also briefly explored. The initial four simulations all had a fixed mean rain drop size of 1mm. Based on a double-moment simulation of this same storm (not shown), 1 mm is a representative mean diameter for raindrops near the surface, but it is large for raindrops in rain formation regions. A fifth simulation (D25_RD0.3) again uses a fixed cloud droplet size of 25μm, but reduces the mean raindrop diameter to 0.3 mm. In terms of cloud process rates, cloud water path, and convective mass flux, D25 and D25_RD0.3 are more similar to each other than to any other simulation (Fig. 3.1a, b, and d). Nonetheless, convective mass flux during the second half of the two simulations becomes increasingly different, and the final precipitation produced in D25_RD0.3 is significantly reduced (Fig. 3.1c), in part due to greater rain evaporation caused by small raindrops that evaporate more readily (not shown).

c. Other Thermodynamic and Radiative Impacts

The atmosphere is a complex system and, not surprisingly, these changes in cloud properties and dynamics impact many other aspects of this system. Changes to the precipitation amount and evaporation rates below cloud base lead to an average reduction in surface temperature of ~0.5K between the warmest (D5) and coolest (D25_RD0.3) simulations within the cold pool, where the cold pool is defined as all surface points with temperature less than the base state surface temperature. In terms of forecasting daily temperature this may not be important, but it could be very important for cold pool dynamics and subsequent convective development (Tompkins 2001). A number of other studies have also shown sensitivity of the cold pool strength to choices in microphysical parameters (e.g. van den Heever and Cotton 2004; Dawson et al. 2010; Adams-Selin et al. 2013).

Upper level tropospheric moisture is important as a chemical catalyst in the stratosphere and in its own right as a greenhouse gas. Figure 3.2b shows that up to 75% more moisture is available in the lower stratosphere in the D5 case, likely because more cloud water was available to be transported to the upper atmosphere to form ice in the anvil that subsequently sublimated. Accurately predicting stratospheric moisture has been shown to be critical to predicting long-term temperature trends of the lower stratosphere (Thompson et al. 2012).

Radiation is another factor that is impacted by changes to the single-moment scheme design. Differences in radiation will be largely driven by changes in cloud area, though total water content, hydrometeor phase, and other hydrometeor properties will also play a role. Cloud area, reflected shortwave fraction, and outgoing longwave radiation are shown in Figure 3.2c-e. A column is defined to be cloudy if one or more grid boxes has a hydrometeor mixing ratio greater than 0.01 g kg^{-1}. The radiative quantities have been averaged over cloudy columns; therefore differences in these quantities between simulations do not account for changes in cloud

area. The reflected shortwave radiation is consistently ~25% higher in D5 compared to D25 and N100 throughout the latter half of the simulations (Fig. 3.2c) due to smaller cloud and ice particles. In terms of outgoing longwave radiation, the anvil in D25_RD0.3 emits ~45% more longwave radiation than D5 (Fig. 3.2d), which is in part due to D25_RD0.3 having a lower cloud top height (not shown). These changes in radiation have implications for the radiative balance of the earth as simulated by CRMs (particularly when they are used for radiative-convective equilibrium simulations) and by GCMs and present yet another reason why moving away from single-moment schemes to double-moment schemes should be considered. To put one of these values in context, the 45% increase in emitted longwave radiation in D25_RD0.3 compared to D5 would be on par with the magnitude of the largest deep convective cloud-climate feedback predicted by climate models (Zelinka and Hartmann 2010).

3.4 Single- vs. Double-Moment Schemes

a. Simulation Design

It could be argued that perhaps the simulations discussed in the previous section would not show such large differences if they were run for a longer period or over a larger domain. Furthermore, perhaps a similar range in sensitivity could be obtained by varying the aerosol concentration (which is arguably the primary control on the cloud droplet number concentration) in a double-moment simulation. To test some of these possibilities, results from large-domain and long-time radiative-convective equilibrium (RCE) RAMS simulations are now presented.

These simulations were conducted at cloud-resolving grid scale (1km) on a large domain (3000x200) with doubly periodic lateral boundary conditions and 65 vertical levels. The model top extends to 25km altitude. This narrow grid setup has proven useful in the past to allow for

large-scale flows while minimizing computational cost (Tompkins 2001; Posselt et al. 2008). The simulation is run for 70 days. The final 10 days will be used for analysis. As in (van den Heever et al. 2011), the 0000 UTC 5 December 1992 tropical sounding from TOGA-COARE (Tropical Ocean Global Atmosphere Coupled Ocean-Atmosphere Response Experiment) was used to initialize the temperature and moisture fields. Convection was induced with small, random perturbations to the potential temperature field. No mean wind was imposed, but a minimum wind speed of 4m/s was used for the bulk surface flux calculations. A Smagorinsky (1963)-type turbulence scheme and the 2-stream radiation scheme that is fully interactive with hydrometeors (Harrington 1997) were used. These simulations are designed to represent the equilibrium state of the tropical atmosphere and contain the full range of tropical cloud types, from shallow, isolated cumulus through to large, deep convective complexes (van den Heever et al. 2011).

The base simulation is run with the double-moment scheme for 70 days; it is in RCE for approximately the latter half of that time. The base simulation is run with the double-moment microphysics scheme and has a horizontally and vertically homogeneous aerosol concentration of 100 cm^{-3}. This base simulation will be referred to as DM_A100.

DM_A100 is restarted on day 60 and run for ten days with the single-moment microphysics scheme (SM_DEF) rather than the double-moment scheme. The initial mixing ratio of all species is kept the same, but the number concentration and mean diameter all change instantaneously upon restart. This method of restarting DM_A100 rather than starting a new simulation with the single-moment scheme and running it for 70 days is justified in section 3.6. SM_DEF is run with a fixed cloud droplet number concentration of 300 mg^{-1}. This droplet number concentration is the default value in RAMS; all other parameters are also run with the

default values (see Table 3.2). While the default values may not be the most appropriate values to use, the default values may be a common and typical choice made by users of cloud models, especially those who are not experts in microphysics, regardless of the kind of simulation they are running. Therefore, we want to explore the consequences of this potentially naïve choice in these RCE simulations.

A second sensitivity test has also been run in which an exponentially decreasing aerosol concentration profile is utilized (DM_A1000). The profile maximizes at 1000 cm^{-3} at the surface and has a scale height of 2 km. The double-moment scheme is used for this test. It is presented to show a possible range of cloud characteristics for a change in aerosol concentration. Given that the increase in aerosol concentration in DM_A1000 is relatively large, especially for the tropical maritime environment, we would hope that the differences in cloud properties arising through use of the single-moment scheme would be no larger than those arising from this significant (and physically possible) increase in aerosol concentration.

b. Bulk Cloud and Rain Properties

Average cloud fraction as a function of height from the three simulations is shown in Figure 3.3 where the shading indicates one standard deviation in the time mean. At heights greater than 11 km, where anvil clouds associated with deep convection are present, the cloud fraction of the single-moment simulation is comparable to or exceeds those of the two double-moment simulations. Below 11 km, differences in the cloud fraction are larger. Peaks in cloud fraction at 5.5km and 9km associated with congestus and detrainment at the freezing level (Johnson et al. 1999; Posselt et al. 2008) are reduced or not present in SM_DEF. There is a peak around 2km in all three simulations that indicates the shallow convective mode; however in the

single-moment simulation this peak is drastically reduced. It is ~1/6 the magnitude of the corresponding peak in cloud fraction for DM_A100, and the shaded regions do not overlap. The tropical shallow cloud fraction as measured from CloudSat (Mace et al. 2009) and CALIPSO (Medeiros et al. 2010) is ~0.15-0.25, which indicates that the double-moment simulations capture the frequency of these clouds more realistically. Additionally, although all of the RCE simulations underestimate the upper-level cloud fraction (~12%; Mace et al. 2009), only the double-moment simulations correctly simulate more low cloud fraction than high cloud fraction.

Figure 3.4a shows the average rain rate as a function of precipitable water. The "critical" precipitable water (PW) value at which rain rates increase rapidly can be used to indicate the transition from shallow to deep convection and is a strong function of mean tropospheric temperature (Neelin et al. 2009). All of the RCE simulations have a mean tropospheric temperature of 273 K, which, based on observations, corresponds to a critical PW value of 68 mm (Neelin et al. 2009). For the two double-moment simulations, this value is ~65 mm, whereas for the single-moment simulation, it is ~60 mm. Again, the double-moment simulations agree more closely with the observations. The difference in these values can be put in context by noting that observations indicate that a decrease of 5mm in this critical PW value occurs for a 2 °C decrease in tropospheric mean temperature (Neelin et al. 2009), a large value in the context of climate considerations. The mean temperature profiles among all the simulations, though, are very similar. This comparison suggests that the shift in the critical PW between the single- and double-moment simulations is large and could have important implications for the proper simulation of the tropical atmosphere.

Figure 3.4b shows the ratio of the mean rain rate as a function of (PW) for SM_DEF and DM_A1000 to that of DM_A100. Associated with the reduction in cloud fraction for shallow

convection in SM_DEF is a 70-90% reduction in the average rain rate for values of PW less than ~40mm. This reduction in rain rate is consistently 10-40% greater than that seen in DM_A1000. Though much smaller, there is also a greater change in the convective rain rates (PW values greater than ~60-65 mm) in SM_DEF than in DM_A1000. These changes to the cloud fraction and rain rate of both deep and shallow convection are noteworthy since they are entirely driven by the differences in the microphysics scheme, and because they are larger than changes that can be achieved by a tenfold increase in aerosol concentration in the double-moment scheme.

To investigate the cause of the reduced cloud fraction in SM_DEF, time series of rain and cloud water path in regions of shallow convection, defined as all points with PW less than 40mm, are shown in Fig. 3.5. The rain and cloud water paths in SM_DEF both decrease immediately and never recover. The decrease is even larger than that for DM_A1000, the simulation that was expected to be an approximate limit for the magnitude of cloud property changes. Figure 3.5 suggests that the large changes in cloud fraction (Fig. 3.3) and rain rate (Fig. 3.4) in SM_DEF are due to fast changes in the microphysics, and are not due to a slow adjustment to a new radiative-convective equilibrium state.

The average cloud droplet number concentration in shallow clouds in DM_A100 is ~30 cm^{-3} (Fig. 3.6a), which is much lower than the fixed cloud droplet concentration of 300 cm^{-3} in SM_DEF. Given that both simulations begin with the same cloud water content, cloud droplets in SM_DEF are immediately made to be ~1/5 the size of those in DM_A100. Conversely, the average raindrop diameter is 0.2-0.5mm for shallow cumuli (Fig. 3.6b), which is much lower than the fixed raindrop diameter of 1mm. These comparisons indicate that cloud droplets are much smaller in SM_DEF and lead to reduced collision-coalescence and rain production. With less rain, and with much larger raindrops that evaporate more slowly, evaporatively-generated

cold pools likely diminish in strength and number, thus making new convection more difficult to initiate in SM_DEF.

c. Representative Parameters

These results suggest that more care should be taken in choosing the fixed parameters in a single-moment scheme. Perhaps the cloud characteristics in SM_DEF and DM_A100 would be more similar if the fixed parameter values in SM_DEF were more representative of the values in DM_A100. To test this idea, a second single-moment sensitivity simulation was started in the same way as SM_DEF, but in which the fixed parameter values were taken as the mass-weighted averages of number concentration or diameter of each hydrometeor species from DM_A100 at the time of the model restart. These values are listed in Table 3.2 and the simulation is referred to as SM_AVG. Table 3.2 shows that some of the parameter values in SM_DEF, such as aggregate diameter, are in fact quite close to the averages in DM_A100 which are used for SM_AVG. However, parameters such as the cloud droplet number concentration and raindrop diameter used in SM_DEF are not appropriate for representing these microphysical characteristics in DM_A100.

SM_AVG developed a low-level downdraft associated with one of the deep convective storms with a speed of -18 m s^{-1} after just over six hours of simulation that was incompatible with the vertical grid spacing. Nonetheless, since the largest changes in SM_DEF occurred in the first six hours, we can learn from this simulation. The rain water content in this downdraft was high compared to values found at any time in DM_A100 (not shown). This suggests that rain water is being created too quickly in regions of deep convection. While the cloud droplet number concentration is 40 cm^{-3} in SM_AVG, the average cloud droplet number concentration

in deep convective updrafts in DM_A100 is ~75-100 cm^{-3} (Fig. 3.6a). Assuming that the cloud water contents are similar, this difference in number concentration implies that the cloud droplets in SM_AVG are too large compared to DM_A100 in these updrafts and may be causing too efficient conversion of cloud water to rain. Furthermore, average raindrop sizes increase rapidly in the low-level downdrafts (Fig. 3.6b) as the smallest drops are evaporated in DM_A100, though this change in size is counteracted somewhat by the rain break-up process which begins when drops reach 0.6 mm in diameter. These effects are not captured in single-moment simulations. Therefore the average raindrop size at low levels (where the large downdraft occurred) in SM_AVG is too small, thus enhancing evaporation and downdraft generation relative to DM_A100.

Even in the regions of shallow cumulus, SM_AVG does not appear to have improved the representation of clouds. The cloud water path decreases at about the same rate as in SM_DEF (Fig. 3.5a). Rain water in SM_AVG does not decrease as quickly (Fig. 3.5b). However, as in the regions of deep convection, the average raindrop size is too small at low levels compared to DM_A100 (Fig. 3.6b) and therefore the rain evaporation process would likely not be well represented. These results suggest that the natural variability in microphysical properties of hydrometeors within all tropical cloud types can be better simulated by double-moment schemes than single-moment schemes.

3.5 Conclusions

Single-moment microphysics schemes run faster but by design predict fewer properties of hydrometeor distributions than double-moment microphysics schemes. It has been shown here through theoretical arguments and simple numerical experiments that the assumptions made in

single-moment schemes lead to a large degree of inherent uncertainty in simulations of convective clouds. For example, in a single-moment scheme with a fixed mean cloud droplet diameter, basic microphysical equations indicate that doubling of the diameter can decrease condensation rates by a factor of four while increasing autoconversion rates by a factor of two. Simulations of a deep convective cell using the RAMS single-moment scheme confirm that the microphysical rates are highly sensitive to the choice of parameter to fix and its value. Unlike most other single-moment schemes, RAMS allows the diameter of hydrometeors to be fixed rather than the number concentration or the intercept parameter. The results show that the simulations are indeed more sensitive to a change in the fixed mean diameter than to the fixed number concentration as predicted by the simple theoretical arguments. This finding may lend support to the choice of a fixed number concentration rather than a fixed mean diameter in single-moment schemes.

The changes in the microphysical rates seen in the idealized thunderstorm simulations feed back to other fields in the simulations. Accumulated precipitation showed up to a 200% percent increase as a result of observationally-based parameter choices in the single-moment scheme. Convective mass flux, surface temperature, short and longwave radiation, and upper level moisture are all also sensitive to the fixed parameters of a single-moment scheme. The variability in the radiative fluxes is found to be of similar magnitude to those associated with cloud feedbacks predicted by climate models (Zelinka and Hartmann 2010).

In addition to simulations employing single-moment schemes being sensitive to the choice of parameters and values, they struggle to capture the observed bulk features of tropical clouds such as cloud fraction and rain rate in radiative-convective equilibrium simulations, whereas double-moment schemes, at least the double-moment scheme in RAMS, are more

successful with these tasks. Even when every effort is made to choose fixed values in a single-moment scheme that are representative of the system being simulated, our results show that unintended feedbacks can arise due to the inherently large variability of hydrometeor distribution properties within cloud systems. Similar conclusions have been drawn in studies of squall line convection which have found that single-moment schemes cannot simultaneously capture the microphysical properties of the leading line and the trailing stratiform cloud (Morrison et al. 2009; Van Weverberg et al. 2012; Baba and Takahashi 2013). Lastly, although our RCE simulations are idealized, the results suggest that double-moment schemes better represent tropical clouds than single-moment schemes when compared with observations.

The focus in this study has primarily been on the warm phase. To confirm further that double-moment schemes outperform single-moment schemes, more detailed analysis of the ice phase should be done in a future study. In addition, though not explored in this study, it is recognized that single-moment schemes with parameters diagnosed from environmental conditions may mitigate some of the issues with more traditional single-moment schemes (Roh and Satoh 2014), such as the one used in this study. Lastly, as discussed in the introduction, while double-moment schemes eliminate some of the assumptions required in single-moment schemes, they do introduce new assumptions that in some cases do not result in any improvement to simulations (e.g. Van Weverberg et al. 2014). Nonetheless, it seems that double-moment schemes should be able to represent simultaneously better the characteristics of *multiple cloud types* in a single simulation even if a single-moment scheme can predict the characteristics of any *one cloud type* as well or better.

It is acknowledged that the use of single-moment schemes may sometimes be desirable in order to understand specific feedback processes, to constrain intentionally the model for various

experiments, in simple model frameworks where the equations are oversimplified intentionally for specific purposes, or in very long time simulations such as those used for climate predictions. However, if one of those situations is not the case, it is argued based on our results and those of others (Reisner et al. 1998; Swann 1998; Luo et al. 2008; Morrison et al. 2009; Dawson et al. 2010; Milbrandt et al. 2010; Lee and Donner 2011; Jung et al. 2012; Molthan and Colle 2012; Van Weverberg et al. 2012; Baba and Takahashi 2013; Jin et al. 2014) that the improvement in the representation of clouds and cloud feedbacks gained by use of a double-moment scheme (or other added complexity schemes such as triple-moment or spectral bin schemes) is well worth the extra expense in computational time and should be strongly considered in all but the lengthiest simulations where realistic reproduction of the atmosphere is desired.

3.6 Appendix A

It could be argued that the method of restarting a simulation with a different microphysics scheme as was done here is too strong a "shock" to the model and that differences between the original and restarted simulations are a result of this shock. To test if this is the case, SM_DEF is restarted from its fifth simulation hour with the double-moment scheme turned back on (DM_restart) and run for five days. Such a restart does not produce a shock to the model because the initial hydrometeor mixing ratios and number concentrations are identical to those in SM_DEF. If the shock is the primary cause of the rapid changes, then DM_restart, which has no shock, should continue to behave like SM_DEF. If the shock is *not* the primary cause of the rapid changes in cloud properties, then DM_restart should also rapidly return to a state similar to DM_A100.

Rapid changes to the cloud and rain properties are in fact seen in DM_restart. The cloud fraction and rain rate values become similar to those seen in Figs. 3.3 and 3.4 within two days (Fig. 3.7) with the most rapid increases occurring within the first ten hours of the simulation. (Over the next three days, the low cloud fraction increases beyond the average seen in Fig. 3.7a and then decreases again (not shown). While the average over this three-day period is higher than that seen in Fig. 3.7a, it is believed that the simulation would eventually return to the average value. Such large fluctuations are not seen in SM_DEF and thus are not of concern for the validity of the results arising from that simulation.) This result strongly suggests these RCE simulations respond very quickly to changes to the microphysics scheme. Furthermore, the cloud fraction in SM_DEF is very similar to the cloud fraction presented by Posselt et al. (2008) as part of a similar RCE modeling study utilizing a single-moment scheme (their Fig. 3.2b). While the responses seen in SM_DEF within the first hour are likely a result of the model shock, it is unlikely that the long-term responses are also a result of the model shock. Rather they are physical changes that could be expected to persist if the model were run for additional days or if the simulation had been started at time zero.

3.7 Tables and Figures

Table 3.1. Summary of the sensitivity of process rates to a fixed mean diameter and fixed number concentration of cloud droplets as described in Section 3.2.

Change in the process rate when …	Condensation/ Evaporation	Collision-Coalescence
Diameter is doubled	÷ 4	x 2
Number concentration is doubled	x 1.6	÷ 1.3
Number concentration is increased tenfold	x 4.6	÷ 2.2

Table 3.2. Summary of the microphysical parameters used in the idealized thunderstorm and RCE simulations. The parameter that is fixed is indicated with a 'D' for mean diameter, 'N' for number concentration, or 'P' if it is predicted (that is, the double-moment scheme is being used). The unit for the cloud diameter is micrometers; all other diameters are given in millimeters. The number concentration is given in # mg^{-1} and is italicized as a reminder that it is not a diameter. Note that the aerosol number concentration is a prognostic variable and that the value given is the initial concentration at the surface. Values that are not the default values are in bold font. Values for SM_AVG are the mass weighted average values for the restart time in DM_A100. See the text for further details.

	Cloud	$N_{drizzle}$	D_{rain}	D_{snow}	D_{aggr}	$D_{graupel}$	D_{hail}	$N_{aerosol}$
Idealized Thunderstorm Simulations								
D5	**D - 5**	*0.1*	1	1	1	1	3	N/A
D25	**D - 25**	*0.1*	1	1	1	1	3	N/A
N100	***N - 100***	*0.1*	1	1	1	1	3	N/A
N1000	***N - 1000***	*0.1*	1	1	1	1	3	N/A
D25_RD0.3	**D - 25**	*0.1*	**0.3**	1	1	1	3	N/A
RCE Simulations								
SM_DEF	*N - 300*	*0.1*	1	1	1	1	3	N/A
SM_AVG	***N - 40***	***0.2***	**0.2**	**0.3**	**0.9**	**0.7**	**1**	N/A
DM_A100	P	P	P	P	P	P	P	*100*
DM_A1000	P	P	P	P	P	P	P	*1000*

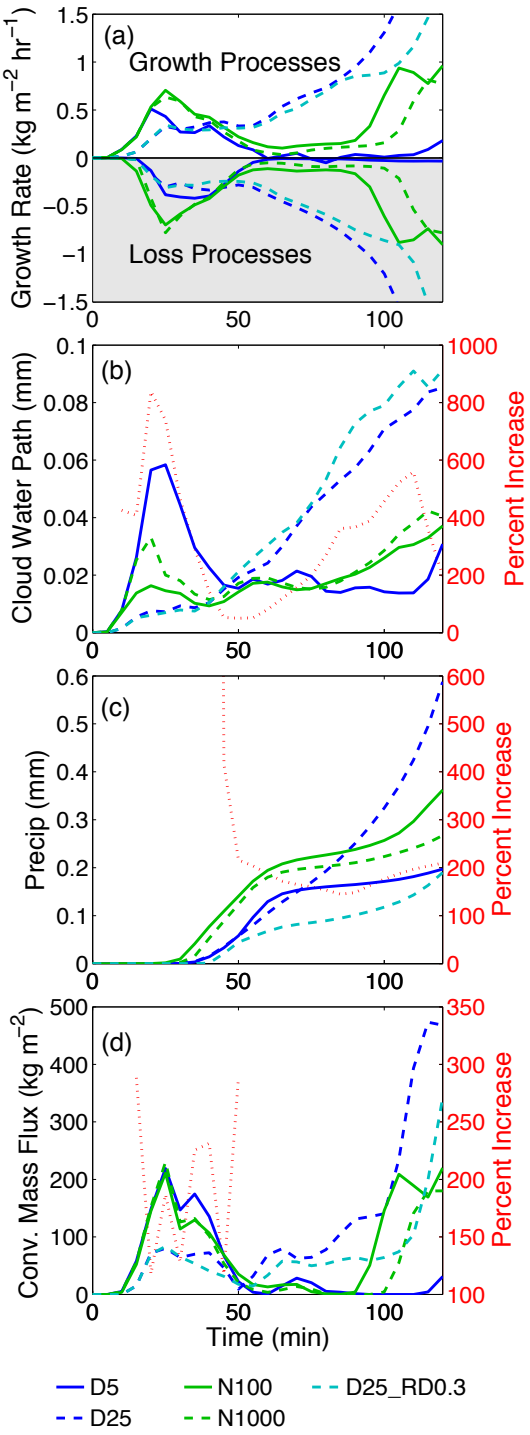

Figure 3.1. Time series of domain-mean quantities. (a) Vertically-integrated net condensation rate and loss rate of cloud water through autoconversion, accretion, and riming, (b) cloud water path, (c) accumulated precipitation and (d) vertically integrated convective mass flux (see text for details). The red dotted lines in (b)-(d) correspond to the right axes and show the percent increase of the maximum value among all five simulations relative to the minimum value among all five simulations as a function of time.

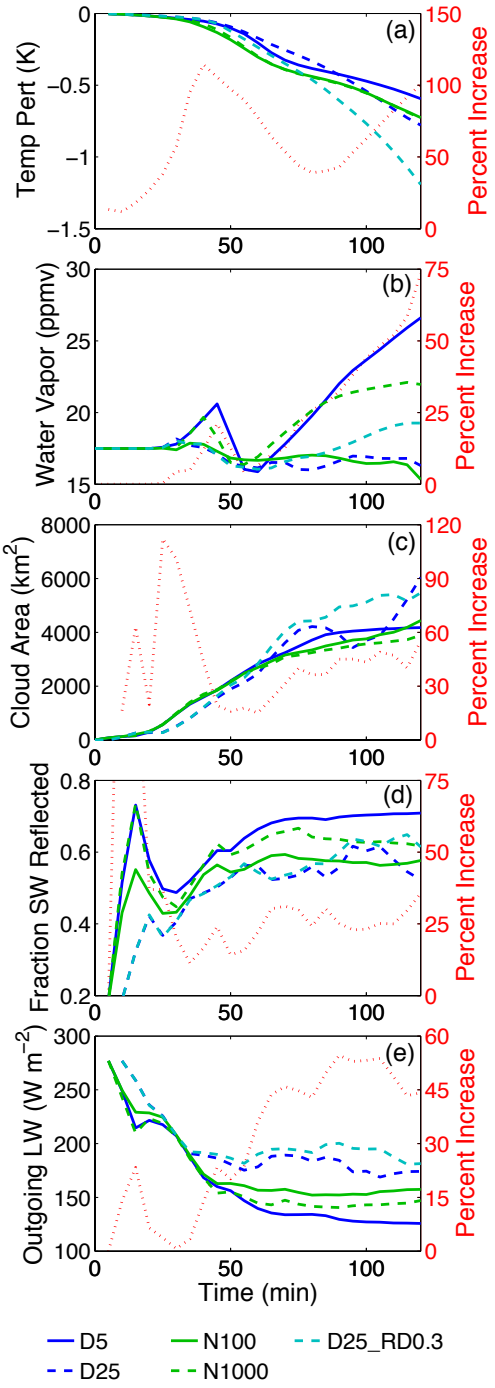

Figure 3.2. Time series of (a) Average cold pool surface temperature perturbation relative to the initial environmental temperature, (b) water vapor mixing ratio averaged over a 10000 km^2 area centered around the storm at the first model level above the tropopause (13.3 km), (c) cloud area, (d) fraction of incoming shortwave radiation reflected in cloudy columns, and (e) top of atmosphere outgoing longwave radiation in cloudy columns. A cloudy column in (c-e) is defined as a column with condensate mixing ratio at any level greater than 0.01 g kg^{-1}. Red dotted lines are as in Fig. 3.1.

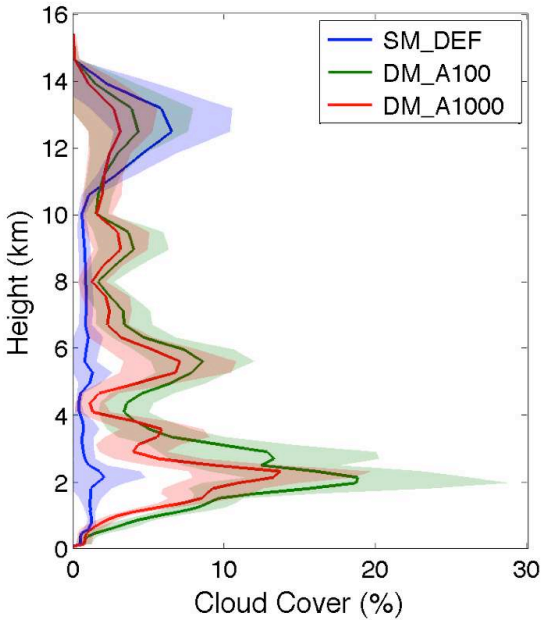

Figure 3.3. Average cloud cover as a function of height in each of the three simulations. The shaded regions indicate one standard deviation in the time mean.

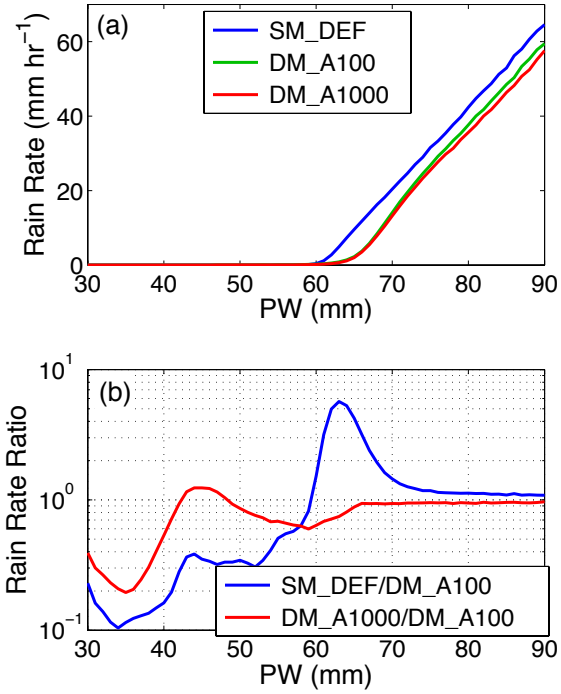

Figure 3.4. (a) Average rain rate as a function of 1mm precipitable water bins. (b) The ratio of the rain rates shown in (a) for selected pairs of the simulations.

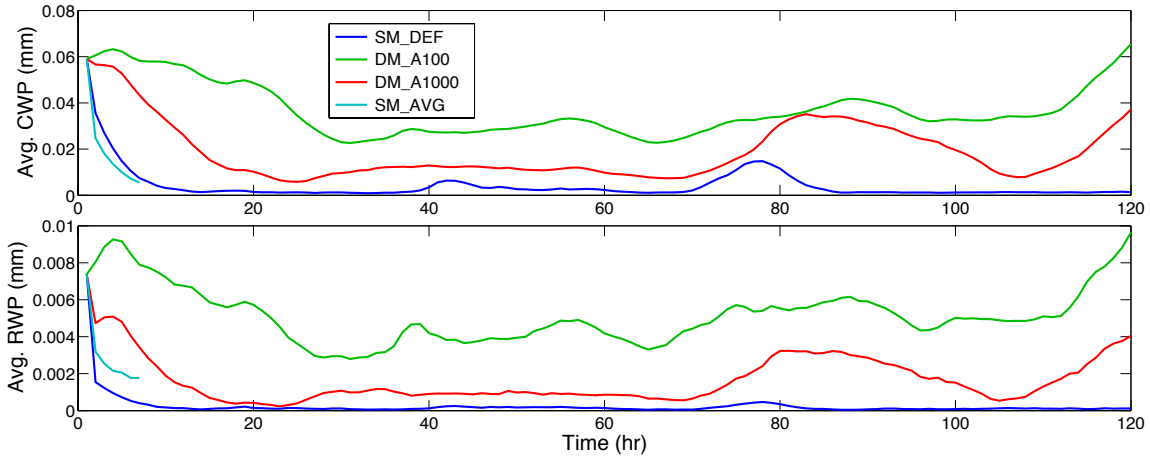

Figure 3.5. Time evolution over the first 120 hours of simulation of the average cloud and rainwater path (CWP, RWP) in low PW regions (<40 mm).

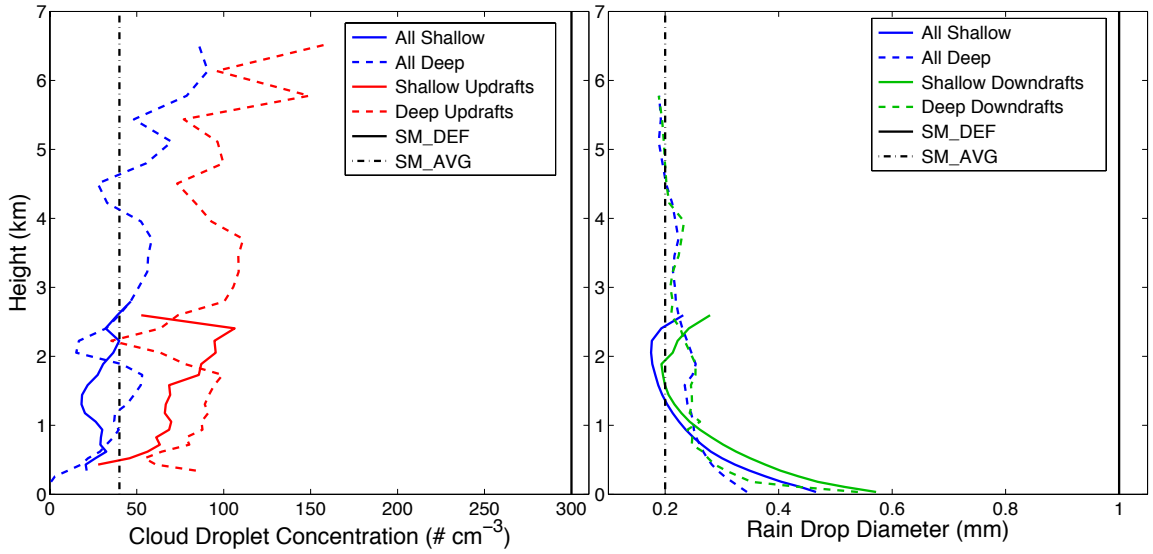

Figure 3.6. Colored lines: (a) cloud droplet concentration averaged over cloudy points and (b) mass-weighted raindrop diameter averaged over rainy points in DM_A100. Cloudy and rainy points defined as having a mixing ratio > 0.01 g kg^{-1}. Shallow cumulus identified as regions with precipitable water < 40mm, deep convection identified as regions with precipitable water > 60mm. Updrafts (downdrafts) defined to be points with vertical velocity > 0.5 m s^{-1} (< −0.5 m s^{-1}). Black lines: Fixed values of each parameter in the two single-moment simulations.

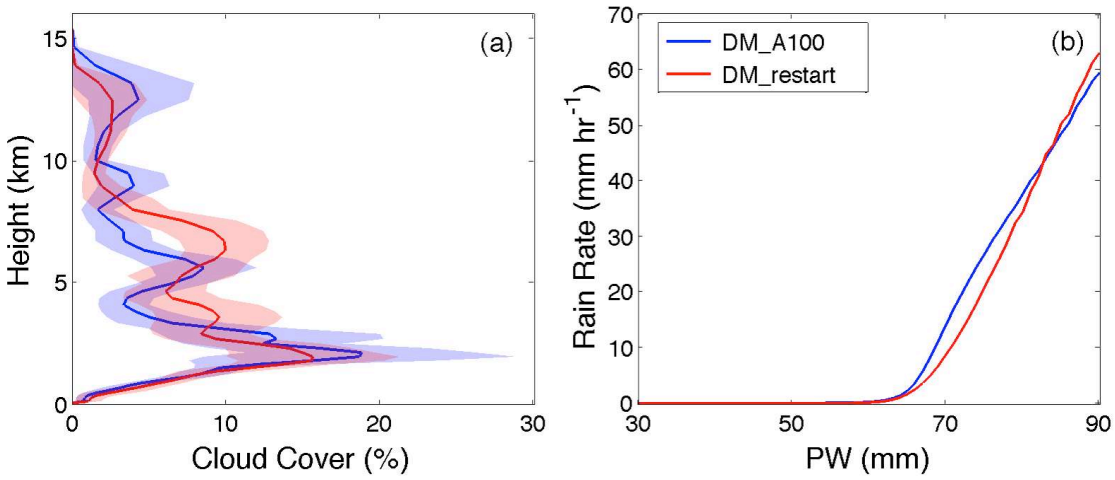

Figure 3.7. (a) As in Fig. 3.3, and (b) as in Fig. 3.4, for DM_A100 and DM_restart. The values for DM_restart are averaged over the first 48 hours of the simulation.

4. CONDENSATION RATES IN BIN AND BULK MICROPHYSICS SCHEMES

4.1 Introduction

Bin and double-moment bulk microphysics schemes are both popular approaches for parameterizing subgrid-scale cloud processes (Khain et al. 2015). In double-moment bulk schemes, the mixing ratio and total number concentration for predefined hydrometeor species are typically predicted, and a function is assumed to describe the shape of the size distribution of each species. In contrast, bin schemes do not assume a size distribution function, but instead, the distribution is broken into discrete size bins, and the mixing ratio is predicted for each bin. Usually the size of each bin is fixed, in which case the number concentration is also known for each bin.

Bin schemes are generally thought to describe cloud processes more realistically and accurately than bulk schemes, and thus they are often used as the benchmark simulation when comparing simulations with different microphysics schemes (e.g. Beheng 1994; Seifert and Beheng 2001; Morrison and Grabowski 2007; Milbrandt and Yau 2005; Milbrandt and McTaggart-Cowan 2010; Kumjian et al. 2012). However, they are much more computationally expensive since many additional variables need to be predicted and as a result bin schemes are used less frequently. It is of interest then to see how well bulk and the more accurate bin microphysics schemes compare in terms of predicted process rates, and to assess how much value is added by using a bin instead of a bulk microphysics scheme.

One of the primary drawbacks of double-moment bulk schemes that assume probability distributions is that many microphysical processes are dependent on the distribution parameters that must be either fixed or diagnosed. In the case of a gamma distribution, this parameter is

typically the shape parameter. Much is still to be learned regarding what the most appropriate value of this parameter is, and how it might depend on cloud microphysical properties. Figure 4.1 shows previously proposed relationships between the cloud droplet number concentration and the shape parameter (Grabowski 1998; Rotstayn and Liu 2003; Morrison and Grabowski 2007; hereafter G98, RL03, and MG07, respectively) along with values of the shape parameter reported in the literature and summarized by Miles et al. (2000). The figure shows a wide range of possible values of the shape parameter based on observations. The lowest reported value is 0.7 and the highest is 44.6, though this highest point is clearly an outlier. Furthermore, there is no apparent relationship with the cloud droplet concentration in the data set as a whole, and both increases and decreases of the shape parameter are found with increasing droplet concentration among individual groupings. Figure 4.1 also shows that two of the proposed functions relating these two quantities are similar (RL03 and MG07), but that the third function is in total disagreement with these first two (G98).

Furthermore, using appropriate values of the shape parameter may be necessary for accurately modeling cloud characteristics and responses to increased aerosol concentrations. Morrison and Grabowski (2007) found that switching from the MG07 to the G98 N-v relationships in Fig. 4.1 led to a 25% increase in cloud water path in polluted stratocumulus clouds. This example shows that inappropriately specifying the shape parameter could have implications for the accurate simulation of not only basic cloud and radiation properties but also for the proper understanding of cloud-aerosol interactions. However, it is apparent from Figure 4.1 that *large uncertainties still exist regarding the behavior of the shape parameter and how it should be represented in models*.

The goal of this study is to compare the condensation and evaporation rates predicted by bin and bulk microphysics schemes in cloud-resolving simulations run using the same dynamical and modeling framework and to assess what the biggest sources of disagreement are. The focus is on condensation and evaporation since these processes occur in all clouds and are fundamental for all hydrometeor species. It will be shown that in spite of other basic differences between the particular bulk and bin microphysics schemes examined here, the lack of a prognosed shape parameter for the cloud droplet size distribution in the bulk scheme is often the primary source of differences between the two schemes, and thus an improved understanding of the shape parameter is necessary from observations and models.

4.2 Condensation/Evaporation Rate Formulations

The Regional Atmospheric Modeling System (RAMS) is used in this study. It contains a double-moment bulk microphysics scheme (RDB; Saleeby et al. 2004), and the Hebrew University spectral bin model (SBM; Khain et al. 2004). The SBM is newly implemented in RAMS. Details about the implementation can be found in the supplementary information.

In the RDB microphysics scheme, condensation/evaporation is treated with a bulk approach. Cloud droplet size distributions are assumed to conform to a gamma probability distribution given by:

$$n(D) = \frac{N}{{D_n}^{\nu}\Gamma(\nu)} D^{\nu-1} e^{-D/D_n} \tag{4.1}$$

All symbols are defined in Table 4.1. The condensation/evaporation scheme is described in detail in Walko et al. (2000), and the amount of liquid water condensed in a time step is given by their Eq. 6. Here, a slightly rearranged and simplified version of this equation is presented in order to highlight the similarities to the SBM condensation/evaporation equation shown below.

Specifically, the RDB condensation/evaporation equation is written as:

$$r_c^{t+\Delta t} = r_c^* + 2\pi \left[N\bar{D}v \left(\frac{\Gamma(\nu)}{\Gamma(\nu+3)} \right)^{1/3} f_{v,RBE} \right] G_{RBE}(T, r_{vs}, r_c^*) \left(S^{t+\Delta t} - 1 \right) \Delta t \tag{4.2}$$

By using the value of S at $t+\Delta t$, the full equation for r_v (not shown) is implicit.

In contrast, the equation for the condensation/evaporation rate in the SBM is given by:

$$r_c^{t+\Delta t} = r_c^* + 2\pi \left(\sum N_i D_i f_{vi,SBM} \right) G_{SBM}(T, e_s) \int_0^{\Delta t} \left(S - 1 \right) dt \tag{4.3}$$

Semi-analytical equations are used to solve for the time integral of supersaturation that appears at the end of Eq. 4.3 (Khain and Sednev 1996).

Although both equations have the same basic form, there are three primary differences in how these equations are formulated:

- In the SBM, as is required by the model structure, the condensation rate is calculated for each bin of the distribution, and these rates are then summed over all bins, as opposed to the integration of the gamma distribution that is done in the RDB scheme.
- The formulation of the ventilation coefficients and of G_{RDB} and G_{SBM} are different, though the details will not be discussed here.
- The time step integration is performed semi-analytically in the SBM with multiple sub-time steps rather than implicitly in the RDB scheme.

These differences between the bin and bulk schemes will be taken into consideration in this analysis in order to understand why the two schemes produce different condensation rates.

4.3 Simulations

In order to investigate the difference in condensation rates predicted by the two microphysics schemes, simulations of *non-precipitating* shallow cumulus clouds over land were performed. This cloud type was chosen in order to minimize the indirect impacts of precipitation processes and thus facilitated the direct comparison of condensation rates. Furthermore, the daytime heating and evolution of the boundary layer results in a wider range of thermodynamic conditions than would occur in simulations of maritime clouds. The wider range of thermodynamic conditions make the conclusions of this study more robust. The simulations were run with RAMS and employed 50m horizontal spacing and 25m vertical spacing over a grid that is 12.8 x 12.8 x 3.5 km in size. More details about the simulation set-up can be found in the supplemental information. Three simulations were run with the RDB scheme and three with the SBM scheme. Since the relationships in Figure 4.1 (G98; RL03; MG07) suggest that the shape parameter may depend on the cloud droplet number concentration, the simulations were run with three different aerosol concentrations, specifically, 100, 400, and 1600 cm^{-3}, in order to obtain a larger range of droplet concentration values. The number concentration of 100 cm^{-3} is somewhat uncommon over land, but it is necessary to use this value in order to more fully explore the range of possible microphysical conditions. The simulations will be referred to by the microphysics scheme abbreviation and the initial aerosol concentration, e.g. SBM100 and RDB1600.

4.4 Results

a. Binned Instantaneous Rates

In order to directly compare the condensation rates predicted by the RDB and SBM microphysics schemes, it is necessary to evaluate these rates given the same thermodynamic and

cloud microphysical conditions. The RDB condensation equation (Eq. 4.2) is approximately proportional to four quantities: S, N, $\bar{D}$, and v. We say approximately proportional since the presence of the ventilation coefficient and the time-stepping methods make these factors not truly proportional to the condensation rate. In the SBM scheme, the condensation rate is only explicitly proportional to S, and the SBM scheme does not make assumptions about the functional form of the size distribution. If it is assumed nevertheless that the SBM size distributions can be described by some probability distribution function (which doesn't necessarily have to be a gamma distribution), then Eq. 4.3 could also be rewritten to be approximately proportional to N and $\bar{D}$. Therefore, in order to best compare the condensation rates between the two schemes, the condensation and evaporation rates that occur during one time step were binned by the values of S and $N\bar{D}$ (hereafter referred to as the integrated diameter) that existed at the start of the condensation/evaporation process and were averaged in each bin. Where the cloud was supersaturated and subsaturated, saturation ratio bin widths of 0.1 and 1 were used, respectively. For $N\bar{D}$, bin widths of 0.05 m g^{-1} were used. The output from the model only includes the values of S, N, and $\bar{D}$ after condensation and evaporation have occurred. However, since the rates of condensation and droplet nucleation were known, and since microphysics is the last physical process to occur during a time step in RAMS, the S, N and $\bar{D}$ that existed before condensation occurred were easily obtained. All points where the cloud mixing ratio before condensation was greater than 0.01 g kg^{-1} are included in the analysis.

The average condensation rate in each S and $N\bar{D}$ bin was calculated for all simulations. Figure 4.2 shows an example of this calculation for one simulation. As is seen in Figure 4.2, there is a smooth transition to higher condensation rates as the saturation ratio increaeses, and to higher condensation ($S \geq 1$) and evaporation ($S < 1$) rates as the integrated diameter increases. This

is expected based on the condensation equations (Eqs. 4.2, 4.3). All other simulations behave similarly.

In order to easily compare the condensation rates predicted by the two microphysics schemes, Figure 4.3a-c shows the ratio of the RDB to SBM condensation rates in the S and $N\bar{D}$ phase space. It reveals that for low integrated diameter values, the RDB scheme predicts higher condensation rates, but that almost everywhere else, the condensation rate is higher in the SBM scheme simulations. In the RDB1600 and SBM1600 simulations, the RDB scheme predicts lower condensation rates almost everywhere. In all cases, the ratios are lowest (RDB rates are lower than SBM rates) where $N\bar{D}$ is large.

For evaporation (Fig. 4.2d-f), the RDB and SBM rates are more similar than for condensation. The disagreement is worst for very low relative humidity values, very low integrated diameter values, as well as for moderate values of both quantities. In all of these cases, the difference is 25% or more. However, where evaporation occurs most frequently (at high saturation ratio and low integrated diameter; not shown), the differences are generally less than 10%. Thus it appears that the evaporation rates between the two schemes generally agree better than do the condensation rates.

There are many potential reasons why the condensation and evaporation rates are different between the two schemes. As the following analysis will show, one major source of discrepancy is that the cloud droplet size distribution assumed by the RDB scheme is not always representative of what the SBM scheme simulates.

b. Shape Parameter

As can be seen in the condensation equation for the RDB scheme (Eq. 4.2), when a gamma distribution is assumed, the condensation rate is proportional to the shape parameter ν such that a higher shape parameter results in higher condensation rates. To assess whether the use of a constant shape parameter could explain differences between the RDB and SBM average condensation rates, we find the best-fit shape parameters for the cloud droplet size distributions at every cloudy grid point in the SBM simulations and then evaluate their mean for each point in the S and $N\overline{D}$ phase space. More information about the fitting methods can be found in the supplemental materials.

Figure 4.4 displays a scatterplot of the average shape parameters and the condensation and evaporation rate ratios presented in Figure 4.3 for each of the three sets of simulations. The black line plotted in all three panels is the same and shows the theoretical condensation rate ratio that we would expect if there were no other differences between the bin and bulk condensation equations. Recall that in the RDB simulations the shape parameter is constant and has a value of 4. Therefore, specifically, the line is equal to $4\left(\frac{\Gamma(4)}{\Gamma(7)}\right)^{1/3} \Big/ \nu\left(\frac{\Gamma(\nu)}{\Gamma(\nu+3)}\right)^{1/3}$ (see the ν dependency in Eq. 4.2).

In all three pairs of simulations, the mean shape parameter in the SBM simulations explains a large fraction of the variability in the condensation rate ratios, particularly for points with a supersaturation greater than 0.1% (blue dots) or a relative humidity between 90 and 99% (yellow dots). Note that at low shape parameter values, both the theoretical ratio and the modeled ratios indicate that the RDB prediction can be 50% higher than the SBM prediction or more. As the initial aerosol concentration increases, the spread of the points in these two categories around

the theoretical expectation increases but is otherwise qualitatively similar. The increased spread is in part due to the fact that the RDB1600 and SBM1600 simulations cover a larger area of the S and $N\overline{D}$ phase space (Fig. 4.3). Therefore there are more points displayed in Fig. 4.4c and each point has on average fewer instances of condensation included in its average (not shown). As a result, it is difficult to draw conclusions about how the bulk versus bin condensation rates change as a function of the initial aerosol concentration, except to say that aside from the change in spread, there are no startling differences.

The quality of the match between the predicted and the model-derived condensation ratios is lower for points with relative humidity values close to saturation (99-100.1%; orange dots). These points tend to lie much farther from the predicted ratio line and show less correlation with the mean shape parameter value. Many of the points in this category instead have ratios near 1, indicating that both schemes predict the same condensation/evaporation rates. For these points, it is likely that the supersaturation or subsaturation is entirely removed in one time step. In such a case, the shape of the droplet size distribution, as well as all of the other scheme differences, has no impact on the condensation/evaporation rate. If, on the other hand, the supersaturation or subsaturation is nearly, but not entirely removed, the predicted rate is likely sensitive to the scheme's time stepping method and large differences between the condensation/evaporation rates predicted by the two schemes can arise. Finally, at high sub-saturation (0-89% RH; purple dots), the ability of the shape parameter to predict the condensation rate ratio is also diminished. In this regime, cloud water mixing ratio is low and droplets are small. Any of the other differences between the two condensation schemes could be responsible for the disagreement here.

4.5 Discussion and Conclusions

In this study we have conducted a comparison of the condensation rates predicted by a bulk and a bin microphysics scheme in simulations of non-precipitating cumulus clouds run using the same dynamical framework, namely RAMS. The simulations were run with three different background aerosol concentrations in order to consider a large range of microphysical conditions. When the condensation rates were binned by saturation ratio and integrated diameter, the RDB rates were on average higher only for evaporation at low relative humidities and for condensation at low integrated diameter values. Otherwise, the RDB condensation and evaporation rates were consistently lower than those predicted by the SBM. Further analysis indicated that the fixed shape parameter assumed for RDB cloud droplet size distributions explained much of the discrepancy in condensation rates between the two schemes, particularly when the supersaturation was greater than 0.1% or the relative humidity was 90-99%. For relative humidity values close to 100% (99-100.1%), the two schemes often predicted similar rates regardless of the best-fit shape parameter values from the SBM. A number of conclusions can be drawn from these results:

1. A gamma probability distribution appears to be a good assumption for the cloud droplet distribution shape, and exact knowledge of the distribution shape in a bin scheme is often not necessary when using such schemes to minimize errors in the condensation rate in bulk schemes.
2. Given that the shape parameter associated with the bin scheme cloud distributions explains the condensation rate ratios well under most conditions, differences in the formulations of the ventilation coefficient and G terms may not be important except possibly when the relative humidity is low.

3. For relative humidity conditions near saturation, the rates predicted by bin and bulk schemes are often similar since the supersaturation or subsaturation is entirely consumed in one time step. If, on the other hand, the supersaturation or subsaturation is only mostly removed, then large discrepancies in the condensation rates may appear.
4. Except when small residual supersaturation or subsaturation remains at the end of the model time step, the multiple sub-time steps taken by the SBM scheme may not strongly impact the total amount of condensed water in the full time-step and thus it may not be necessary to use such computationally expensive methods.

In conclusion, it appears that *the most important factor for agreement in condensation rates between bin and bulk schemes is the shape parameter*.

We have presented here a novel method for comparing condensation rates between any two microphysics schemes. Although we have only investigated two specific schemes, it is expected that the results can be applied more generally to bulk and bin schemes. Additional work should be conducted using a similar approach in order to compare and evaluate additional microphysics schemes and additional microphysical processes. While it is clear that the effective shape parameter in the bin simulations explains much of the discrepancies in predicted condensation rates between bin and bulk schemes, and that the shape parameter value can change the condensation rate by 50% or more, our understanding of what the most appropriate value of the shape parameter is or how it should vary as a function of basic cloud properties is limited. More work then is also needed on understanding cloud droplet distributions from observations and measurements.

4.6 Appendix A

a. Implementation of the HUCM SBM Scheme into RAMS

While the present study is only concerned with warm phase processes, the methods to interface the Hebrew University SBM scheme with the RAMS radiation scheme (Harrington 1997) will be described here, including those for the ice species. The RAMS radiation scheme uses pre-computed lookup tables for the extinction coefficient, single-scattering albedo, and asymmetry parameter for each hydrometeor species. Three of the hydrometeor species in the SBM correspond directly to species in the RAMS microphysics scheme, namely, aggregates, graupel, and hail. All liquid drops are represented as one species in the SBM, so these liquid bins are classified as either cloud droplets or rain drops using the same size threshold used by the RAMS microphysics scheme to distinguish these two species. Finally, the SBM represents three ice crystal types – plates, columns, and dendrites. Separate RAMS radiation look-up tables already exist for these different ice crystal types, but like for cloud and rain, there are two tables for each crystal type depending on the mean size of the crystals. In RAMS, the small ice crystals are referred to as pristine ice, and the large ice crystals as snow. Again, the same size threshold used to distinguish these two ice categories is used to assign bins from the SBM ice crystal species as either pristine ice or snow. This fortuitous overlap in the ice species has allowed for the seamless integration of the SBM hydrometeor species with the RAMS radiation scheme. For each set of SBM bins that corresponds to a RAMS species, the total number concentration and mean diameter is calculated, a gamma distribution shape parameter of 2 is assumed, and the appropriate set of look-up tables for the corresponding RAMS species is used for all radiative calculations.

b. Simulation Setup

The model setup is designed to simulate *non-precipitating* continental shallow cumulus. The domain is 12.8 x 12.8 km in the horizontal with 50m grid spacing and 3.5km deep with 25m grid spacing in the vertical. The simulations are run for 9.5 hours (after this time the clouds hit the model top) using a 1s time step. The simplified profiles of potential temperature, horizontal wind speed, and water vapor mixing ratio based on an ARM SGP sounding from 6 July 1997 at 1130 UTC (630 LST) presented in Zhu and Albrecht (2003) (see their Fig. 3) are used to initialize the model horizontally homogeneously. The initial profiles of potential temperature and relative humidity are reproduced in Figure 4.5. The wind direction is taken to be 0° throughout the domain. Random temperature and moisture perturbations are applied to the lowest model level at the initial time. Simulations are run with both the newly implemented Hebrew University SBM and the standard RAMS double-moment bulk (RDB; Saleeby and Cotton 2004), which is a double-moment bulk microphysics scheme that uses pre-computed look-up tables generated from bin microphysics schemes for some processes. The Harrington (1997) radiation scheme is used for simulations with both microphysics parameterizations. Surface fluxes were predicted using the LEAF-3 land surface model (Walko et al. 2000a) and a short grass vegetation type was assumed.

Some modifications were made to the model for this study only in order to make the two microphysics schemes more directly comparable. The calculation of relative humidity was changed in the RDB scheme to make it the same as the calculation in the SBM. The SBM does not include a parameterization for aerosol surface deposition, so this process was turned off in the RDB scheme. Finally, the regeneration of aerosol upon droplet evaporation was deactivated

in both microphysics schemes. Aerosol concentrations were initialized horizontally and vertically homogeneously. Aerosol particles did not interact with radiation.

c. Shape Parameter Fitting

Best-fit gamma distribution parameters are found for the cloud droplet size distributions predicted by the SBM simulations. In the SBM, no distinction is made between cloud and rain; however, in order to fit only the part of the distribution corresponding to cloud droplets, such a distinction must be made. We define cloud droplets as belonging to one of the first 15 bins of the SBM liquid array, which corresponds to a maximum cloud droplet diameter of 50.8 μm. Many methods are available to find such best-fit parameters, but they generally all give similar results (McFarquhar et al. 2014). Here we use the maximum-likelihood estimation method and find best-fits that minimize the error in the total number concentration. Using this method, the size distributions are first normalized by the corresponding total number concentration, leaving only D_n and ν as free parameters of the distribution (Eq. 4.1).

Note that while we could determine the values of S and $N\bar{D}$ that existed before condensation occurred, we cannot determine the value of the best-fit shape parameter for this time because the change in mixing ratio of each bin is not output by RAMS. Thus the average shape parameters used in the analysis are those that exist at the end of the time step. Nonetheless, given the short time step used in these simulations, it is not expected that the best-fit shape parameter would change much in one time step and thus the impact of using the post-condensation shape parameters is not expected to have a large impact on the results.

4.7 Table and Figures

Table 4.1. Definitions of symbols used.

Symbol	Definition
e_s	Saturation water vapor pressure
D	Cloud droplet diameter
$\bar{D}$	Volume mean cloud droplet diameter. $r_c=\pi\rho_w N\bar{D}^3/6$
D_n	Characteristic cloud droplet diameter. $D_n^3=\bar{D}^3\Gamma(\nu)/\Gamma(\nu+3)$
$f_{v,RDB}$, $f_{v,SBM}$	Ventilation coefficients
G_{RDB}, G_{SBM}	Term to account of the impact of latent heat release on the condensation process. See Walko et al. (2000) and Khain and Sednev (1996) for the formulations used in the RDB and SBM schemes, respectively.
N	Cloud droplet number concentration
n	Concentration of cloud droplets per unit cloud droplet diameter interval
r_c	Cloud water mixing ratio
r_v	Water vapor mixing ratio
r_{vs}	Saturated water vapor mixing ratio
S	Saturation ratio
T	Air temperature
t	Time
Γ	Gamma function
ν	Gamma distribution shape parameter
( )*	Value of a quantity after advection and all other model processes but before microphysical processes have occurred during a model time step

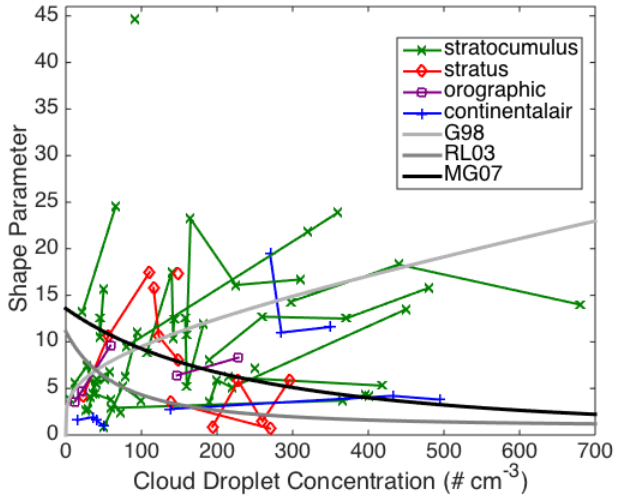

Figure 4.1. Shape parameter (ν) values as a function of cloud droplet concentration as reported by Miles et al. (2000) from 16 previous studies. Values, cloud classification, and groupings are based on their Tables 1 and 2. The three solid gray lines show proposed relationships between the cloud droplet concentration and the shape parameter. G98 is from Eq. 9 in Grabowski (1998). RL03 is from Eq. 3 in Rotstayn and Liu (2003) with their α=0.003. MG07 is from Eq. 2 in Morrison and Grabowski (2007). All equations were originally written for relative dispersion, which is equal to $\nu^{-1/2}$, and have been converted to equations for ν for this figure.

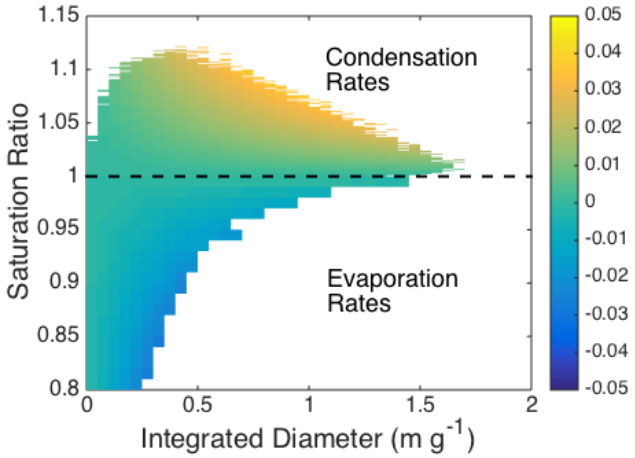

Figure 4.2. The average condensation and evaporation rates (g kg^{-1} s^{-1}) as a function of saturation ratio (S) and integrated diameter ($N\bar{D}$) for the SBM100 simulation.

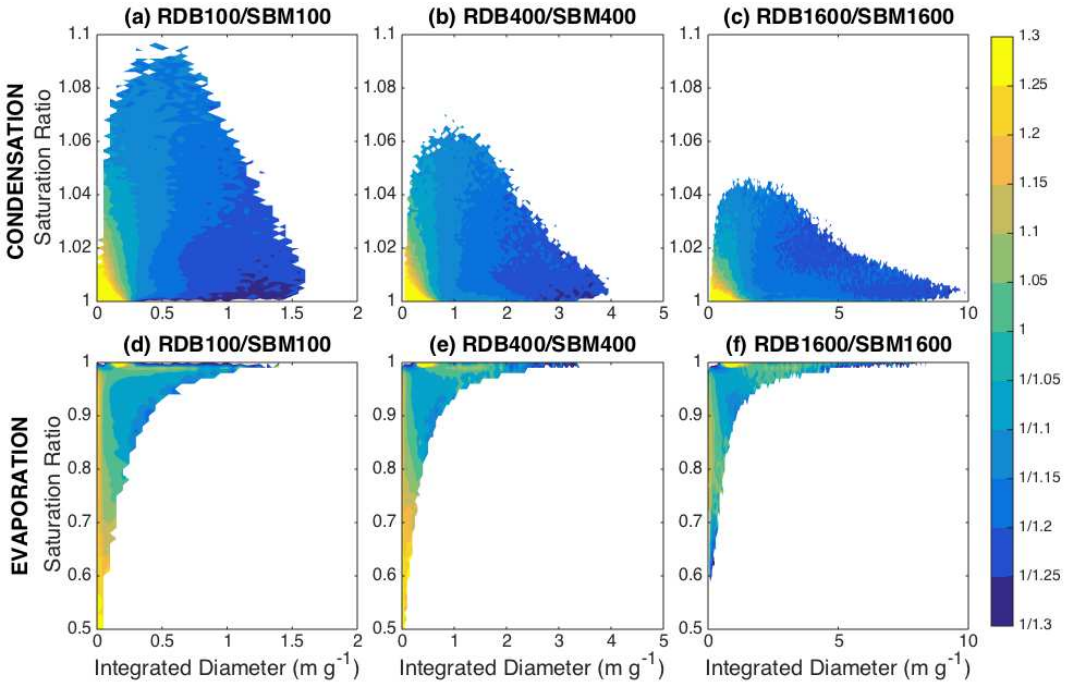

Figure 4.3. The ratio of the RDB to SBM (a-c) condensation and (d-f) evaporation rates as a function of saturation ratio (S) and integrated diameter ($N\bar{D}$) for each pair of simulations. Note the differences in axes limits.

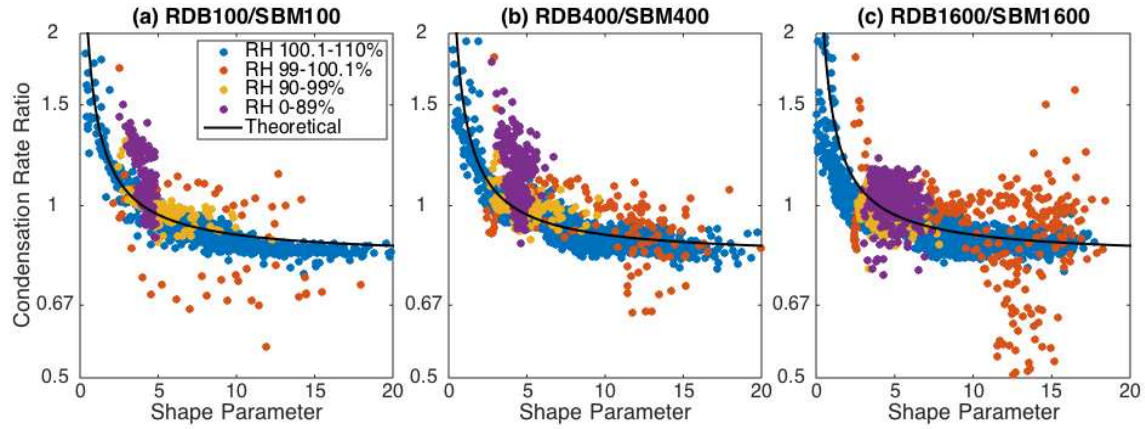

Figure 4.4. Scatterplots of the condensation rate ratio (RDB/SBM) and mean best-fit shape parameter. Each point shows values from a joint bin in the S and $N\bar{D}$ phase space in Figure 4.3. The black line is identical in all three plots and displays the theoretical condensation rate ratio obtained by assuming that no other differences exist between the two schemes. See the text for more details.

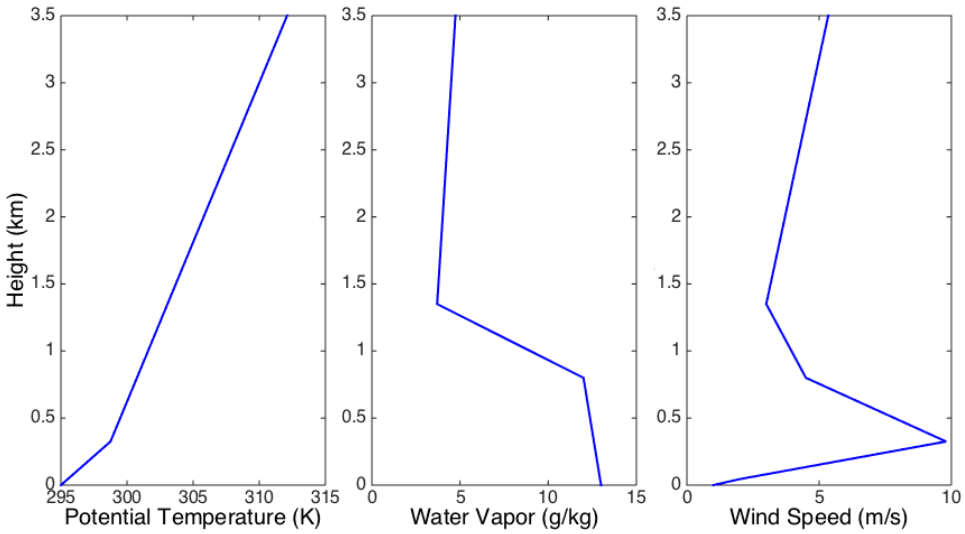

Figure 4.5. Profiles of potential temperature, water vapor, and wind speed used to initialize the simulations from Zhu and Albrecht (2003).

5. IMPACTS OF THE SHAPE OF THE CLOUD DROPLET SIZE DISTRIBUTION ON THE MICROPHYSICAL AND OPTICAL PROPERTIES OF SHALLOW CUMULI

5.1 Introduction

Microphysical schemes used in numerical cloud, weather, and climate models usually need to assume a probability distribution to describe the size distribution of each hydrometeor species that is represented by the model. Such schemes are referred to as "bulk" microphysics schemes. The two distributions that are most commonly used within such schemes are the exponential and gamma probability distributions. Following Walko et al. (1995), the gamma probability distribution ($n(D)$) is expressed as

$$n(D) = \frac{N_t}{D_n^{\nu}\Gamma(\nu)} D^{\nu-1} e^{-D/D_n} \tag{5.1}$$

where N_t is the total number concentration of the hydrometeor species, D is the species diameter, D_n is called the characteristic diameter, and ν is referred to as the shape parameter. Note that the gamma distribution reduces to the exponential distribution when ν =1. The shape parameter influences the width of the size distribution, and can be directly related to the relative dispersion (ε, the ratio of the standard deviation of cloud droplet size to the mean cloud droplet size) of the distribution by $\nu = 1/\varepsilon^2$ (e.g. Hsieh et al. 2009). This relationship indicates that higher shape parameters correspond to narrower size distributions and vice versa.

To fully describe the gamma distribution given by Eq. 5.1, three parameters must be known: N_t, D_n, and ν. In a two-moment bulk microphysics scheme, N_t and q, the mass mixing ratio of the species, are explicitly predicted by the model. Furthermore, for spherical water droplets, D_n and ν can shown to be related to N_t and q through the relationship

$$q = N_t \frac{\pi}{6} \rho_w D_n^3 \frac{\Gamma(\nu + 3)}{\Gamma(\nu)} \tag{5.2}$$

With this relationship, D_n can be solved for if ν is known. However, in single and double moment bulk microphysics schemes, ν is not known, and must be set to a constant value or diagnosed in some other way (e.g. Grabowski 1998; Rotstayn and Liu 2003; Morrison and Grabowski 2007; Thompson et al. 2008; Geoffroy et al. 2010). Triple-moment schemes (e.g. Milbrandt and Yau 2005b; Shipway and Hill 2012; Loftus et al. 2014) on the other hand, which additionally predict the sixth moment of the distribution, can explicitly solve for this remaining parameter of the gamma distribution. This is the primary advantage of these schemes over lower-moment microphysics schemes.

Since the shape parameter for cloud droplets is set to a constant for the simulation duration when using single- and double-moment schemes, there have been efforts to determine the most appropriate value of this parameter from observations of cloud droplet distributions. Table 5.1 shows a summary of estimates of this parameter from several recent field measurements of just one cloud type, shallow cumulus clouds. Estimated values range from about 2 to 14. There do not appear to be any consistent differences based on region or surface type (land vs. ocean). Similarly wide ranges of values were found by Miles et al. (2000) who reported primarily on stratus and stratocumulus clouds. Furthermore, the studies in Table 5.1 which include clouds sampled in different levels of air pollution do not agree on whether the shape parameter should increase or decrease with increasing aerosol concentration, with two studies finding an increase (Goncalves et al. 2008; Martins and Silva Dias 2009), two finding a decrease (Costa et al. 2000; Pandithurai et al. 2012) and one finding a nonmonotonic change (Lu et al. 2008). There are many potential reasons for these discrepancies ranging from differences in the boundary layer environment to sampling and analysis methods. Regardless, Table 5.1

indicates that the shape parameter for the cloud droplet size distribution is poorly constrained by observations.

Other investigators have sought to understand the relative dispersion, and thus also the shape parameter, both from a theoretical perspective and through modeling studies using bin microphysics schemes which, by design, preclude the need for an assumed size distribution function (Khain et al. 2015). Processes such as collision-coalescence and entrainment decrease the shape parameter (Paluch and Baumgardner 1989; Politovich 1993; Lu and Seinfeld 2006), whereas condensation will increase it (Yum and Hudson 2005; Liu et al. 2006; Peng et al. 2007; Hsieh et al. 2009b; Wang et al. 2011). When only considering condensation, theoretical arguments and parcel modeling have shown that the relative dispersion decreases as vertical velocity increases, and increases as cloud droplet number concentration (and therefore to a first degree aerosol concentration) increases (Yum and Hudson 2005; Liu et al. 2006; Peng et al. 2007; Pinsky et al. 2014). Observations compiled by Liu and Daum (2002) appear to confirm that the relative dispersion increases as aerosol concentration increases, as do some data from individual field campaigns (e.g. Pawlowska et al. 2006). These findings have led to the term "dispersion effect" which refers to the effect of this relationship on the first indirect effect (e.g. Chen and Penner 2005). However, other observations compiled by Miles et al. (2000), observations from individual field campaigns (Zhao et al. 2006; Hsieh et al. 2009; Geoffroy et al. 2010; Lu et al. 2007, 2008), and bin microphysics simulations of stratocumulus clouds (Lu and Seinfeld 2006) show a constant or decreasing relative dispersion with increasing droplet or aerosol concentration.

In addition to the impact of the relative dispersion/shape parameter on the radiative properties of clouds, the shape parameter also can have a large impact on microphysical process

rates (Milbrandt and Yau 2005a). Yet little work has been done to understand how sensitive simulations are to the value of the shape parameter for cloud droplet size distributions. Two exceptions are Morrison and Grabowski (2007) and Gonçalves et al. (2008) both of whom found that the sensitivity of cloud properties to the shape parameter is potentially large. It seems then that we are still far from understanding the behavior of the relative dispersion of cloud droplet size distributions, but that understanding this behavior could be important in enhancing our understanding of cloud processes and radiation on local through global scales (Peng and Lohmann 2003; Rotstayn and Liu 2003; Chen and Penner 2005).

In this study we will use simulations with a spectral bin microphysics scheme to investigate the average value of the relative dispersion and shape parameter as a function of aerosol concentration in *non-precipitating* shallow cumulus clouds. These values will be used to guide simulations with a bulk microphysics scheme in order to investigate the sensitivity of the condensation rates, and the cloud physical and optical properties to the value of the shape parameter.

5.2 Methods

In this study, the Regional Atmospheric Modeling System (RAMS; Cotton et al. 2003) is used to run simulations of shallow cumulus clouds over land. These are the same simulations that were run in Chapter 4 and are briefly described again here. The model domain was 12.8 x 12.8 x 3.5 km with 50m grid spacing in the horizontal and 25m grid spacing in the vertical, and the simulations were run for 9.5 hours with a 1s time step. Semi-idealized thermodynamic profiles (Zhu and Albrecht 2003) from the ARM SGP site in Oklahoma were used to initialize the model horizontally homogeneously, but the wind shear was set to 0. The simulations employed either

the RAMS bin-emulating double-moment bulk microphysics scheme (RDB; Saleeby and Cotton 2004; Saleeby and van den Heever 2013), or the Hebrew University SBM (Khain et al. 2004). In both schemes, the aerosol particles were depleted upon cloud droplet activation, but no other aerosol processes were included in order to keep the aerosol physics as similar as possible between the RDB and SBM microphysics schemes. Since the cloud base and boundary layer height were continuously rising in these simulations, new aerosol particles were continually being entrained from the free troposphere into the boundary layer and therefore the aerosol population did not become depleted too rapidly. Hydrometeors were radiatively active (Harrington 1997), but aerosol particles were not.

Three simulations were run with the SBM scheme using spatially homogeneous aerosol concentrations of 100, 400, and 1600 cm^{-3} (SBM100, SBM400, SBM1600). These concentrations are representative of ultra-clean, moderate, and polluted concentrations of accumulation mode aerosol particles at the ARM SGP site (Sheridan et al. 2001). No other source of new particles was present in the simulations. Twelve simulations were run with the RDB scheme. Four simulations were run with each of the three aerosol concentration values used for the SBM simulations with shape parameter values of 2, 4, 7 and 14 for the cloud droplet size distribution. The choice of these values will be discussed below. These simulations will be designated as RDBaero-NUx, e.g. RDB100-NU2 for the simulation with an aerosol concentration of 100 cm^{-3} and a shape parameter value of 2. The simulations are summarized in Table 5.1. In all simulations, all ice processes were turned off. Additionally, although these simulations are of non-precipitating clouds, small amounts of drizzle and rain do form, particularly in the SBM100 and RDB100 simulations. For the RDB simulations, a shape parameter value of 2 was used for both the drizzle and rain hydrometeor categories.

5.3 Results

a. Shape Parameter Distributions

Best-fit shape parameters for the cloud droplet size distributions from the SBM simulations were found using maximum-likelihood estimation methods (see Chapter 4 for more details) and are shown in Figure 5.1. The average value of the best-fit shape parameter is about 6.5, which is a moderate value in comparison to the observations listed in Table 5.2. The frequency distributions of the best-fit shape parameters take on different shapes when they are separated into subsaturated and supersaturated regions. In supersaturated regions, the average best-fit shape parameter increases to about 7 and the distribution of best-fit shape parameter values is slightly broader, whereas in subsaturated regions it decreases to about 4.5 and the distribution of best-fit shape parameter values is much narrower. These results are consistent with past theoretical studies that have shown that the shape parameter (relative dispersion) should increase (decrease) during condensation, and vice versa during evaporation (Yum and Hudson 2005; Liu et al. 2006; Peng et al. 2007; Hsieh et al. 2009b; Wang et al. 2011; Pinsky et al. 2014). Additionally, lower values of the shape parameter are expected when mixing is strong (Lu and Seinfeld 2006), and in these clouds mixing should be stronger in the subsaturated areas along cloud edges rather than in the supersaturated areas located closer to the cloud center. In the bulk microphysics simulations discussed below, the impacts of this spatial variability of the shape parameter on the cloud characteristics will be explored.

Interestingly, there is no strong dependence of the average best-fit shape parameter on the initial aerosol concentration, either in the full data set or when the data are subsetted by relative humidity (mean values are given on Fig. 5.1). The lack of such an aerosol dependency may be due to changes in self-collection, vertical velocity, or mixing. Table 5.3 shows that all three of

these quantities change with increasing droplet concentration in a manner that would counteract size distribution narrowing by the increased average condensation rates that are also evident in Table 5.3. If there is in fact no dependence on aerosol concentration, this may explain why previously reported values of the shape parameter from observations of shallow cumulus clouds do not consistently show either an increase or a decrease in shape parameter with aerosol concentration. Other factors, such as the width of the aerosol distribution which was initially the same in all of the SBM simulations, may be important for determining whether the best-fit shape parameter increases or decreases as the aerosol concentration and cloud droplet concentration increase. Such factors have not been tested here.

Finally, it should be noted that the average value of the best-fit shape parameter is highly dependent on the averaging area. For the results shown in Figure 5.1, shape parameters were calculated at every cloudy grid point and hence there was no averaging over multiple grid points. If, however, the size distributions are averaged over multiple grid points before fitting, extreme values become less frequent, and the average itself decreases to lower values (not shown). Miles et al. (2000) presented similar findings pertaining to observational analyses. On the other hand, bin microphysics schemes have a tendency to artificially broaden the size distributions of hydrometeors during condensation (e.g. Khain et al. 2000) and therefore the shape parameter may be artificially decreased. These caveats should be kept in mind when interpreting the results of this and other studies which examine the distribution width of hydrometeor distributions.

b. RDB Simulations

Despite not finding a dependence of the shape parameter on the initial aerosol concentration, we still wish to test the sensitivity of the cloud characteristics to the shape

parameter using the RDB (bulk) microphysics scheme, since observationally estimated values of this parameter vary so much (Table 5.2; Miles et al. 2000; Liu and Daum 2002). As described above, several simulations were run with the RDB microphysics scheme with shape parameter values of 2, 4, 7, and 14. The values of 4 and 7 correspond to the averages found in the sub- and supersaturated regions of the bin simulations, and the values of 2 and 14 are the extreme average values reported in the literature for shallow cumulus clouds (Table 5.2). The analysis will focus primarily on the RDB400 simulations for simplicity, but note that the trends are qualitatively the same for the RDB100 and RDB1600 simulations as well. It is worth remembering that the value of the shape parameter is typically kept constant, both spatially and temporally, when using bulk schemes. A fifth simulation was run for RDB400 with the shape parameter set equal to 4 in subsaturated regions and 7 in supersaturated regions (NUe4-NUc7) in order to determine whether including a spatially varying shape parameter is important (Table 5.1). Whether a grid point was subsaturated or supersaturated was assessed prior to the call to the condensation routine at each time step. This approach is blunt; certainly we are still missing most of the spatial and temporal variability of the shape parameter with this test, but the test should still indicate whether or not spatial variability is important.

c. Theoretical Expectation

Before examining the results of the RDB400 simulations, it is useful to understand how the shape parameter is expected to alter the simulations. In these simulations of *non-precipitating* cumulus clouds, the most important microphysical process is condensation. The condensation equation, when integrated over a gamma distribution of cloud droplet sizes and neglecting the

ventilation coefficient (up to a 10% correction), is related to the shape parameter in the following way:

$$\frac{\partial r_c}{\partial t} \propto \nu \left(\frac{\Gamma(\nu)}{\Gamma(\nu+3)} \right)^{1/3} \tag{5.3}$$

This relationship between the condensation rate and the shape parameter is shown in Figure 5.2. It is evident from this figure that the term rapidly increases at low values of the shape parameter and more slowly approaches 1 as the value increases. There is a 35% percent increase in the total condensation rate from the low shape parameter value of 2 to the high value of 14 used in the simulations. Even the simulation with a shape parameter value of 4 can expect a ~20% increase in the condensation rate if all else is equal (and the condensation rate is non-zero). Therefore, from a theoretical point of view, the shape parameter may be quite important for determining cloud growth rates and cloud droplet properties. However, this theoretical analysis cannot account for the feedbacks that will occur in real clouds, nor how actual condensation rates over a finite time step will be limited by the supersaturation, and so the actual changes in the condensation rate within numerical simulations may be quite different from the values predicted by this simple curve.

c. Condensation Rates

Figure 5.3a shows the average condensation rates across all RDB400 simulations as a function of relative humidity. In agreement with the theoretical example, the condensation and evaporation rates increase as the shape parameter increases. Where the saturation ratio is greater than 1, the condensation rate becomes less sensitive to the shape parameter as its value increases, which is also in agreement with the theoretical example. However, in the evaporation regime, it

is not clear whether the evaporation rate is becoming less sensitive to the shape parameter as its value increases or not. Furthermore, the percent increase in the condensation and evaporation rates (Fig. 5.3b) are much higher than predicted by the theoretical example, particularly for evaporation where the percent increase exceeds 500% for the NU14 test. Lastly, the percent change in condensation or evaporation rate should not be a function of saturation ratio (see Eq. 5.3), yet Figure 5.3b clearly shows that the percent change generally increases as the saturation ratio decreases. These results suggest that the shape parameter has a larger impact on condensation/evaporation processes than would be expected based on the theoretical example as a result of feedbacks that occur within the cloud.

While the focus of the discussion thus far has been on the impact of the shape parameter on the condensation and evaporation rates, the shape parameter is used by the RDB scheme for other microphysical calculations too. For cloud droplets, it is also used in the collision-coalescence scheme, and to determine what fraction of the droplet number concentration to deplete during evaporation. This latter rate will be referred to as the number evaporation rate. The impact of the shape parameter on the collision-coalescence process is small (not shown) in these simulations of non-precipitating clouds. However, the impact of the shape parameter through the number evaporation rate could be important. To test the relative importance of the shape parameter for the condensation/evaporation rate and for the number evaporation rate, we ran additional RDB400 simulations for each shape parameter value (2, 4, 7, 14) in which the shape parameter was changed only for one process at a time, and all other processes used an arbitrary shape parameter value of 5. Simulations where the shape parameter was changed only for the condensation equation are referred to as NUx-cond (e.g. NU2-cond), and simulations

where the shape parameter was changed only for the number evaporation rate are referred to as NUx-numevap (e.g. NU2-numevap). See Table 5.1 for a summary of these simulations.

In the NUx-cond tests, a quantitatively different dependency of the condensation rate on relative humidity emerges (Fig 5.3c, d). The percent increase in condensation and mass evaporation rates is now much less dependent of the saturation ratio (note the change in scale on the y-axis), and the values of the percent increase from NU2-cond are much closer to those predicted in the theoretical example (Fig. 5.2). These results therefore suggest that when the shape parameter is varied only in the condensation equation there are no strong feedbacks between the shape parameter and droplet characteristics.

Strong feedbacks do exist when the shape parameter is varied only for the number evaporation rate calculations. The NUx-numevap tests (Fig. 5.3e, f) clearly reveal that the value of the shape parameter used for the number evaporation rate has a much larger impact on *both the evaporation and the condensation rates* than does the value of the shape parameter used directly in the evaporation and condensation rate calculations (Fig. 5.3c, d). In the RDB microphysics scheme, the fraction of droplets depleted is stored in a look-up table and is a function of the fraction of droplet mass evaporated and the shape parameter. These functions are shown in Figure 5.4 and were developed based on a bin model representation of the evaporation process (Meyers et al. 1997). It can be seen that the fraction of the number of droplets evaporated decreases rapidly as the shape parameter increases. Therefore, during a simulation, more droplets "survive" evaporation during one time step when the shape parameter is higher, such that the number concentration is higher at the end of the time step, all else being equal including the initial mixing ratio. Since the evaporation rate is proportional to $N_t^{2/3} q^{1/3}$ (e.g. Pinsky et al. 2013), during the following time step, the relative increase in number concentration in the higher shape

parameter case acts to increase the mass evaporation rate. It is this feedback process that explains why the average evaporation rate is so much enhanced for higher values of the shape parameter as seen in Figures 5.3a and 5.3e. This feedback results from the basic physics associated with condensation and therefore is not specific only to the microphysics schemes being considered here.

The impact of the shape parameter on the fraction of evaporated droplets is the more important impact on condensation rates, as well as evaporation rates, even though there is of course no change in the droplet concentration during condensation. This result suggests that the mixing of saturated and unsaturated cloudy air is more important for the number and size of cloud droplets in the saturated air than is the condensation process itself and has important implications for choosing an appropriate shape parameter in simulations that use a constant value for this parameter. Specifically, *it is more important to represent the size distribution characteristics of the evaporating part of the cloud than it is the condensing part of the cloud.*

Such a conclusion is supported by the NUe4-NUc7 test in which the shape parameter is set to 4 where cloud is evaporating and to 7 where cloud is condensing. Figure 5.3a,b shows that the average evaporation rate in the NUe4-NUc7 test is essentially identical to that in the NU4 test. In other words, the changed shape parameter in the supersaturated regions has little impact in the subsaturated regions of the cloud. The condensation rates in the NUe4-NUc7 test lie between the condensation rates for the NU4 and NU7 tests, though the values generally lie closer to the NU4 test. Therefore, although the condensation rates in the NUe4-NUc7 test are enhanced relative to the NU4 test, they are still heavily influenced by the value of the shape parameter in the subsaturated regions of the cloud.

The same analysis of the condensation and evaporation rates was carried out for the SBM400 simulations and is shown in Figure 5.3g,h. Here, the best-fit values of the shape parameter have been used to find the average condensation rates as a function of both the shape parameter and the saturation ratio. While the lines are not as smooth as in the RDB400-NUx simulations because there are many fewer data points for each shape parameter line, we see the same qualitative behavior in the SBM400 simulations as in the RDB400-NUx simulations. Specifically, the condensation and evaporation rates increase as the shape parameter increases, and the evaporation rates are more sensitive to the shape parameter than are the condensation rates. Also, just as with the RDB results, this sensitivity is much higher than was predicted by the theoretical example (Fig. 5.2) and suggests that the same feedbacks that are present in the RDB simulations act in the SBM simulations to enhance the sensitivity of the condensation and evaporation rates to the shape parameter. However, the enhancement is not as large in subsaturated cloudy air as in the RDB simulations, suggesting that either (1) the dependence of the number evaporation rate on the shape parameter is not as strong, and/or (2) the mixing of regions with different shape parameters decreases the enhancement.

The first possibility can be partly assessed by plotting the fraction of droplets evaporated as a function of the fraction of mass evaporated and shape parameter for the bin scheme (Figure 5.4). It can be seen that the sensitivity of the number fraction evaporated to the shape parameter is much less than that parameterized by the RDB scheme, although both schemes do show that a higher fraction is evaporated for a lower shape parameter value. The differences are in part due to the fact that the two schemes have different minimum sizes for cloud droplets. It is unclear from this analysis which scheme has the more appropriate relationship between the shape parameter and number evaporation rate since both are based on bin microphysics.

In order to evaluate the second possibility, Figure 5.3g,h also shows the average condensation rate for all of the cloudy points as a function of saturation ratio (green dashed line). The all-data line lies very close to the ν=4 line in the subsaturated portion of Figure 5.3g,h, suggesting that the average best-fit shape parameter is an appropriate value to use in order to capture the average behavior of the evaporation rates. In the supersaturated portion of Figure 5.3g,h, the all-data line lies between the ν=4 and ν=7 lines. This increase in the "effective" shape parameter value in the supersaturated region is in agreement with the fitting results in Figure 5.1. However we cannot determine to what extent the value of the all-data line in the supersaturated portion of Figure 3g is influenced by the microphysics of the subsaturated portion. Regardless, we see that the results of the shape parameter tests with the RDB scheme are qualitatively in agreement with the results of the SBM scheme, which supports the validity, and hence findings, of the RDB400 simulation results.

d. Macroscopic Cloud Characteristics

There are large differences in the condensation and evaporation rates as a function of relative humidity when the shape parameter is varied (Fig. 5.3); however, these differences may or may not have a large impact on macroscopic features of the shallow clouds being simulated here. To investigate whether these changes are important for the cloud as a whole, we plot vertical profiles of selected quantities in Figures 5.5 and 5.6 from the simulations in which the shape parameter is changed for all processes. Since the boundary layer depth and cloud base height is increasing in time, creating average vertical profiles of clouds is not trivial. Here, we have used image processing techniques to identify individual clouds. A grid box is considered cloudy if the cloud water mixing ratio is greater than 0.01 g kg^{-1}, and cloudy grid boxes are

defined to be connected using a 6-connected neighborhood, or in other words, cloudy grid boxes must share a full face with its neighbor in order to be connected. For each cloud, cloud base is defined as the first vertical level above the surface that is saturated or supersaturated. All clouds are aligned relative to cloud base, and then mean vertical profiles are calculated. In total there are about 4000-5000 clouds per simulation.

Figures 5.5a and 5.5b show that the cloud averaged condensation and evaporation rates do in fact increase as the shape parameter increases as we expect based on Figure 5.3, and that the differences become larger with increasing height above cloud base. Nonetheless, due to the strong mixing between saturated and unsaturated regions of cumulus clouds, and because the increased condensation and evaporation rates tend to offset one another, the average cloud water content is nearly identical in all simulations in the saturated zones (Fig. 5.5c). In the subsaturated regions of the cloud, the mixing ratio is somewhat increased for the higher shape parameter tests (Fig. 5.5d) despite the fact that the higher shape parameter tests have higher evaporation rates (Fig. 5.5b). The reason for these increased mixing ratios lies in changes to the distribution of cloud mixing ratio values in the subsaturated zone (not shown). In the NU2 test, evaporation rates are slow and there are many points with very low cloud mixing ratios. In contrast, in the NU14 test, evaporation rates are fast and there are many fewer points with very low mixing ratios. As a result of this shift in the distribution of cloudy points in the subsaturated region, the average value of the cloud water content is highest in the NU14 test despite the fact that the evaporation rate in this test is also highest.

Although the cloud water contents are similar across all shape parameter tests, the number concentration is quite different across these tests in both the saturated and subsaturated zones; there are about 50 cm^{-3} more droplets (~400% increase) in the NU14 test than in the NU2

test (Fig. 5.5e,f). Since the cloud water content is similar in all simulations, the change in number concentration results in a change to the average cloud droplet diameter as well – there is a decrease in the average diameter in supersaturated regions of about 5 μm (Fig. 5.5g), and in the subsaturated regions of about 20 mum (Fig. 5.5h) when going from the NU14 test to the NU2 test.

The changes in number concentration in the saturated zone cannot be explained by changes in the number of droplets nucleated (Fig. 5.6a). Instead, these changes are attributed to the impact of the shape parameter on the number evaporation rate (Fig. 5.6b), and the strong mixing that exists between saturated and unsaturated regions. Whereas the changes in evaporation and condensation rates could approximately offset one another, there is no mechanism to offset the decrease in the number evaporation rate (Fig. 5.6b) in the subsaturated regions caused by an increase in the shape parameter. However, recall that aerosol regeneration upon cloud droplet evaporation is not turned on in these simulations. If it had been represented, the mixing of regenerated aerosol particles back into the supersaturated regions of the cumulus clouds, and the subsequent activation of these particles may have been able to offset some of the changes we see to the number concentration of droplets in the supersaturated regions (Fig. 5.5e). The importance of this mechanism should be addressed in a future study.

Finally, the NUe4-NUc7 test more closely resembles the NU4 test than the NU7 test in every quantity shown in Figures 5.5 and 5.6b. This result reinforces the idea that it is more important to represent the relative dispersion of the subsaturated regions than the supersaturated regions of the clouds.

While we have only shown the macroscopic cloud properties from the RDB400 tests, the same qualitative results were seen in the RDB100 and RDB1600 simulations as well, but are not shown here.

f. Cloud Optical Properties

The impact of the shape parameter on the radiative properties of clouds has been discussed previously in a theoretical framework (Liu et al. 2008). It was shown that increasing the relative dispersion (decreasing the shape parameter) leads to a reduction in cloud albedo and radiative forcing when all else is equal. Our simulations have shown that increasing the relative dispersion (decreasing the shape parameter) increases the mean droplet diameter and decreases the number of droplets in cumulus clouds while keeping the cloud water content constant (Fig. 5.5). This increase in the mean droplet diameter will further reduce the cloud albedo and radiative forcing for clouds with higher relative dispersion, and hence the relative dispersion of cloud droplets may be more important than previously thought for determining cloud radiative characteristics.

The column optical depth and albedo for these simulations were calculated from the cloud mixing ratio and number concentration using the same formulae as in Liu et al. (2008) and assuming a value of the asymmetry parameter of 0.85. The average albedo of cloudy columns is shown in Figure 5.7a, where a cloudy column is defined as a column with at least one grid point that has a cloud mixing ratio greater than 0.01 g kg^{-1}. Consistent with Liu et al. (2008), the albedo increases as the shape parameter increases, but the magnitude of the increase, about 0.06 between the RDB100-NU2 and RDB100-NU14 simulations, is greater than that predicted by Liu et al. (2008).

As discussed above, there are two factors that drive the increase in albedo with shape parameter. There is a "direct" factor discussed by Liu et al. (2008) in which, if all else is equal, a higher shape parameter corresponds to a lower effective radius, and hence a higher albedo. There is also an "indirect" factor, which is the impact of the shape parameter on changes to the microphysical properties of clouds. (These "direct" and "indirect" factors are not to be confused with direct and indirect aerosol effects.) To assess which factor is more important, the cloud average albedo is recalculated for the simulations in two different ways. To assess the magnitude of the direct factor, the cloud average albedo is calculated four times for each of the NU2 simulations, once with each of the four values (2, 4, 7, and 14) of the shape parameter tested in this study where that value appears in the albedo equation. To assess the magnitude of the indirect factor, the cloud average albedo for each simulation is calculated using the cloud properties predicted by each simulation, but using a shape parameter value of 2 where that value appears in the albedo equation.

The results of these calculations are shown in Figure 5.8. The increase in cloud albedo from NU=2 to NU=14 due to the direct factor is about 0.01 to 0.025 for a given droplet concentration (Fig. 5.8a). Liu et al. (2008) showed that the maximum change in albedo due to changes in the shape parameter occurs for a cloud albedo of 0.5. Thus when the cloud albedo is less than 0.5, higher albedos respond more strongly to changes in the shape parameter than lower albedos. Consistent with this result, the increase in cloud albedo due to the direct factor (Fig. 5.8a) increases as the average cloud albedo increases since it is always less than 0.5. The magnitude of the indirect factor is more difficult to estimate for a given droplet concentration since all simulations have different mean droplet concentrations; however, the increase in cloud albedo from NU=2 to NU=14 is likely to be about 0.03 (Fig. 5.8c). These two factors added

together approximate the total change in albedo (through a Taylor expansion of the albedo equation). This result indicates that for low average cloud albedo, the indirect factor can amplify the total change in albedo by about a factor of 4, and by about a factor of 2 for more moderate values of the albedo. Thus, it is important to consider both the direct and indirect factors when determining the impact of the relative dispersion on cloud albedo.

Although the average cloud albedo increases with the shape parameter, the cloud fraction decreases as this parameter increases by up to 7% in the cleanest simulations (Fig. 5.7c). The decrease in cloud fraction is not surprising given that the high shape parameter tests result in the highest evaporation rates (Fig. 5.5a). As a result, the domain average albedo, which is more important than the cloud average albedo from a climate perspective, is less sensitive to the shape parameter than the cloud average albedo, though it still increases as the shape parameter increases (Fig. 5.7b). This change in the domain average albedo can again be attributed to direct and indirect factors, where the change in cloud fraction is an indirect factor. The direct change to domain average albedo (Fig. 5.8b; magnitude is about 0.002 to 0.003) is more important than the indirect change to this quantity (Fig. 5.8d; magnitude is at most 0.001) since the change in cloud fraction offsets most of the indirect factor associated with the cloud average albedo. For the shallow cloud regime, a change in albedo of 0.001 from the indirect factor is small and can likely be neglected, but at higher cloud fractions, should the same feedback processes be active, the indirect factor may become much larger and be required for accurate representation of cloud albedo.

Lastly, it is seen that the cloud fraction becomes less sensitive to the shape parameter as the droplet concentration increases (Fig. 5.7c), but that the sensitivity of the cloud average albedo to the shape parameter is approximately independent of the droplet concentration (Fig.

5.7a). Consequently, the domain average albedo will also likely become less sensitive to the shape parameter as the droplet concentration increases. It is difficult to ascertain from these simulations whether this is in fact the case since the average droplet concentrations are so different in the RDB1600 simulations (Fig. 5.7). More simulations are needed in order to address this question.

5.5 Conclusions

In this study, simulations of *non-precipitating* shallow cumulus clouds over land have been conducted using two different microphysical schemes – a spectral bin model (SBM) and the RAMS bin-emulating scheme (RDB) – all using the RAMS dynamical modeling framework. With these simulations, several issues pertaining to the relative dispersion of cloud droplets and the shape parameter of the cloud droplet gamma distribution have been addressed. First, there has been some debate about what the dependence of the relative dispersion (and hence the gamma distribution shape parameter) is on the cloud droplet concentration (e.g. Miles et al. 2000; Liu and Daum 2002). The SBM simulations do not indicate that there is any relationship between these two quantities when averaged over all clouds. While the initial studies on this topic promoted the idea that the relative dispersion of cloud droplet size distributions increases with cloud droplet concentration (Costa et al. 2000; Liu and Daum 2002), there is increasing evidence (Miles et al. 2000; Lu and Seinfeld 2006; Hsieh et al. 2009; Geoffroy et al. 2010), including this study, which suggests that this is not always the case. More work is needed to determine how this dependency is impacted by cloud type and other factors such as the initial aerosol distribution shape and precipitation processes.

The simulations with the RDB scheme gave insight into the potential importance of choosing an appropriate value for the shape parameter and the importance of a spatially-varying shape parameter. These simulations indicated that the evaporation rate can increase fivefold or more for a given RH value as the shape parameter is increased from 2 to 14. Increases in the condensation rate were also seen, but were not as large. These results were also supported by the SBM simulations. The primary pathway for these enhancements to the condensation and evaporation rates was through changes to the number of fully evaporated drops, as demonstrated by both the RDB and SBM schemes. However, these two scheme have very different relationships between the fraction of evaporated mass and number, so it is unclear at this point whether the magnitude of the enhancements are representative of reality or not.

The spatially varying shape parameter test with the RDB scheme revealed that the value of the shape parameter in the subsaturated regions was more important for the cloud characteristics of both the supersaturated and subsaturated regions of the cloud. This is good news for modelers. We have seen from the SBM simulations that the shape parameter is higher in the supersaturated regions of the cloud, and that the possible values for the shape parameter are more widely distributed in the supersaturated regions. However, since the shape parameter in the subsaturated regions is more important for determining the overall cloud characteristics, it *might* be a good assumption to ignore this spatial variation and only use a value of the shape parameter that is appropriate for the subsaturated region. The SBM simulations indicate that this most appropriate value for continental cumulus clouds is in the range of 3-5.

Finally, we investigated the impact of the chosen shape parameter value on cloud optical properties. We found that increasing the shape parameter led to little change in the cloud water content, but to decreases in the mean droplet diameter and hence increases to the cloud albedo.

This observed increase in the cloud albedo supports the previously documented relationship that exists between cloud albedo and relative dispersion when all other cloud properties are constant (Liu et al. 2008). However, changes to the domain average albedo were partially offset by a negative correlation between cloud fraction and shape parameter. While the SBM simulations do not suggest that relative dispersion increases with aerosol concentration, should such a relationship nonetheless exist (e.g. Liu and Daum 2002), the magnitude of the dispersion effect on domain average albedo may decrease as droplet concentration increases due to decreased sensitivity of the cloud fraction to the shape parameter at high droplet concentrations. In this case, the dispersion effect would be most important at low droplet concentrations.

The results discussed here can only be applied to *non-precipitating*, shallow continental cumulus clouds. It is unclear how the results may change as the cloud fraction increases and the clouds become more stratiform, or as the clouds begin to precipitate more. Furthermore, we have only used one bulk microphysics scheme here. Similar studies using other models should be conducted. Finally, these simulations have neglected aerosol regeneration upon evaporation, and this process may be important for shallow cumulus clouds. These additional avenues of research should be addressed in future work.

5.6 Tables and Figures

Table 5.1. Summary of simulations.

Simulation	Description
SBM100, SBM400, SBM1600	Simulations using the bin scheme (Khain et al. 2004) with initial aerosol concentrations of 100, 400, and 1600 cm^{-3}, respectively.
RDB400-NU2, RDB400-NU4, RDB400-NU7, RDB400-NU14	Simulations using the RAMS double-moment bulk scheme (Saleeby and van den Heever 2013) with a cloud droplet shape parameter value of 2, 4, 7, and 14, respectively.
RDB100, RDB1600	Same as above, but using aerosol concentrations of 100 and 1600 cm^{-3}, respectively. For each aerosol concentration, four simulations were run, one with each of the four cloud droplet shape parameter values (2, 4, 7, 14).
NUe4-NUc7	Simulation using the RDB scheme and an initial aerosol concentration of 400 cm^{-3} in which a cloud droplet shape parameter value of 4 is used at subsaturated grid points, and a value of 7 is used at supersaturated grid points
NU2-cond, NU4-cond, NU7-cond, NU14-cond	Simulation using the RDB scheme and an initial aerosol concentration of 400 cm^{-3} in which the given value of the cloud droplet shape parameter (2, 4, 7, or 14) is used only for the condensation rate calculations, and a value of 5 is used for all other processes
NU2-numevap, NU4-numevap, NU7-numevap, NU14-numevap	Simulation using the RDB scheme and an initial aerosol concentration of 400 cm^{-3} in which the given value of the cloud droplet shape parameter (2, 4, 7, or 14) is used only for the calculation of the number of fully evaporated droplets during evaporation, and a value of 5 is used for all other processes.

Table 5.2. Previously reported values of the shape parameter. In some studies only the relative dispersion is reported in which case we have converted these values to shape parameter values.

Paper	Campaign (Location)	Mean cloud droplet concentration (# cm^{-3})	Shape Parameter	Notes
Costa et al. (2000)	Ceará experiment (Brazil)	227 (Maritime)	13.5 (19.3)	Mean (standard deviation). See their Tables 3 and 6.
		265 (Coastal)	10.7 (13.5)	
		375 (Continental)	12.5 (10.6)	
		433 (Urban)	9.8 (10.2)	
Gonçalves et al. (2008)	Dry-to-Wet campaign (Brazil)	521 (Clean)	1.9 (1.3)	Mean (standard deviation) of single flights; see their Table 2.
		816 (Intermediary)	3.8 (1.2)	
		1451 (Polluted)	6.1 (0.7)	
Lu et al. (2008)	GoMACCS (Texas)	206	9.6	Data in their Table 2 split into equal groups based on droplet concentration and averaged.
		282	13.2	
		350	10.9	
Hsieh et al. (2009)	CRYSTAL-FACE (Florida)	480	5.9 (4.5-8.7)	Mean (25^{th}-75^{th} percentiles). See their Table 1.
	CSTRIPE (California coast)	304	3.2 (2.4-4.5)	
Martins and Silva Dias (2009)	LBA (Brazil)	550	4.3	Data in their Table 1 split into equal groups based on droplet concentration and averaged.
		748	5.7	
		1021	5.3	
Hudson et al. (2012)	RICO (Caribbean)	75	7.1	Their Table 2 flight average (row 2^{nd} from bottom)
Pandithurai et al. (2012)	CAIPEEX-I (India)	264	8.6	Data in their Table 1 split into equal groups based on droplet concentration and averaged.
		326	8.1	
		508	7.3	

Table 5.3. Mean quantities averaged over cloudy points (cloud water mixing ratio greater than 0.01 g kg^{-1}) in each of the three SBM simulations. Updraft speed is averaged over cloudy points with a positive vertical velocity, self-collection is scaled by the initial aerosol concentration, and the condensation rate is averaged over cloudy points with a positive condensation rate. The turbulence coefficient gives a measure of sub-grid scale diffusion.

	Updraft speed (m s^{-1})	Scaled self-collection (hr^{-1})	Turbulence Coef. (m^2 s^{-1})	Cond. Rate (g kg^{-1} hr^{-1})
SBM100	1.0	0.18	0.83	0.29
SBM400	1.1	0.058	0.90	0.39
SBM1600	1.2	0.018	0.97	0.49

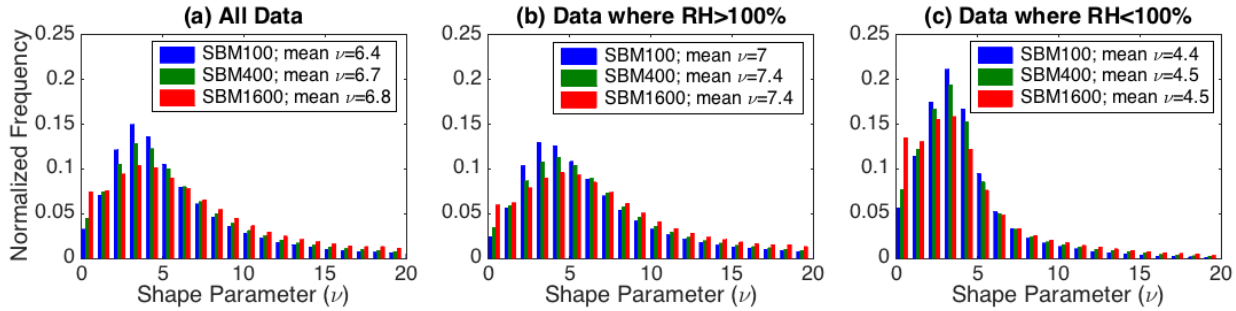

Figure 5.1. Frequency distributions of the best-fit shape parameters from the SBM simulations. (a) All data, (b) data from supersaturated regions, and (c) data from subsaturated regions.

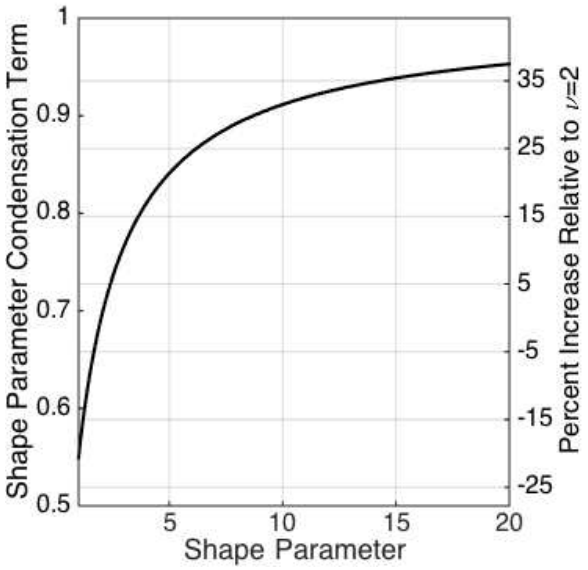

Figure 5.2. Theoretical dependence of the condensation rate on the shape parameter. The left axis show the value of the shape parameter term in the condensation equation (Eq. 5.3), and the right axis shows the percent increase in the condensation rate from the condensation rate when the shape parameter equals 2.

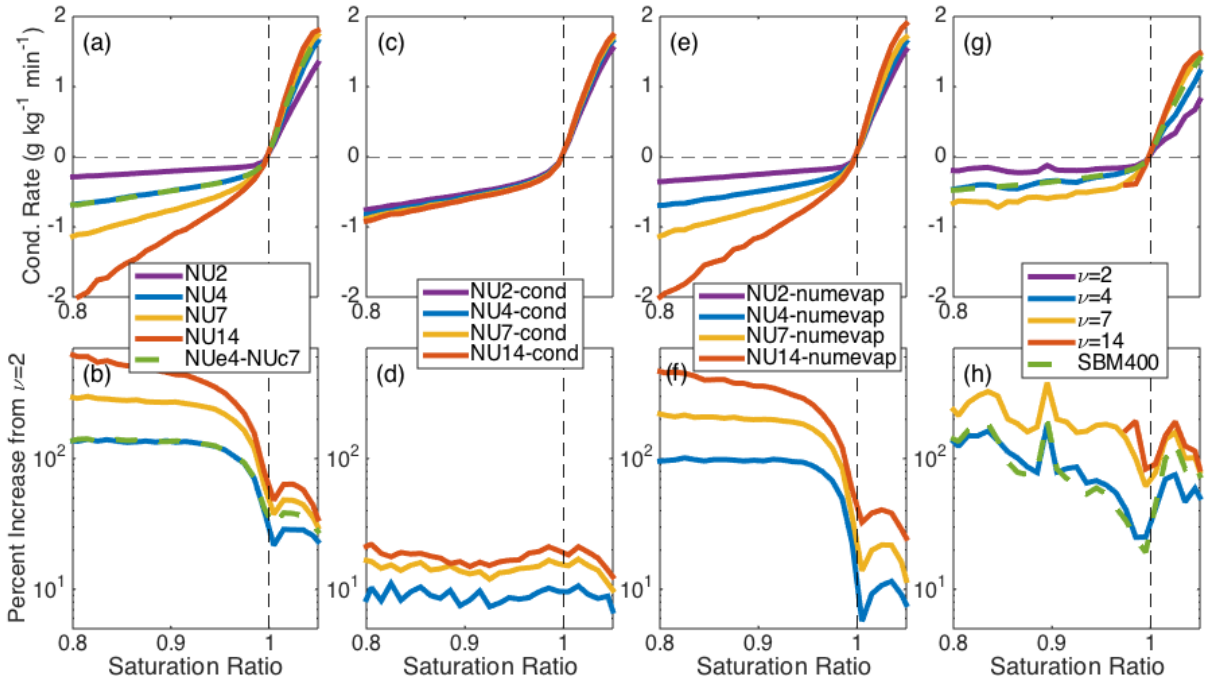

Figure 5.3. (a, c, e, g) The condensation rate as a function of saturation ratio and (b, d, f, h) the percent increase of the condensation rate relative to the condensation rate in the simulation with the shape parameter equal to 2 (this is a different simulation for each pair of plots). The analysis is from RDB400 simulations where the shape parameter is changed for (a, b) all processes (NUx), (c, d) only the condensation equation (NUx-cond), (e, f) only the number evaporation (NUx-numevap). (g, h) Analysis from SBM400 where the average condensation rate has been calculated for points where the best-fit shape parameter (ν) is within 0.5 of the given value in the legend. The green line shows the average condensation rate for all cloudy points in SBM400. See the text for further details.

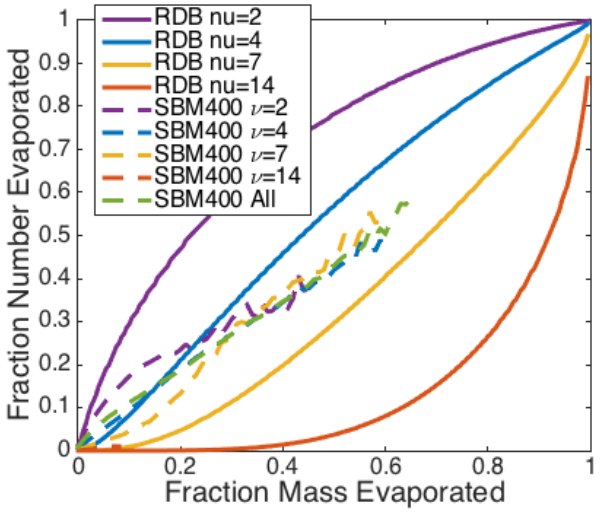

Figure 5.4. The fraction of cloud droplets evaporated as a function of the mass of cloud droplet evaporated and of the shape parameter. Solid lines show the parameterized relationship between these quantities in the RDB microphysics scheme and the dashed lines show the relationship between these quantities based on simulation results from the SBM400 simulation. Average values of the fraction of number concentration evaporated is found for points where the best fit shape parameter (ν) is within 0.5 of the given value in the legend. The green line is the relationship for all cloudy points in SBM400.

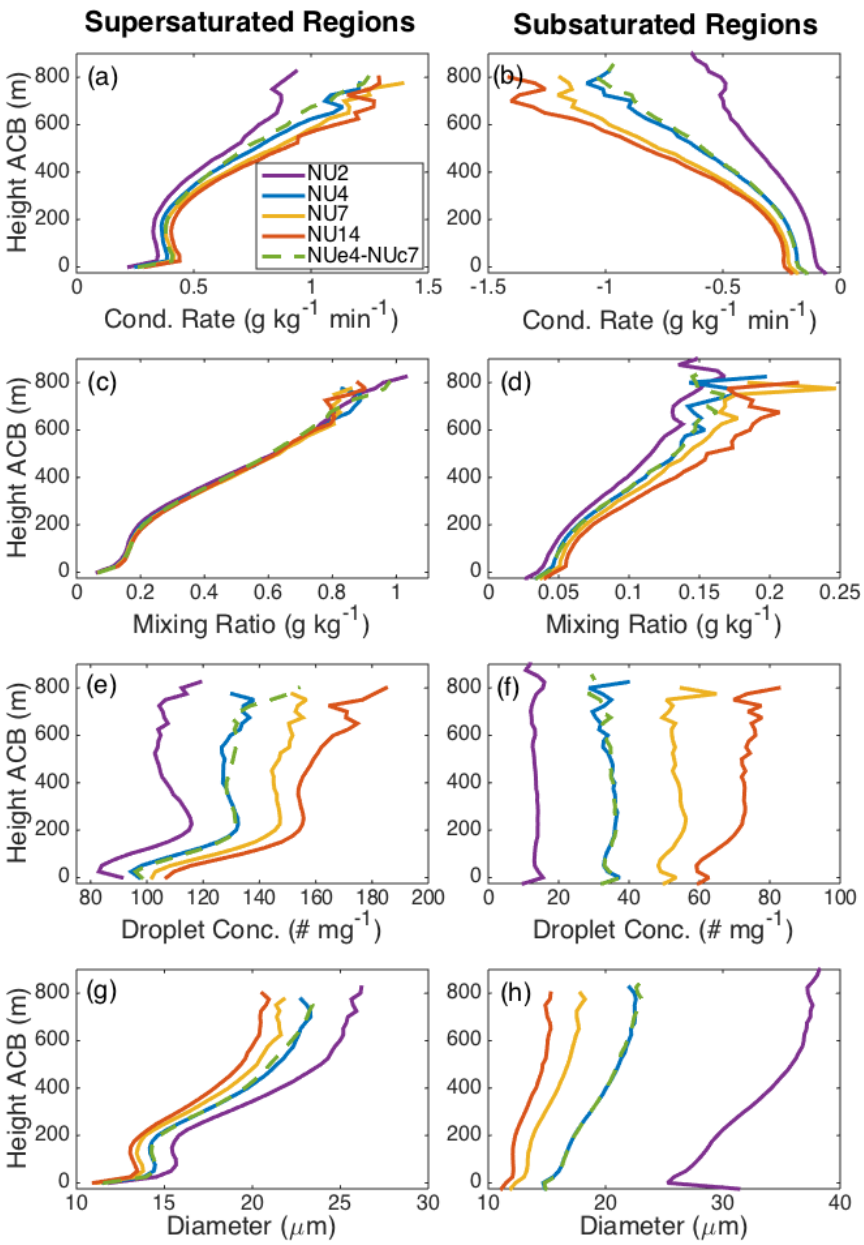

Figure 5.5. Average vertical profiles of (a,b) condensation rate, (c,d) cloud mixing ratio, (e,f) cloud droplet concentration, (g,h) mean cloud diameter in (a,c,e,g) supersaturated regions and (b,d,f,h) subsaturated regions of the clouds from the RDB400-NUx simulations as a function of height above cloud base (ACB).

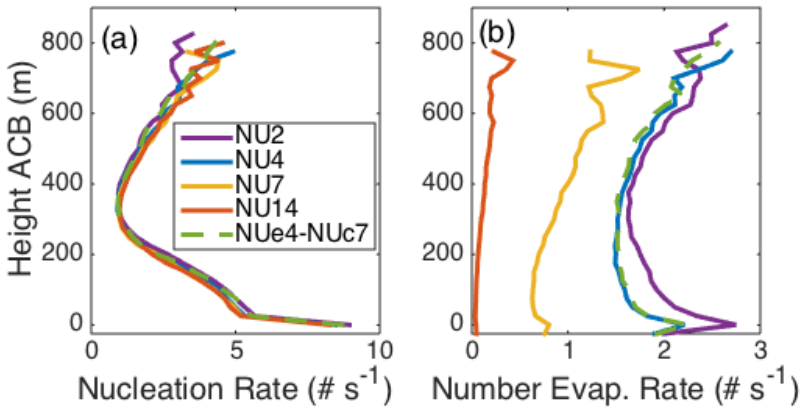

Figure 5.6. Average vertical profiles relative to cloud base of (a) the cloud droplet nucleation rate in supersaturated regions of the cloud and (b) the cloud droplet number evaporation rate in subsaturated regions of the cloud from the RDB400-NUx simulations.

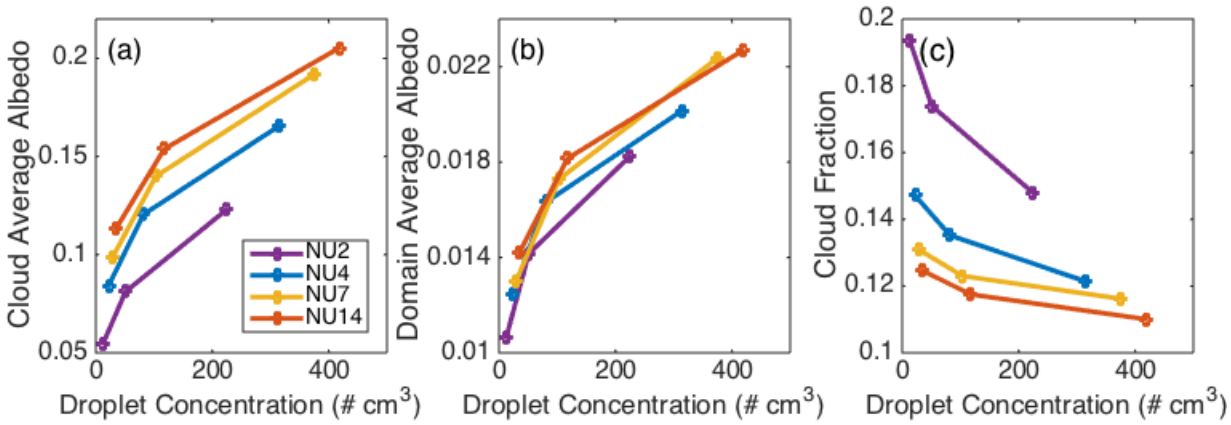

Figure 5.7. (a) Cloud average albedo, (b) domain average albedo where a value of 0 is used where there is no cloud, and (c) cloud fraction plotted as a function of the cloud average droplet concentration for all of the RDB simulations. Each point represents a different RDB simulation.

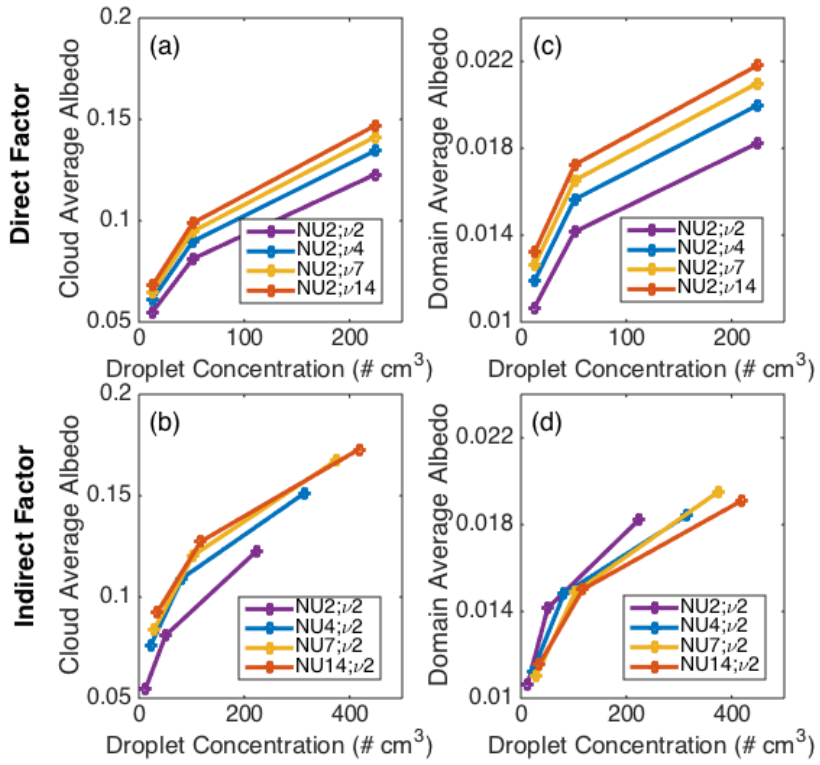

Figure 5.8. (a, b) Cloud average cloud albedo and (c, d) domain average cloud albedo calculated from the RDB simulations but in (b) and (d) all albedo calculations use the NU2 simulations for cloud properties and the indicated value of the shape parameter (NU) in order to assess the "direct factor" and in (a) and (c) all albedo calculations use the indicated simulations for cloud properties but use a shape parameter value of 2 in order to assess the "indirect" factor. See the text for more details.

6. CONCLUDING REMARKS

In this dissertation a number of outstanding issues in cloud microphysics using both theoretical and numerical modeling approaches have been investigated. Taken together, these studies have increased our understanding of warm-phase processes, particularly condensation and evaporation. The specific conclusions of each study have been detailed in each of the chapters; they are briefly summarized here.

In Chapter 2, the topic of condensational invigoration, that is, the convective invigoration due to the influence of aerosol concentration on condensation rates, was addressed. While many previous investigations have quantified this effect in specific or idealized cases, a theoretical approach was utilized here that can be applied to any general case. Previous theoretical work by Pinsky et al. (2013, 2014) to describe the evolution of liquid water and supersaturation with height was applied to equations for buoyancy in order to develop a relatively simple expression describing the upper limit of the difference in kinetic energy between a clean and a polluted parcel. This change in kinetic energy was used as a measure of condensational invigoration and used to explore how this invigoration depends on quantities such as the initial buoyancy and temperature of the clouds. In the future, similar approaches might be appropriate for exploring aerosol-induced invigoration in the mixed and ice phases of convective clouds. Such developments would be particularly important for better understanding which microphysical processes most contribute to aerosol-induced invigoration in deep convective clouds.

The remainder of the dissertation was focused on how cloud microphysics is parameterized in numerical models. While many previous studies had compared single- and double-moment microphysics schemes before, Chapter 3 (which is already published in the peer-

reviewed literature) was one of the first to argue that the existing evidence has conclusively shown double-moment schemes to outperform single-moment schemes in nearly all situations. This argument was supported by original analysis of simple thunderstorm simulations run with a variety of single-moment scheme settings and by the comparison of radiative-convective equilibrium simulations run with both a single-moment and a double-moment scheme. In particular, the radiative-convective equilibrium simulations were unique in that they simulated multiple cloud types simultaneously, whereas most previous studies that compared single- and double-moment schemes focused on only one cloud type or system. While single-moment schemes may be able to simulate single cloud types relatively well in some situations, they are unlikely to be able to simulate multiple cloud types well simultaneously given that there is such a wide range of cloud microphysical properties in different cloud types.

After discussing single- and double-moment simulations, attention was given to comparing double-moment bulk and bin scheme simulations. In Chapter 4 it was found that differences in the width of cloud droplet distribution between the two schemes were primarily responsible for discrepancies in the condensation rates between the two schemes. Further investigation in Chapter 5 revealed that the largest impact of the shape parameter on condensation and evaporation occurred when the shape parameter altered the fraction of fully evaporated droplets. This impact led to a positive feedback loop in which a higher shape parameter leads to higher evaporation rates and slower depletion of entire droplets, which in turn further enhances evaporation rates since the droplet concentration is higher than it would have been otherwise. These enhanced changes in the evaporation rates have potentially large impacts on the macrophysical and optical properties of the clouds. These impacts of the shape parameter

on condensation, evaporation, and cloud properties need to be explored in other cloud types in order to better assess their significance on a global scale.

The ultimate goal of this work has been to improve the parameterization of cloud microphysics in bulk microphysical schemes. Though not specifically investigated here, the same basic results relating to condensation and evaporation of cloud droplets are hypothesized to hold true for the condensation and evaporation of raindrops and for the deposition and sublimation of ice crystals. Previous work has also shown that size distribution widths can have large impacts on other microphysical processes as well (Milbrandt and Yau 2005a; Cohen et al. 2006; Loftus and Cotton 2014), but none of these studies have focused on the condensation process. These previous results, along with the current results, have shown that one potentially fruitful approach for advancing bulk microphysics schemes is to improve the representation of size distribution width. Triple-moment bulk schemes already represent one way to address issues related to size distribution widths. These schemes should be further developed and studied. Also, more attention should be given to developing methods to better diagnose the distribution width in double-moment schemes in order to minimize the computational cost of such improvements to the parameterizations.

REFERENCES

Adams-Selin, R. D., S. C. van den Heever, and R. H. Johnson, 2013: Impact of Graupel Parameterization Schemes on Idealized Bow Echo Simulations. *Mon. Weather Rev.*, **141**, 1241–1262, doi:10.1175/MWR-D-12-00064.1.

Altaratz, O., I. Koren, L. A. Remer, and E. Hirsch, 2014: Review: Cloud invigoration by aerosols—Coupling between microphysics and dynamics. *Atmos. Res.*, **140-141**, 38–60, doi:10.1016/j.atmosres.2014.01.009.

Andreae, M. O., D. Rosenfeld, P. Artaxo, A. A. Costa, G. P. Frank, K. M. Longo, and M. A. F. Silva-Dias, 2004: Smoking rain clouds over the Amazon. *Science*, **303**, 1337–1342, doi:10.1126/science.1092779.

Baba, Y., and K. Takahashi, 2013: Dependency of stratiform precipitation on a two-moment cloud microphysical scheme in mid-latitude squall line. *Atmos. Res.*, **138**, 394–413, doi:10.1016/j.atmosres.2013.12.009.

Baker, M. B., 1993: Variability in concentrations of cloud condensation nuclei in the marine cloud-topped boundary layer. *Tellus B*, **45**, 458–472, doi:10.1034/j.1600-0889.45.issue5.1.x.

Beheng, K. D., 1994: A parameterization of warm cloud microphysical conversion processes. *Atmos. Res.*, **33**, 193–206, doi:10.1016/0169-8095(94)90020-5.

Boucher, O., H. Le Treut, and M. B. Baker, 1995: Precipitation and radiation modeling in a general circulation model: Introduction of cloud microphysical processes. *J. Geophys. Res. Atmos.*, **100**, 16395–16414, doi:10.1029/95JD01382.

Bringi, V. N., and V. Chandrasekar, 2001: *Polarimetric Doppler Weather Radar*. 636 pp.

Brown, P. N., G. D. Byrne, and A. C. Hindmarsh, 1989: VODE: A Variable-Coefficient ODE Solver. *SIAM J. Sci. Stat. Comput.*, **10**, 1038–1051, doi:10.1137/0910062.

Bryan, G. H., and J. M. Fritsch, 2002: A Benchmark Simulation for Moist Nonhydrostatic Numerical Models. *Mon. Weather Rev.*, **130**, 2917–2928, doi:10.1175/1520-0493(2002)130<2917:ABSFMN>2.0.CO;2.

Chen, Y., and J. E. Penner, 2005: Uncertainty analysis for estimates of the first indirect aerosol effect. *Atmos. Chem. Phys. Discuss.*, **5**, 4507–4543, doi:10.5194/acpd-5-4507-2005.

Cohen, C. and E. W. McCaul Jr., 2006: The sensitivity of simulated convective storms to variations in prescribed single-moment microphysics parameters that describe particle distributions, sizes, and numbers. *Mon. Weather Rev.*, **134**, 2547-2565.

Connolly, P. J., A. J. Heymsfield, and T. W. Choularton, 2006: Modelling the influence of rimer surface temperature on the glaciation of intense thunderstorms: The rime-splinter mechanism of ice multiplication. *Quart. J. Roy. Meteor. Soc.,* **132**, 3059-3077, doi:10.1256/qj.05.45.

Costa, A. A., C. J. De Oliveira, J. C. P. De Oliveira, and A. J. D. C. Sampaio, 2000: Microphysical observations of warm cumulus clouds in Ceara, Brazil. *Atmos. Res.*, **54**, 167–199.

Cotton, W. R. and Coauthors, 2003: RAMS 2001: Current status and future directions. *Meteorol. Atmos. Phys.*, **82**, 5–29, doi:10.1007/s00703-001-0584-9.

Dawson, D. T., M. Xue, J. A. Milbrandt, and M. K. Yau, 2010: Comparison of Evaporation and Cold Pool Development between Single-Moment and Multimoment Bulk Microphysics Schemes in Idealized Simulations of Tornadic Thunderstorms. *Mon. Weather Rev.*, **138**, 1152–1171, doi:10.1175/2009MWR2956.1.

Fan, J., L. R. Leung, D. Rosenfeld, Q. Chen, Z. Li, J. Zhang, and H. Yan, 2013: Microphysical effects determine macrophysical response for aerosol impacts on deep convective clouds. *Proc. Natl. Acad. Sci. U. S. A.*, **110**, E4581–E4590, doi:10.1073/pnas.1316830110.

Feingold, G., and A. J. Heymsfield, 1992: Parameterizations of Condensational Growth of Droplets for Use in General Circulation Models. *J. Atmos. Sci.*, **49**, 2325–2342, doi:10.1175/1520-0469(1992)049<2325:POCGOD>2.0.CO;2.

Feingold, G., R. L. Walko, B. Stevens, and W. R. Cotton, 1998: Simulations of marine stratocumulus using a new microphysical parameterization scheme. *Atmos. Res.*, **47-48**, 505–528, doi:10.1016/S0169-8095(98)00058-1.

Ferrier, B., W.-K. Tao, and J. Simpson, 1995: A double-moment multiple-phase four-class bulk ice scheme. Part II: Simulations of convective storms in different large-scale environments and comparisons with other bulk parameterizations. *J. Atmos. Res.*, **52**, 1001–1033.

Ferrier, B. S., 1994: A Double-Moment Multiple-Phase Four-Class Bulk Ice Scheme. Part I: Description. *J. Atmos. Sci.*, **51**, 249–280, doi:10.1175/1520-0469(1994)051<0249:ADMMPF>2.0.CO;2.

Fukuta, N., 1993: Water supersaturation in convective clouds. *Atmos. Res.*, **30**, 105–126.

Geoffroy, O., J.-L. Brenguier, and F. Burnet, 2010: Parametric representation of the cloud droplet spectra for LES warm bulk microphysical schemes. *Atmos. Chem. Phys.*, **10**, 4835–4848, doi:10.5194/acp-10-4835-2010.

Gilmore, M. S., E. N. Rasmussen, and J. M. Straka, 2004: Precipitation Uncertainty Due to Variations in Precipitation Particle Parameters within a Simple Microphysics Scheme. *Mon. Weather Rev.*, **132**, 2610–2627.

Gonçalves, F. L. T., J. A. Martins, and M. a. Silva Dias, 2008: Shape parameter analysis using cloud spectra and gamma functions in the numerical modeling RAMS during LBA Project at Amazonian region, Brazil. *Atmos. Res.*, **89**, 1–11, doi:10.1016/j.atmosres.2007.12.005.

Gorgucci, E., V. Chandrasekar, V. N. Bringi, and G. Scarchilli, 2002: Estimation of Raindrop Size Distribution Parameters from Polarimetric Radar Measurements. *J. Atmos. Sci.*, **59**, 2373–2384, doi:10.1175/1520-0469(2002)059<2373:EORSDP>2.0.CO;2.

Grabowski, W. W., 1998: Toward Cloud Resolving Modeling of Large-Scale Tropical Circulations: A Simple Cloud Microphysics Parameterization. *J. Atmos. Sci.*, **55**, 3283–3298, doi:10.1175/1520-0469(1998)055<3283:TCRMOL>2.0.CO;2.

Gunn, K. L. S., and J. S. Marshall, 1958: The Distribution with Size of Aggregate Snowflakes. *J. Meteorol.*, **15**, 452–461, doi:10.1175/1520-0469(1958)015<0452:TDWSOA>2.0.CO;2.

Haddad, Z. S., S. L. Durden, and E. Im, 1996: Parameterizing the Raindrop Size Distribution. *J. Appl. Meteorol.*, **35**, 3–13, doi:10.1175/1520-0450(1996)035<0003:PTRSD>2.0.CO;2.

Harrington, J. Y., 1997: The effects of radiative and microphysical processes on simulation warm and transition season Arctic stratus. Ph.D. dissertation, Colorado State University, 289 pp. [Available from Department of Atmospheric Science, Colorado State University, Fort Collins, CO 80523.]

Heymsfield, A. J., and R. M. Sabin, 1989: Cirrus Crystal Nucleation by Homogeneous Freezing of Solution Droplets. *J. Atmos. Sci.*, **46**, 2252–2264, doi:10.1175/1520-0469(1989)046<2252:CCNBHF>2.0.CO;2.

Hong, S.-Y., and J.-O. J. Lim, 2006: The WRF single-moment 6-class microphysics scheme (WSM6). *J. Korean Meteorol. Soc.*, **42**, 129–151.

Hong, S.-Y., J. Dudhia, and S.-H. Chen, 2004: A Revised Approach to Ice Microphysical Processes for the Bulk Parameterization of Clouds and Precipitation. *Mon. Weather Rev.*, **132**, 103–120.

Hong, S.-Y., K.-S. S. Lim, Y.-H. Lee, J.-C. Ha, H.-W. Kim, S.-J. Ham, and J. Dudhia, 2010: Evaluation of the WRF Double-Moment 6-Class Microphysics Scheme for Precipitating Convection. *Adv. Meteorol.*, **2010**, 1–10, doi:10.1155/2010/707253.

Hoppel, W. A., G. M. Frick, and J. W. Fitzgerald, 1996: Deducing droplet concentration and supersaturation in marine boundary layer clouds from surface aerosol measurements. *J. Geophys. Res.*, **101**, 26553, doi:10.1029/96JD02243.

Hsieh, W. C., H. Jonsson, L. -P. Wang, G. Buzorius, R. C. Flagan, J. H. Seinfeld, and A. Nenes, 2009a: On the representation of droplet coalescence and autoconversion: Evaluation using

ambient cloud droplet size distributions. *J. Geophys. Res.*, **114**, D07201, doi:10.1029/2008JD010502.

Hsieh, W. C., A. Nenes, R. C. Flagan, J. H. Seinfeld, G. Buzorius, and H. Jonsson, 2009b: Parameterization of cloud droplet size distributions: Comparison with parcel models and observations. *J. Geophys. Res.*, **114**, D11205, doi:10.1029/2008JD011387.

Hudson, J. G., 1980: Relationship Between Fog Condensation Nuclei and Fog Microstructure. *J. Atmos. Sci.*, **37**, 1854–1867, doi:10.1175/1520-0469(1980)037<1854:RBFCNA>2.0.CO;2.

Hudson, J. G., S. Noble, and V. Jha, 2012: Cloud droplet spectral width relationship to CCN spectra and vertical velocity. **117**, 1–11, doi:10.1029/2012JD017546.

Jin, Y. and Coauthors, 2014: The Impact of Ice Phase Cloud Parameterizations on Tropical Cyclone Prediction. *Mon. Weather Rev.*, **142**, 606–625, doi:10.1175/MWR-D-13-00058.1.

Johnson, R. H., T. M. Rickenbach, S. A. Rutledge, P. E. Ciesielski, and W. H. Schubert, 1999: Trimodal Characteristics of Tropical Convection. *J. Clim.*, **12**, 2397–2418, doi:10.1175/1520-0442(1999)012<2397:TCOTC>2.0.CO;2.

Jung, Y., M. Xue, and M. Tong, 2012: Ensemble Kalman Filter Analyses of the 29–30 May 2004 Oklahoma Tornadic Thunderstorm Using One- and Two-Moment Bulk Microphysics Schemes, with Verification against Polarimetric Radar Data. *Mon. Weather Rev.*, **140**, 1457–1475, doi:10.1175/MWR-D-11-00032.1.

Khain, A., A. Pokrovsky, M. Pinsky, A. Seifert, and V. Phillips, 2004: Simulation of Effects of Atmospheric Aerosols on Deep Turbulent Convective Clouds Using a Spectral Microphysics

Mixed-Phase Cumulus Cloud Model. Part I: Model Description and Possible Applications. *J. Atmos. Sci.*, **61**, 2963–2982, doi:10.1175/JAS-3350.1.

Khain, A., D. Rosenfeld, and A. Pokrovsky, 2005: Aerosol impact on the dynamics and microphysics of deep convective clouds. *Q. J. R. Meteorol. Soc.*, **131**, 2639–2663, doi:10.1256/qj.04.62.

Khain, A. P., N. BenMoshe, and A. Pokrovsky, 2008: Factors Determining the Impact of Aerosols on Surface Precipitation from Clouds: An Attempt at Classification. *J. Atmos. Sci.*, **65**, 1721–1748, doi:10.1175/2007JAS2515.1.

Khain, A. P., and I. Sednev, 1996: Simulation of precipitation formation in the Eastern Mediterranean coastal zone using a spectral microphysics cloud ensemble model. *Atmos. Res.*, **43**, 77–110, doi:10.1016/S0169-8095(96)00005-1.

Khain, A. P. and Coauthors, 2015: Representation of microphysical processes in cloud-resolving models: Spectral (bin) microphysics versus bulk parameterization. *Rev. Geophys.*, **53**, 247–322, doi:10.1002/2014RG000468.

King, N. J., K. N. Bower, J. Crosier, and I. Crawford, 2013: Evaluating MODIS cloud retrievals with in situ observations from VOCALS-REx. *Atmos. Chem. Phys.*, **13**, 191–209, doi:10.5194/acp-13-191-2013.

Kogan, Y. L., and W. J. Martin, 1994: Parameterization of Bulk Condensation in Numerical Cloud Models. *J. Atmos. Sci.*, **51**, 1728–1739, doi:10.1175/1520-0469(1994)051<1728:POBCIN>2.0.CO;2.

Koren, I., G. Dagan, and O. Altaratz, 2014: From aerosol-limited to invigoration of warm convective clouds. *Science*, **344**, 1143–1146, doi:10.1126/science.1252595.

Kumjian, M. R., S. M. Ganson, and A. V. Ryzhkov, 2012: Freezing of Raindrops in Deep Convective Updrafts: A Microphysical and Polarimetric Model. *J. Atmos. Sci.*, **69**, 3471–3490, doi:10.1175/JAS-D-12-067.1.

Lebo, Z. J., and J. H. Seinfeld, 2011: Theoretical basis for convective invigoration due to increased aerosol concentration. *Atmos. Chem. Phys.*, **11**, 5407–5429, doi:10.5194/acp-11-5407-2011.

Lebo, Z. J., H. Morrison, and J. H. Seinfeld, 2012: Are simulated aerosol-induced effects on deep convective clouds strongly dependent on saturation adjustment? *Atmos. Chem. Phys.*, **12**, 9941–9964, doi:10.5194/acp-12-9941-2012.

Lee, S. S., L. J. Donner, V. T. J. Phillips, and Y. Ming, 2008: Examination of aerosol effects on precipitation in deep convective clouds during the 1997 ARM summer experiment. *Q. J. R. Meteorol. Soc.*, **134**, 1201–1220, doi:10.1002/qj.287.

Lee, S. S., and L. J. Donner, 2011: Effects of Cloud Parameterization on Radiation and Precipitation: A Comparison Between Single-Moment Microphysics and Double-Moment Microphysics. *Terr. Atmos. Ocean. Sci.*, **22**, 403, doi:10.3319/TAO.2011.03.03.01(A).

Li, Z., F. Niu, J. Fan, Y. Liu, D. Rosenfeld, and Y. Ding, 2011: Long-term impacts of aerosols on the vertical development of clouds and precipitation. *Nat. Geosci.*, **4**, 888–894, doi:10.1038/ngeo1313.

Liao, L., R. Meneghini, and A. Tokay, 2014: Uncertainties of GPM DPR Rain Estimates Caused by DSD Parameterizations. *J. Appl. Meteorol. Climatol.*, **53**, 2524–2537, doi:10.1175/JAMC-D-14-0003.1.

Lin, Y.-L., R. D. Farley, and H. D. Orville, 1983: Bulk Parameterization of the Snow Field in a Cloud Model. *J. Clim. Appl. Meteorol.*, **22**, 1065–1092, doi:10.1175/1520-0450(1983)022<1065:BPOTSF>2.0.CO;2.

Liu, Y., and P. H. Daum, 2002: Anthropogenic aerosols: Indirect warming effect from dispersion forcing. *Nature*, **419**, 580–581, doi:10.1038/419580a.

Liu, Y., and P. H. Daum, 2004: Parameterization of the Autoconversion Process.Part I: Analytical Formulation of the Kessler-Type Parameterizations. *J. Atmos. Sci.*, **61**, 1539–1548, doi:10.1175/1520-0469(2004)061<1539:POTAPI>2.0.CO;2.

Liu, Y., P. H. Daum, and S. S. Yum, 2006: Analytical expression for the relative dispersion of the cloud droplet size distribution. *Geophys. Res. Lett.*, **33**, L02810, doi:10.1029/2005GL024052.

Liu, Y., P. H. Daum, H. Guo, and Y. Peng, 2008: Dispersion bias, dispersion effect, and the aerosol–cloud conundrum. *Environ. Res. Lett.*, **3**, 045021, doi:10.1088/1748-9326/3/4/045021.

Liu, Y., Y. Laiguang, Y. Weinong, and L. Feng, 1995: On the size distribution of cloud droplets. *Atmos. Res.*, **35**, 201–216, doi:10.1016/0169-8095(94)00019-A.

Loftus, A. M., and W. R. Cotton, 2014: Examination of CCN Impacts on Hail in a Simulated Supercell Storm with Triple-Moment Hail Bulk Microphysics. *Atmos. Res.*, doi:10.1016/j.atmosres.2014.04.017.

Lu, M.-L., and J. H. Seinfeld, 2006: Effect of aerosol number concentration on cloud droplet dispersion: A large-eddy simulation study and implications for aerosol indirect forcing. *J. Geophys. Res.*, **111**, D02207, doi:10.1029/2005JD006419.

Lu, M.-L., W. C. Conant, H. H. Jonsson, V. Varutbangkul, R. C. Flagan, and J. H. Seinfeld, 2007: The Marine Stratus/Stratocumulus Experiment (MASE): Aerosol-cloud relationships in marine stratocumulus. *J. Geophys. Res.*, **112**, D10209, doi:10.1029/2006JD007985.

Lu, M.-L., G. Feingold, H. H. Jonsson, P. Y. Chuang, H. Gates, R. C. Flagan, and J. H. Seinfeld, 2008: Aerosol-cloud relationships in continental shallow cumulus. *J. Geophys. Res.*, **113**, D15201, doi:10.1029/2007JD009354.

Luo, Y., K.-M. Xu, H. Morrison, and G. McFarquhar, 2008: Arctic Mixed-Phase Clouds Simulated by a Cloud-Resolving Model: Comparison with ARM Observations and Sensitivity to Microphysics Parameterizations. *J. Atmos. Sci.*, **65**, 1285–1303, doi:10.1175/2007JAS2467.1.

Mace, G. G., Q. Zhang, M. Vaughan, R. Marchand, G. Stephens, C. Trepte, and D. Winker, 2009: A description of hydrometeor layer occurrence statistics derived from the first year of merged Cloudsat and CALIPSO data. *J. Geophys. Res.*, **114**, D00A26, doi:10.1029/2007JD009755.

Mansell, E. R., 2010: On sedimentation and advection in multimoment bulk microphysics. *J. Atmos. Sci.*, **67**, 3084-3094, doi:10.1175/2010JAS3341.1.

Mansell, E. R., C. L. Ziegler, and E. C. Bruning, 2010: Simulated Electrification of a Small Thunderstorm with Two-Moment Bulk Microphysics. *J. Atmos. Sci.*, **67**, 171–194, doi:10.1175/2009JAS2965.1.

Manton, M., and W. Cotton, 1977: Formulation of approximate equations for modeling moist deep convection on the mesoscale. Colorado State University.

Marshall, J. S., and W. M. K. Palmer, 1948: Tge Distribution of Raindrops with Size. *J. Meteorol.*, **5**, 165–166, doi:10.1175/1520-0469(1948)005<0165:TDORWS>2.0.CO;2.

Martins, J. A., M. A. F. Silva Dias, and F. L. T. Gonçalves, 2009: Impact of biomass burning aerosols on precipitation in the Amazon: A modeling case study. *J. Geophys. Res.*, **114**, D02207, doi:10.1029/2007JD009587.

McDonald, J. E., 1963: The saturation adjustment in numerical modelling of fog. *J. Atmos. Sci.*, **20**, 476–478.

McFarquhar, G. M., T.-L. Hsieh, M. Freer, J. Mascio, and B. F. Jewett, 2015: The Characterization of Ice Hydrometeor Gamma Size Distributions as Volumes in $N_0 - \lambda - \mu$ Phase Space: Implications for Microphysical Process Modeling. *J. Atmos. Sci.*, **72**, 892–909, doi:10.1175/JAS-D-14-0011.1.

Medeiros, B., L. Nuijens, C. Antoniazzi, and B. Stevens, 2010: Low-latitude boundary layer clouds as seen by CALIPSO. *J. Geophys. Res.*, **115**, D23207, doi:10.1029/2010JD014437.

Meyers, M. P., R. L. Walko, J. Y. Harrington, and W. R. Cotton, 1997: New RAMS cloud microphysics parameterization. Part II: The two-moment scheme. *Atmos. Res.*, **45**, 3–39, doi:10.1016/S0169-8095(97)00018-5.

Milbrandt, J. A., and R. McTaggart-Cowan, 2010: Sedimentation-induced errors in bulk microphysics schemes. *J. Atmos. Sci*., **67**, 3931-3948, doi:10.1175/2010JAS3541.1.

Milbrandt, J. A., and M. K. Yau, 2005a: A Multimoment Bulk Microphysics Parameterization. Part I: Analysis of the Role of the Spectral Shape Parameter. *J. Atmos. Sci.*, **62**, 3051–3064, doi:10.1175/JAS3534.1.

Milbrandt, J. A., and M. K. Yau, 2005b: A Multimoment Bulk Microphysics Parameterization. Part II: A Proposed Three-Moment Closure and Scheme Description. *J. Atmos. Sci.*, **62**, 3065–3081, doi:10.1175/JAS3535.1.

Milbrandt, J. A., M. K. Yau, J. Mailhot, S. Bélair, and R. McTaggart-Cowan, 2010: Simulation of an Orographic Precipitation Event during IMPROVE-2. Part II: Sensitivity to the Number of Moments in the Bulk Microphysics Scheme. *Mon. Weather Rev.*, **138**, 625–642, doi:10.1175/2009MWR3121.1.

Miles, N. L., J. Verlinde, and E. E. Clothiaux, 2000: Cloud Droplet Size Distributions in Low-Level Stratiform Clouds. *J. Atmos. Sci.*, **57**, 295–311, doi:10.1175/1520-0469(2000)057<0295:CDSDIL>2.0.CO;2.

Molthan, A. L., and B. A. Colle, 2012: Comparisons of Single- and Double-Moment Microphysics Schemes in the Simulation of a Synoptic-Scale Snowfall Event. *Mon. Weather Rev.*, **140**, 2982–3002, doi:10.1175/MWR-D-11-00292.1.

Morrison, H., J. A. Curry, and V. I. Khvorostyanov, 2005: A New Double-Moment Microphysics Parameterization for Application in Cloud and Climate Models. Part I: Description. *J. Atmos. Sci.*, **62**, 1665–1677, doi:10.1175/JAS3446.1.

Morrison, H., and W. W. Grabowski, 2007: Comparison of Bulk and Bin Warm-Rain Microphysics Models Using a Kinematic Framework. *J. Atmos. Sci.*, **64**, 2839–2861, doi:10.1175/JAS3980.

Morrison, H., G. Thompson, and V. Tatarskii, 2009: Impact of Cloud Microphysics on the Development of Trailing Stratiform Precipitation in a Simulated Squall Line: Comparison of One- and Two-Moment Schemes. *Mon. Weather Rev.*, **137**, 991–1007, doi:10.1175/2008MWR2556.1.

Morrison, H., and J. Milbrandt, 2011: Comparison of Two-Moment Bulk Microphysics Schemes in Idealized Supercell Thunderstorm Simulations. *Mon. Weather Rev.*, **139**, 1103–1130, doi:10.1175/2010MWR3433.1.

Morrison, H., S. A. Tessendorf, K. Ikeda, and G. Thompson, 2012: Sensitivity of a Simulated Midlatitude Squall Line to Parameterization of Raindrop Breakup. *Mon. Weather Rev.*, **140**, 2437–2460, doi:10.1175/MWR-D-11-00283.1.

Neelin, J. D., O. Peters, and K. Hales, 2009: The Transition to Strong Convection. *J. Atmos. Sci.*, **66**, 2367–2384, doi:10.1175/2009JAS2962.1.

Onishi, R., and K. Takahashi, 2012: A Warm-Bin–Cold-Bulk Hybrid Cloud Microphysical Model. *J. Atmos. Sci.*, **69**, 1474–1497, doi:10.1175/JAS-D-11-0166.1.

Ovtchinnikov, M., and Y. L. Kogan, 2000: An Investigation of Ice Production Mechanisms in Small Cumuliform Clouds Using a 3D Model with Explicit Microphysics. Part I: Model Description. *J. Atmos. Sci.*, **57**, 2989–3003, doi:10.1175/1520-0469(2000)057<2989:AIOIPM>2.0.CO;2.

Painemal, D., and P. Zuidema, 2011: Assessment of MODIS cloud effective radius and optical thickness retrievals over the Southeast Pacific with VOCALS-REx in situ measurements. *J. Geophys. Res. Atmos.*, **116**, n/a – n/a, doi:10.1029/2011JD016155.

Paluch, I. R., and D. G. Baumgardner, 1989: Entrainment and Fine-Scale Mixing in a Continental Convective Cloud. *J. Atmos. Sci.*, **46**, 261–278, doi:10.1175/1520-0469(1989)046<0261:EAFSMI>2.0.CO;2.

Pandithurai, G., S. Dipu, T. V. Prabha, R. S. Maheskumar, J. R. Kulkarni, and B. N. Goswami, 2012: Aerosol effect on droplet spectral dispersion in warm continental cumuli. *J. Geophys. Res.*, **117**, D16202, doi:10.1029/2011JD016532.

Pawlowska, H., W. W. Grabowski, and J.-L. Brenguier, 2006: Observations of the width of cloud droplet spectra in stratocumulus. *Geophys. Res. Lett.*, **33**, L19810, doi:10.1029/2006GL026841.

Peng, Y., and U. Lohmann, 2003: Sensitivity study of the spectral dispersion of the cloud droplet size distribution on the indirect aerosol effect. *Geophys. Res. Lett.*, **30**, n/a – n/a, doi:10.1029/2003GL017192.

Peng, Y., U. Lohmann, R. Leaitch, and M. Kulmala, 2007: An investigation into the aerosol dispersion effect through the activation process in marine stratus clouds. *J. Geophys. Res.*, **112**, D11117, doi:10.1029/2006JD007401.

Pinsky, M., I. P. Mazin, A. Korolev, and A. Khain, 2013: Supersaturation and Diffusional Droplet Growth in Liquid Clouds. *J. Atmos. Sci.*, **70**, 2778–2793, doi:10.1175/JAS-D-12-077.1.

Pinsky, M., I. P. Mazin, A. Korolev, and A. Khain, 2014: Supersaturation and diffusional droplet growth in liquid clouds: Polydisperse spectra. *J. Geophys. Res. Atmos.*, **119**, 12,872–12,887, doi:10.1002/2014JD021885.

Platnick, S., and F. P. J. Valero, 1995: A Validation of a Satellite Cloud Retrieval during ASTEX. *J. Atmos. Sci.*, **52**, 2985–3001, doi:10.1175/1520-0469(1995)052<2985:AVOASC>2.0.CO;2.

Politovich, M. K., 1993: A study of the broadening of droplet size distributions in cumuli. *J. Atmos. Sci*, **50**, 2230–2244.

Posselt, D. J., S. C. van den Heever, and G. L. Stephens, 2008: Trimodal cloudiness and tropical stable layers in simulations of radiative convective equilibrium. *Geophys. Res. Lett.*, **35**, L08802, doi:10.1029/2007GL033029.

Pruppacher, H. R., and J. D. Klett, 2010: Microphysics of Clouds and Precipitation. Vol. 18 of *Atmospheric and Oceanographic Sciences Library*, Springer Netherlands, Dordrecht, 10–30.

Rasmussen, R. M., I. Geresdi, G. Thompson, K. Manning, and E. Karplus, 2002: Freezing Drizzle Formation in Stably Stratified Layer Clouds: The Role of Radiative Cooling of Cloud Droplets, Cloud Condensation Nuclei, and Ice Initiation. *J. Atmos. Sci.*, **59**, 837–860, doi:10.1175/1520-0469(2002)059<0837:FDFISS>2.0.CO;2.

Roh, W. and M. Satoh, 2014: Evaluation of Precipitating Hydrometeor Parameterizations in a Single-Moment Bulk Microphysics Scheme for Deep Convective Systems over the Tropical Central Pacific. *J. Atmos. Sci.*, **71**, 2654-2673, doi: 10.1175/JAS-D-13-0252.1.

Rosenfeld, D., U. Lohmann, G. B. Raga, C. D. O'Dowd, M. Kulmala, S. Fuzzi, A. Reissell, and M. O. Andreae, 2008: Flood or drought: how do aerosols affect precipitation? *Science*, **321**, 1309–1313, doi:10.1126/science.1160606.

Rotstayn, L. D., and Y. Liu, 2003: Sensitivity of the First Indirect Aerosol Effect to an Increase of Cloud Droplet Spectral Dispersion with Droplet Number Concentration. *J. Clim.*, **16**, 3476–3481, doi:10.1175/1520-0442(2003)016<3476:SOTFIA>2.0.CO;2.

Rutledge, S. A., and P. Hobbs, 1983: The Mesoscale and Microscale Structure and Organization of Clouds and Precipitation in Midlatitude Cyclones. VIII: A Model for the "Seeder-Feeder" Process in Warm-Frontal Rainbands. *J. Atmos. Sci.*, **40**, 1185–1206, doi:10.1175/1520-0469(1983)040<1185:TMAMSA>2.0.CO;2.

Saleeby, S., and W. Cotton, 2004: A large-droplet mode and prognostic number concentration of cloud droplets in the Colorado State University Regional Atmospheric Modeling System (RAMS). Part I: Module descriptions and supercell test simulations. *J. Appl. Meteorol.*, **44**, 182–195.

Saleeby, S. M., and W. R. Cotton, 2008: A Binned Approach to Cloud-Droplet Riming Implemented in a Bulk Microphysics Model. *J. Appl. Meteorol. Climatol.*, **47**, 694–703, doi:10.1175/2007JAMC1664.1.

Saleeby, S. M., and S. C. van den Heever, 2013: Developments in the CSU-RAMS Aerosol Model: Emissions, Nucleation, Regeneration, Deposition, and Radiation. *J. Appl. Meteorol. Climatol.*, **52**, 2601–2622, doi:10.1175/JAMC-D-12-0312.1.

Saleeby, S. M., S. R. Herbener, S. C. van den Heever, and T. L'Ecuyer, 2015: Impacts of Cloud Droplet–Nucleating Aerosols on Shallow Tropical Convection. *J. Atmos. Sci.*, **72**, 1369–1385, doi:10.1175/JAS-D-14-0153.1.

Seifert, A., and K. D. Beheng, 2001: A double-moment parameterization for simulating autoconversion, accretion and selfcollection. *Atmos. Res.*, **59-60**, 265–281, doi:10.1016/S0169-8095(01)00126-0.

Seifert, A., and K. D. Beheng, 2006: A two-moment cloud microphysics parameterization for mixed-phase clouds. Part 1: Model description. *Meteorol. Atmos. Phys.*, **92**, 45–66, doi:10.1007/s00703-005-0112-4.

Seiki, T., and T. Nakajima, 2014: Aerosol Effects of the Condensation Process on a Convective Cloud Simulation. *J. Atmos. Sci.*, **71**, 833–853, doi:10.1175/JAS-D-12-0195.1.

Sheffield, A. M., S. M. Saleeby, and S. C. van den Heever, 2015: Aerosol-induced mechanisms for cumulus congestus growth. *J. Geophys. Res. Atmos.*, **120**, 8941–8952, doi:10.1002/2015JD023743.

Sheridan, P. J., D. J. Delene, and J. A. Ogren, 2001: Four years of continuous surface aerosol measurements from the Department of Energy ' s Atmospheric Radiation Measurement Program Southern Great Plains Cloud and Radiation Testbed site. *J. Geophys. Res.*, **106**, 20735–20747, doi:10.1029/2001JD000785.

Shima, S., K. Kusano, A. Kawano, T. Sugiyama, and S. Kawahara, 2009: The super-droplet method for the numerical simulation of clouds and precipitation: a particle-based and probabilistic microphysics model coupled with a non-hydrostatic model. *Q. J. R. Meteorol. Soc.*, **135**, 1307–1320, doi:10.1002/qj.441.

Shipway, B. J., and A. A. Hill, 2012: Diagnosis of systematic differences between multiple parametrizations of warm rain microphysics using a kinematic framework. *Q. J. R. Meteorol. Soc.*, **138**, 2196–2211, doi:10.1002/qj.1913.

Simpson, J., R. H. Simpson, D. A. Andrews, and M. A. Eaton, 1965: Experimental Cumulus Dynamics. *Rev. Geophys.*, **3**, 387–431.

Smagorinsky, J., 1963: General Circulation Experiments with the Primitive Equations. *Mon. Weather Rev.*, **91**, 99–164, doi:10.1175/1520-0493(1963)091<0099:GCEWTP>2.3.CO;2.

Soong, S.-T., and Y. Ogura, 1973: A Comparison Between Axisymmetric and Slab-Symmetric Cumulus Cloud Models. *J. Atmos. Sci.*, **30**, 879–893, doi:10.1175/1520-0469(1973)030<0879:ACBAAS>2.0.CO;2.

Squires, P., 1958: The Microstructure and Colloidal Stability of Warm Clouds: Part II - The Causes of the Variations in Microstructure. *Tellus*, **10**, 262–271, doi:9229.

Stolz, D. C., S. A. Rutledge, and J. R. Pierce, 2015: Simultaneous influences of thermodynamics and aerosols on deep convection and lightning in the tropics. *J. Geophys. Res. Atmos.*, **120**, 6207–6231, doi:10.1002/2014JD023033.Received.

Storer, R. L., and S. C. van den Heever, 2013: Microphysical Processes Evident in Aerosol Forcing of Tropical Deep Convective Clouds. *J. Atmos. Sci.*, **70**, 430–446, doi:10.1175/JAS-D-12-076.1.

Storer, R. L., S. C. van den Heever, and T. S. L'Ecuyer, 2014: Observations of aerosol-induced convective invigoration in the tropical east Atlantic. *J. Geophys. Res. Atmos.*, **119**, 3963–3975, doi:10.1002/2013JD020272.

Straka, J., and E. Mansell, 2005: A bulk microphysics parameterization with multiple ice precipitation categories. *J. Appl. Meteorol.*, 445–466.

Swann, H., 1998: Sensitivity to the representation of precipitating ice in CRM simulations of deep convection. *Atmos. Res.*, **47-48**, 415–435, doi:10.1016/S0169-8095(98)00050-7.

Tao, W.-K., J.-P. Chen, Z. Li, C. Wang, and C. Zhang, 2012: Impact of aerosols on convective clouds and precipitation. *Rev. Geophys.*, **50**, RG2001, doi:10.1029/2011RG000369.

Thompson, D. W. J., D. J. Seidel, W. J. Randel, C.-Z.Zou, A. H. Butler, C. Mears, A. Osso, C. Long, R. Lin, 2012: The mystery of recent stratospheric temperature trends. *Nature*, **491**, 692-697. doi:10.1038/nature11579.

Thompson, E. J., S. A. Rutledge, B. Dolan, and M. Thurai, 2015: Drop size distributions and radar observations of convective and stratiform rain over the equatorial Indian and West Pacific Oceans. *J. Atmos. Sci.*, 150904104933002, doi:10.1175/JAS-D-14-0206.1.

Thompson, G., R. M. Rasmussen, and K. Manning, 2004: Explicit Forecasts of Winter Precipitation Using an Improved Bulk MicrophysicsScheme. Part I: Description and Sensitivity Analysis. *Am. Meteorol. Soc.*, **132**, 519–542.

Thompson, G., P. R. Field, W. D. Hall, and R. M. Rasmussen, 2008: Explicit Forecasts of Winter Precipitation Using an Improved Bulk Microphysics Scheme. Part II: Implementation of a New Snow Parameterization. *Mon. Weather Rev.*, **136**, 5095–5115, doi:10.1175/2008MWR2387.1.

Tompkins, A. M., 2001: Organization of Tropical Convection in Low Vertical Wind Shears: The Role of Cold Pools. *J. Atmos. Sci.*, **58**, 1650–1672, doi:10.1175/1520-0469(2001)058<1650:OOTCIL>2.0.CO;2.

Twomey, S., 1959: The Nuclei of Natural Cloud Formation Part II : The Supersaturation in Natural Clouds and the Variation of Cloud Droplet Concentration. *Geofis. pura e Appl.*, **43**, 243–249.

Twomey, S., 1974: Pollution and the Planetary Albedo. *Atmos. Environ.*, doi:10.1016/j.atmosenv.2007.10.062.

Twomey, S., 1977: The Influence of Pollution on the Shortwave Albedo of Clouds. *J. Atmos. Sci.*, **34**, 1149–1152, doi:10.1175/1520-0469(1977)034<1149:TIOPOT>2.0.CO;2.

Ulbrich, C. W., 1983: Natural Variations in the Analytical Form of the Raindrop Size Distribution. *J. Clim. Appl. Meteorol.*, **22**, 1764–1775, doi:10.1175/1520-0450(1983)022<1764:NVITAF>2.0.CO;2.

Ulbrich, C. W., and D. Atlas, 1998: Rainfall Microphysics and Radar Properties: Analysis Methods for Drop Size Spectra. *J. Appl. Meteorol.*, **37**, 912–923, doi:10.1175/1520-0450(1998)037<0912:RMARPA>2.0.CO;2.

van den Heever, S. C., and W. R. Cotton, 2004: The Impact of Hail Size on Simulated Supercell Storms. *J. Atmos. Sci.*, **61**, 1596–1609, doi:10.1175/1520-0469(2004)061<1596:TIOHSO>2.0.CO;2.

van den Heever, S. C., G. G. Carrió, W. R. Cotton, P. J. DeMott, and A. J. Prenni, 2006: Impacts of Nucleating Aerosol on Florida Storms. Part I: Mesoscale Simulations. *J. Atmos. Sci.*, **63**, 1752–1775, doi:10.1175/JAS3713.1.

van den Heever, S. C., G. L. Stephens, and N. B. Wood, 2011: Aerosol Indirect Effects on Tropical Convection Characteristics under Conditions of Radiative–Convective Equilibrium. *J. Atmos. Sci.*, **68**, 699–718, doi:10.1175/2010JAS3603.1.

Van Weverberg, K., A. M. Vogelmann, H. Morrison, and J. a. Milbrandt, 2012: Sensitivity of Idealized Squall-Line Simulations to the Level of Complexity Used in Two-Moment Bulk Microphysics Schemes. *Mon. Weather Rev.*, **140**, 1883–1907, doi:10.1175/MWR-D-11-00120.1.

Van Weverberg, K. and Coauthors, 2013: The Role of Cloud Microphysics Parameterization in the Simulation of Mesoscale Convective System Clouds and Precipitation in the Tropical Western Pacific. *J. Atmos. Sci.*, **70**, 1104–1128, doi:10.1175/JAS-D-12-0104.1.

Van Weverberg, K., E. Goudenhoofdt, U. Blahak, E. Brisson, M. Demuzere, P. Marbaix, and J.-P. van Ypersele, 2014: Comparison of one-moment and two-moment bulk microphysics for high-resolution climate simulations of intense precipitation. *Atmos. Res.*, **147-148**, 145–161, doi:10.1016/j.atmosres.2014.05.012.

Wacker, U. and C. Lüpkes, 2009: On the selection of prognostic moments in parameterization schemes for drop sedimentation. *Tellus*, **61A**, 498-511, doi:10.1111/j.1600-0870.2009.00405.x.

Wacker, U. and A. Seifert, 2001: Evolution of rain water profiles resulting from pure sedimentation: Spectral vs. parameterizaed description. *Atmos. Res.*, **58**, 19-39.

Walko, R. L. and Coauthors, 2000a: Coupled atmosphere, biophysics and hydrology models for environmental modeling. *J. Appl. Meteorol.*, **39**, 931–944, doi:10.1175/1520-0450(2000)039<0931:CABHMF>2.0.CO;2.

Walko, R. L., W. R. Cotton, G. Feingold, and B. Stevens, 2000b: Efficient computation of vapor and heat diffusion between hydrometeors in a numerical model. *Atmos. Res.*, **53**, 171–183, doi:10.1016/S0169-8095(99)00044-7.

Walko, R. L., W. R. Cotton, M. P. Meyers, and J. Y. Harrington, 1995: New RAMS cloud microphysics parameterization part I: the single-moment scheme. *Atmos. Res.*, **38**, 29–62, doi:10.1016/0169-8095(94)00087-T.

Wang, X., H. Xue, W. Fang, and G. Zheng, 2011: A study of shallow cumulus cloud droplet dispersion by large eddy simulations. *Acta Meteorol. Sin.*, **25**, 166–175, doi:10.1007/s13351-011-0024-9.

Weisman, M., and J. Klemp, 1982: The dependence of numerically simulated convective storms on vertical wind shear and buoyancy. *Mon. Weather Rev.*, **110**, 504–520.

Wu, L., and G. W. Petty, 2010: Intercomparison of Bulk Microphysics Schemes in Model Simulations of Polar Lows. *Mon. Weather Rev.*, **138**, 2211–2228, doi:10.1175/2010MWR3122.1.

Yum, S. S., and J. G. Hudson, 2005: Adiabatic predictions and observations of cloud droplet spectral broadness. *Atmos. Res.*, **73**, 203–223, doi:10.1016/j.atmosres.2004.10.006.

Yussouf, N., and D. J. Stensrud, 2012: Comparison of Single-Parameter and Multiparameter Ensembles for Assimilation of Radar Observations Using the Ensemble Kalman Filter. *Mon. Weather Rev.*, **140**, 562–586, doi:10.1175/MWR-D-10-05074.1.

Zelinka, M. D., and D. L. Hartmann, 2010: Why is longwave cloud feedback positive? *J. Geophys. Res*., **115**, D16117, doi:10.1029/2010JD013817.

Zhao, C. and Coauthors, 2006: Aircraft measurements of cloud droplet spectral dispersion and implications for indirect aerosol radiative forcing. *Geophys. Res. Lett.*, **33**, L16809, doi:10.1029/2006GL026653.

Zhu, P., and B. Albrecht, 2003: Large eddy simulations of continental shallow cumulus convection. *J. Geophys. Res.*, **108**, 4453, doi:10.1029/2002JD003119.